The Impact of Combustor Turbulence on Loss Mechanisms in the High Pressure Turbine

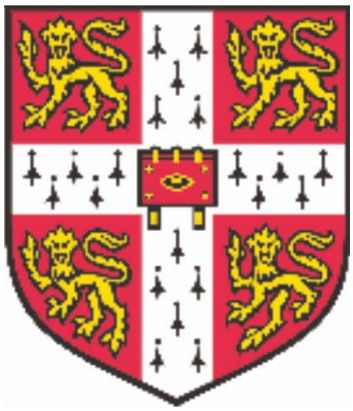

Maria B. Folk

Department of Engineering

University of Cambridge

This dissertation is submitted for the degree of

Doctor of Philosophy

Gonville and Caius College September 2019

In memory of Steven G. Gegg

Declaration

I hereby declare that except where specific reference is made to the work of others, the contents of this dissertation are original and have not been submitted in whole or in part for consideration for any other degree or qualification in this, or any other university. This dissertation is my own work and contains nothing which is the outcome of work done in collaboration with others, except as specified in the text and Acknowledgements. This dissertation contains fewer than 65,000 words including appendices, bibliography, footnotes, tables and equations and has fewer than 150 figures.

Masha Folk

September 2019

Acknowledgements

The author is grateful to a number of organisations and individuals who have supported this work. First of all, my deepest respect and gratitude for Prof Rob Miller, whose supervision of this work and ideas about loss mechanisms have been invaluable. Only through his input into the project has it been able to make impact in industry and the fundamental research of academia. Dr John Coull, who also supervised this research, gave helpful advice towards the extensive measurements undertaken in this work. In addition, Prof Ed Greitzer and Prof Nick Cumpsty, through regular discussion, have offered many insights into the fundamentals of loss mechanisms in high turbulence.

Financial support was provided by the Engineering and Physical Sciences Research Council (EPSRC), Rolls-Royce, and Zonta International. In addition to being a key sponsor, EPSRC was also responsible for forming the Centre for Doctoral Training (CDT) in Gas Turbine Aerodynamics, of which the author was a member in the first cohort. The CDT program provided world-class training and a supportive community which spans the University of Cambridge, University of Oxford, and Loughborough University.

From Rolls-Royce, William Cummings, Jon Ebacher, Simon Gallimore, Fred Goenaga, and Mark Stokes have been excellent sponsors of the project, the author is grateful to for their data, discussions and ideas.

Support within the Whittle Laboratory has been forthcoming from all. Experimental advice and discussion from Dr Ivor Day, Dr Taylor, Dr Anna Young and Dr Sam Grimshaw have been incredibly helpful. Additionally, the author acknowledges Dr Andrew Wheeler for his discussion on loss accounting in turbulence and Dr John Longley for his discussions on uncertainty analysis. The support of the technical staff led by John Saunders has been excellent, the author would also like to thank them for their manufacturing of experimental components.

Special thanks go to Lachlan Jardine and Kanika Gakhar for ideas, discussions, and support. Everything else I owe to my family for making my academic ambitions possible. Finally, I would like to express a very special thank you to my husband, Thomas, for his unending love and patience.

Abstract

A blade row which is located downstream of a combustor has an extremely high turbulence intensity at inlet, typically above 10%. The peak turbulent length scale is also high, at around 20% of the chord of the downstream blade row. In a combustor, the turbulence is mainly created by impinging jets in cross flow. This may result in the turbulence being anisotropic in nature. The aim of this thesis is to investigate the effect of combustor turbulence on the loss mechanisms which occur in a turbine blade row. The thesis has a number of important findings. The combustor turbulence is characterised and is shown to be isotropic in nature. It shows that, when no pressure gradient is present, combustor turbulence increases the loss of a turbulent boundary layer by 22%. The mechanism responsible for this change is shown to be a deep penetration of the turbulence into the boundary layer. It shows that the presence of combustor turbulence increases profile loss and endwall loss in the turbine cascade studied by 37% and 38%, respectively. The presence of combustor turbulence also introduces a freestream loss resulting in the total loss of the turbine cascade rising by 47%. When these loss mechanisms were applied to the vane of an engine-representative high pressure turbine stage, it was found to result in a 1.3% reduction in stage efficiency.

Contents

List of Figures

List of Tables

Nomenclature

Latin letters:

A	Area
B	Grid porosity
C_D	Dissipation coefficient
C_f	Skin friction coefficient
C_x	Axial chord
C_p	Non-dimensional pressure
C_{pb}	Base pressure coefficient
C_{Po}	Five hole probe calibration coefficient for stagnation pressure
$C_{p_{o1}}$	Turbine inelt stagnation pressure coefficient
C_{Ps}	Five hole probe calibration coefficient for static pressure
C_α	Five hole probe calibration coefficient for yaw angle
C_β	Five hole probe calibration coefficient for pitch angle
D_{port}	Hydraulic diameter of combustor port
E	Voltage
E_{uu}	Power spectral density in space
E_{xx}	Power spectral density in time
H_{12}	Shape factor $= \delta^*/\theta$
H_{23}	Shape factor = $= \theta/\delta_e$
L_e	Turbulence dissipation length scale
M	Mesh length
P	Static pressure
P_o	Stagnation pressure
R	Autocorrelation function
Re	Reynolds number
S	Entropy

$\dot{S}_{vol}$	Entropy generation rate, per unit volume
$\dot{S}_a$	Entropy generation rate, per unit area
SKE	Secondary kinetic energy
SF	Skewness factor
T	Temperature
T_{int}	Integral time scale
Tu	Turbulence intensity
U	Instantaneous velocity, streamwise direction
$\bar{U}$	Time average velocity, streamwise direction
V	Instantaneous velocity, wall normal direction
$\bar{V}$	Time average velocity, wall normal direction
$\mathcal{V}$	Volume
Y_p	Stagnation pressure loss coefficient
c	Contraction ratio
d	Grid bar diameter
f	Frequency
h	Enthalpy
k	Turbulent kinetic energy
$\dot{m}$	Mass flow rate
p	Fluctuating pressure
q	Dynamic head
s	Specific entropy
t	Time
u	Fluctuating velocity, streamwise direction
u_τ	Shear friction velocity
v	Fluctuating velocity, wall normal direction
w	Fluctuating velocity, spanwise direction

Greek letters:

Λ_{int}	Turbulence integral length scale
$\bar{\Phi}$	Viscous dissipation of the mean field
α	Flow yaw angle

β	Freestream turbulence parameter
δ	Boundary layer thickness
δ^*	Displacement thickness
δ_e	Energy thickness
ε	Dissipation of turbulent kinetic energy
κ	Wavenumber
λ	Wavelength
μ	Viscosity
ν	Kinematic viscosity
σ	Blade pitch
θ	Momentum thickness
ρ	Density
τ_{ij}	Shear stress
ω	Frequency

Superscripts

MA	Mass averaged
MIX	Mixed out

Subscripts

∞	Freestream
p	Primary
i, j, k	Cartesian components
sec	Secondary (as in velocity components)
te	Trailing edge

Chapter 1
Introduction

All gas turbines have a high pressure turbine stage which is located downstream of its combustor. The aerodynamics of the combustor create high levels of turbulence at the inlet to the high pressure turbine, affecting its performance. Today loss in the turbine is typically measured in rigs with much lower inlet turbulence. The aim of this thesis is to investigate how combustor turbulence affects loss mechanisms in the downstream turbine stage.

The impact of combustor turbulence on a turbine cascade is shown in Figure 1.1, taken from the current study. The plot shows stagnation pressure loss measured with a pneumatic probe downstream of the blade. It can be clearly seen that the presence of combustor turbulence has a major effect on both the width of the midspan wake and on the structure of the endwall secondary flow. The integrated loss with combustor turbulence is 47% higher than that with grid turbulence. The aim of this thesis is to explain the physical cause of this rise in loss.

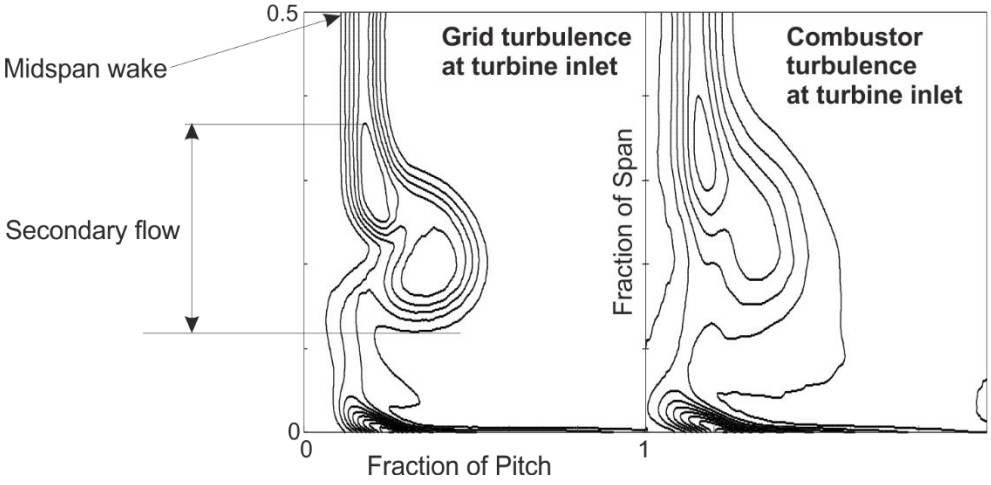

Figure 1.1: Contours of measured loss coefficient downstream of a turbine cascade (with inlet grid turbulence on the left and inlet combustor turbulence on the right).

1.1 What is combustor turbulence?

A typical rich burn combustor is shown in Figure 1.2. The aerodynamics of the combustor, which include large-scale flow recirculation and jets-in-crossflow cooling, create high levels of turbulence. This turbulent mixing is necessary to maintain the required fuel to air ratio to sustain combustion and to control emissions. Approximately one third of the air leaving the core compressor enters the combustor through the fuel nozzle and through slots surrounding the fuel nozzle in the streamwise direction. The rest of the air, two-thirds of compressor discharge, is directed around the combustor liner and enters the combustor via cooling ports on the inner and outer annulus, perpendicular to the streamwise flow. These cooling jets collide in the middle of the combustor and interact with the fuel nozzle air to create a zone of turbulent mixing.

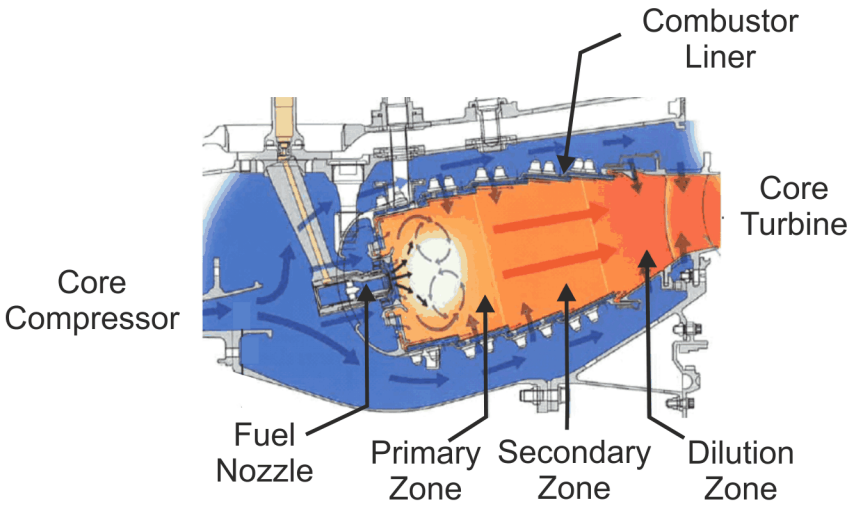

Figure 1.2: Schematic of a typical rich burn combustor (adapted from Rolls-Royce, 2005).

The turbulence that is created by these jets in crossflow is essential for the combustion process but it also convects downstream to the high pressure turbine. It will be shown in Chapter 2 that turbulence intensities at the core turbine inlet typically exceed 10% . This is very different from the typical grid turbulence of around 1% to 4% used in most turbine cascade and stage testing. This difference raises the question of how the presence of combustor turbulence changes the loss mechanisms in the downstream turbine.

1.2 Thesis structure

The aim of this thesis is to investigate the effect of combustor turbulence on the performance of a high pressure turbine stage. The research was largely experimental and was performed in

a low speed wind tunnel at the Whittle Laboratory. A combustor simulator was designed to replicate the aerodynamics of jets in cross flow and to generate 10%-18% turbulence intensity at the inlet of the test section. This is compared with traditional grid turbulence which is 1%-4% in intensity at the inlet of the test section.

Chapter 2 provides a literature survey of the effect of high freestream turbulence on loss. Chapter 3 presents the experimental methods used in this thesis. Chapter 4 describes the method of turbulence generation. Chapter 5 develops a framework for loss accounting in high levels of freestream turbulence. Chapter 6 develops the integral boundary layer equations for high levels of freestream turbulence. It shows that the integral equations for momentum and energy contain extra terms. Chapter 7 investigates the effect of combustor turbulence on a flat plate. Chapter 8 investigates the effect of combustor turbulence on the loss of a turbine cascade. Chapter 9 applies the findings of this thesis to a turbine stage and shows that the effect of combustor turbulence is a 1.3% reduction in stage efficiency.

Chapter 2
Literature Review

The purpose of this thesis is to investigate the impact of combustor turbulence on loss mechanisms in the high pressure turbine. This chapter aims to establish the limit of current knowledge of combustor turbulence effects with an analysis of the available literature. The literature review is divided into two main sections:

- Sections 2.1 and 2.2 expand on what is meant by 'combustor turbulence.' Section 2.1 examines turbulence produced by real gas turbine combustors. The aim is to generalize the fundamental flow features. Section 2.2 reviews existing methods of generating turbulence in laboratory wind tunnel experiments. The aim is to identify which methods of turbulence generation could lead to the most accurate reproduction of combustor turbulence.
- Sections 2.3 and 2.4 consider the effect of turbulence on loss mechanisms in a flat plate boundary layer and a turbine, respectively. The aim is to identify the current limitations of knowledge in this area.

At the end of the chapter, three research questions will be presented which will be answered in this thesis.

2.1 Turbulence generated by combustors

Very little is known about the specifics of combustor turbulence. This is largely due to the high temperatures at the exit of the combustor, which exclude the use of hot wires. Despite this

limitation, several seminal tests have been carried out with more complex optical diagnostics to measure turbulence in real combustors.

One of the first turbulence measurements of a real combustor was performed by Zimmerman in 1979 on Allison Model 250 turboshaft engine (Zimmerman, 1979). Zimmerman used laser Doppler velocimetry (LDV) to measure turbulence at the turbine inlet, both with and without fuel addition in the combustor. Turbulence intensity was found to be 6-10% over the range of operating conditions tested. Zimmerman reported that the turbulence profile was uniform and unaffected by the addition of fuel.

Bicen, Tse, and Whitelaw (1988) made measurements of turbulence in a reacting combustor designed to replicate that of the Rolls-Royce Gem 60 turboshaft engine. They also used LDV to measure turbulence at the combustor exit plane with and without fuel addition. Turbulence intensity was found to be 20%. Like Zimmerman, the authors also found that the turbulence profile was uniform and unaffected by the addition of fuel. Similar results were obtained as part of NASA's hot-section technology (HOST) program in the 1980's. Marek (1984) reported that measured combustor turbulence intensity on that rig was between 9% (in the centre) and 20% (at the endwalls). Furthermore, turbulence intensity was found to be unaffected by the addition of fuel.

Moss and Oldfield (1991) were the first to analyse the nature of combustor turbulence. They compared turbulence spectra in a combustor with and without combustion using unsteady pressure measurements. They found that except at very low wavenumbers, the turbulence spectrum was not affected by the combustion process. This study also found that the combustor burner geometry had no effect on the turbulence spectrum. These measurements suggest that the turbulence inside a rich burn combustor is dominated by the dilution jets. The authors also measured the anisotropy of non-reacting combustor turbulence with crossed hot wires in isothermal flow and reported that combustor turbulence was approximately isotropic.

The key finding of the aforementioned work in real combustors is that combustor turbulence is not affected by the combustion process itself. This established the current common practice in industry to measure the turbulence of a particular hardware design in an isothermal flow test. Measurements of fully featured Rolls-Royce combustors are routinely performed at Loughborough University in an isothermal facility with hot wires (e.g. Cha et al, 2012a and 2012b).

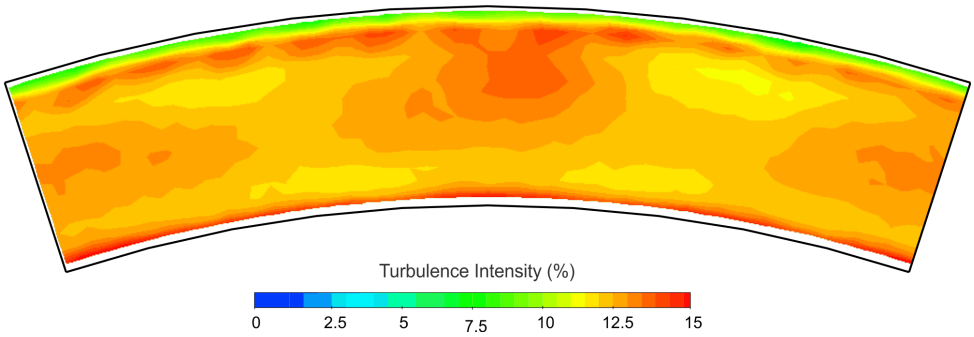

Figure 2.1 Measured turbulence intensity downstream of a rich burn combustor. Data courtesy of P. Denman, 2016.

The results from such combustor tests, which featured real fuel nozzles and liner cooling, are shown in Figure 2.1 (provided by P. Denman, 2016). Peak turbulence intensity is 15.7%. Outside of the liner wall cooling (region of high velocity and low turbulence intensity in the outer radius), the average freestream turbulence intensity is 12.5%.

Another example of isothermal combustion turbulence measurements in industry is the Pratt & Whitney Engines prototype combustor which has been extensively tested at Virginia Tech (e.g. Barringer, Richard, Walter, Stitzel, and Thole, 2002). This combustor did not include fuel nozzles but had fully a featured cooling scheme representative of a real combustor. Hot wire measurements revealed that the dilution jets generate turbulence levels of 15-18% at the exit of the combustor with a length scale that closely matches the diameter of the dilution holes.

A similar non-reacting combustor simulator was installed in the Turbine Research Facility at the Air Force Research Laboratory. In order to achieve representative combustor exit conditions, the design of this combustor simulator was made with input from engine manufacturers, namely the General Electric Company and Pratt & Whitney Engines (Barringer, Thole, and Polanka, 2004). The combustor simulator liner was annular and had two rows of opposed dilution jets, endwall film cooling, and a slight contraction to the turbine inlet. The measured turbulence intensity at the turbine inlet section was between 20% and 30%, depending on the operating condition (Barringer, Thole, and Polanka, 2007). The integral length scale was on the order of the jet diameter.

Measurements in isothermal combustors enabled new techniques which gave further detail into the flow structures. Cha et al. (2012b) used a tracer gas while testing a complete set of engine combustor hardware to gain insight into the flow responsible for the turbulence at the

combustor turbine interface. They found the mixing in the flow to be dominated by the penetration and trajectories of the dilution jets.

The combustors discussed above have all been rich-burn combustors which are dominated by jets-in-crossflow fluid dynamics. Schroll et al. (2017) recently made measurements of turbulence in a reacting, lean-burn combustor using particle image velocimetry (PIV). The measured turbulence intensity of a lean burn combustor was between 8% and 20% at the combustor exit.

In summary, combustor turbulence intensity is typically above 10%, and it is generated by the fluid dynamics of the mixing process. Notably, in a rich burn combustor, the nature of combustor turbulence is not changed by the combustion process itself.

2.2 Generating combustor turbulence in a laboratory

Turbulence in a laboratory is typically generated by means of a turbulence grid placed normal to the flow stream. Flow separation from the grid bars causes turbulent wakes which coalesce into a turbulent flow field downstream. This section will review traditional and non-traditional methods of generating high turbulence for laboratory testing.

2.2.1 Passive grids

Passive (also called static) grids of round or square bars have long been used in wind tunnels to generate turbulence. They are called so because they involve no moving parts and are a static feature of the wind tunnel. The most practical and comprehensive summary of passive grid design was published by Roach in 1987. Roach combined turbulence theories and a considerable amount of experiments to develop a practical guide relating grid geometry and the turbulence intensity, length scale and pressure drop.

An example of turbulence grid design using Roach's guidelines is presented in Figure 2.2. The turbulence grid is an array of parallel square bars of width d and of spacing $(M - d)$. The geometric parameter M is the representative mesh length. Turbulence intensity decays downstream with axial distance normalized by the bar width:

$$Tu = C_1 \left(\frac{x}{d}\right)^{-5/7} \tag{2.1}$$

The pressure drop, ΔP, across the grid scales inversely with porosity, B, of the grid:

$$\frac{\Delta P}{q} = C_2 \left(\frac{1}{\mathrm{B}^2} - 1 \right)^{C_3} \tag{2.2}$$

where C_1, C_2, and C_3 are constants which are a function of Reynolds number, Mach number and grid geometry.

Measurements in grid turbulence must be sufficiently far downstream from the grid itself where the wakes have had time to coalesce into a homogenous flow, creating uniform and nearly isotropic turbulence. The convention is $10 < x/M < 40$, where x is a measure of downstream distance (Roach, 1987, and Hearst, 2015).

A conceptual design of a turbulence grid is shown in Figure 2.2 based on the guidelines of Roach. The maximum turbulence intensity, 9%, is achieved by a grid which has high solidity of 50% and is located ten mesh lengths upstream of the test section. This particular design is on the border of the feasible design space and is likely to have poor flow uniformity. It also requires a high pressure drop across the grid. To achieve flow uniformity, the turbulence grid must have a lower solidity and be located further upstream of the test section. An example of a typical grid is indicated with a black square. This grid has a solidity of 40% and is located 30 mesh lengths upstream of the test section. The turbulence intensity of this grid is 3.4%.

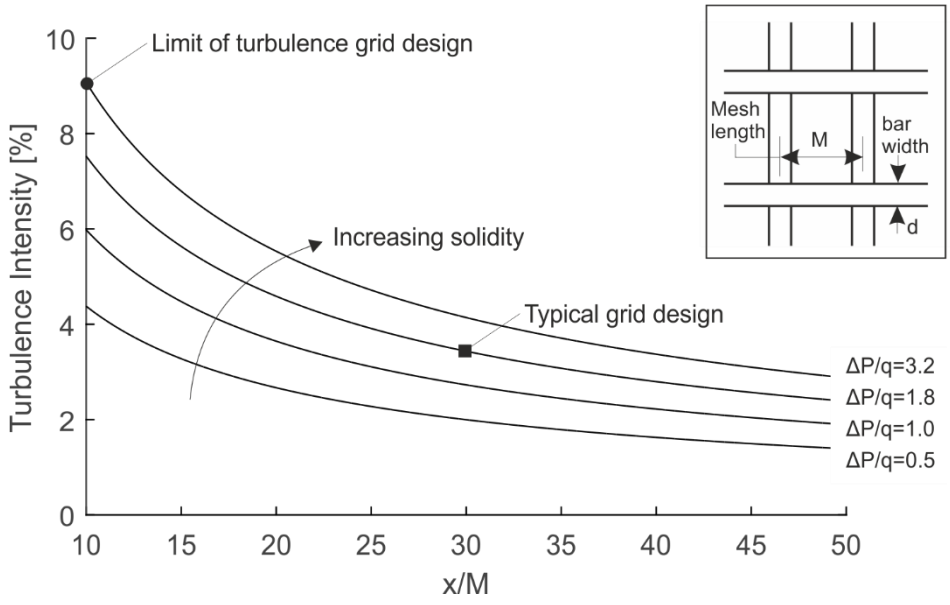

Figure 2.2: Turbulence grid intensity and pressure drop, calculated using Roach (1987).

For uniform flow, conventional grid turbulence is typically limited to <4% turbulence intensity. To achieve higher turbulence levels, grids with non-uniform geometries are often employed (Figure 2.3). This is because the flow produced by a non-uniform grid generates wakes of different sizes which interact at different locations downstream of the grid. The result is a turbulence field which contains eddies of different sizes and has higher turbulence intensity downstream of the grid. Figure 2.3.a shows a fractal grid and Figure 2.3.b shows an 'agitator wing' grid. The latter has been used by Haldeman et al. (2008) to generate turbulence intensities up to 14% in a high speed turbine rig.

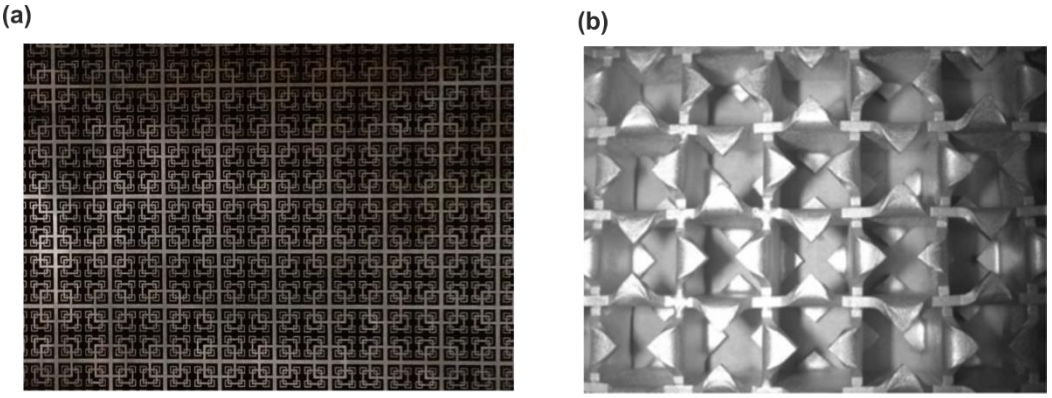

Figure 2.3: Non-conventional static turbulence grids including (a) fractal geometry (Hearst, 2015), and (b) wing geometry (Haldeman et al, 2008).

The problem with such grids is that they have poor flow uniformity. Hearst, who in 2015 conducted a detailed measurement campaign of conventional and fractal grid turbulence, found that fractal grids required much larger distance to achieve flow uniformity compared to conventional grids. Hearst concluded the perceived benefit of fractal grids have been deduced from measurements that were taken too close to the grid itself, where turbulence was not sufficiently developed. Sufficiently far downstream, non-conventional passive grids (such as Hearst's fractal grid) have low levels of turbulence intensity.

In summary, a review of existing literature shows that it is difficult to achieve high turbulence intensity with a passive grid while maintaining a uniform inflow to the test section.

2.2.2 Active grids

Two types of active grids exist which can generate higher turbulence intensities than traditional static grids. These are classified as moving grids and blowing grids.

Moving grids are similar in geometry to static grids with agitator wings but the grid bars are allowed to rotate. This design generates time and space varying solidity that is on average higher than that of passive grids and results in higher turbulence intensities. The rotational speed of the bars is typically in the range of 2-6 Hz, with adjacent bars rotating in opposite directions. The level of turbulence intensity of a moving grid is set by the bar rotational speed, the wing design, and the distance between the grid and the test section (Hearst and Lavoie, 2012). Porous wings (e.g. Figure 2.4) tend to produce higher turbulence intensity than solid wings (Dogan, 2017). Recently, Dogan et al. (2016) used an active grid to generate turbulence intensities up to 13% in a low speed wind tunnel.

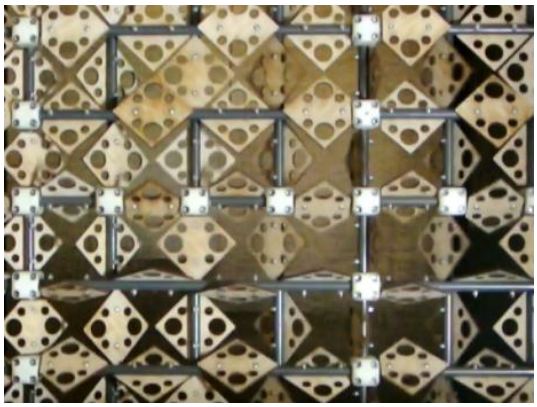

Figure 2.4: Photograph of an active grid with porous agitator wings (Dogan, 2017).

Blowing grids are similar to conventional static grids but the grid bars pass high pressure air which is injected in the upstream or downstream direction. A benefit of a blowing grid is that they typically generate a more uniform flow field relative to a passive grid (Boyle et al. (1998)). Air can be injected in the upstream (e.g. Flegel et al., 2014) or downstream (e.g. Mehendale et al., 1990) direction. Recently, Flegel et al. (2014) used a blowing grid to generate up to 15% turbulence intensity upstream of a turbine cascade.

Active grids and blown grids are more complicated since they require a separate mechanism to control either the motion or the secondary air flow.

2.2.3 Jets in crossflow

As early as the 1970's, the need to understand the thermal mixing in gas turbine combustion chambers motivated studies on the mixing characteristics of jets injected normally into a confined crossflow. The impetus of these early jets in crossflow studies was to correlate flow

and geometric variables to temperature non-uniformity. Holdeman (1991) presents a comprehensive summary on the large body of research in this field.

Measurements of a single row of circular jets in a straight duct showed that the most important flow variable was the momentum flux ratio between the mainstream and the jet. High momentum flux ratios led to increased jet penetration and enhanced mixing.

Although turbulence was not the focus of these early studies, it is clear that the enhanced mixing of jets in crossflow is caused by turbulence. Hence a jets in crossflow configuration was a natural choice for a turbulence generator capable of creating intensity levels above those of a typical grid. Thole designed such a turbulence generator in 1992 to test the effect of combustor turbulence on skin friction and heat transfer. This device used additional blowers to inject air form a different supply into the mainstream ahead of a test section. The turbulence measured in the test section had an intensity of 20%.

Recently, Cresci et al. (2015) used a similar set up for turbulence generation ahead of a linear turbine cascade in the Oxford Combustor-Turbine Interaction (CTI) rig. The geometry of the CTI rig is engine representative. This turbulence generator has two rows of circular jets. The second row of jets have a diameter approximately 1.5 times larger than the first row of jets. The measured turbulence intensity at the turbine inlet plane was between 15-20%.

Cresci noted that the turbulence integral length scale was related to size of the jets which generated it. However, because the experiment set up used varying jet diameters, it was unclear which had the most influence on the turbulence.

A different approach for turbulence generation is combustor simulators. The development of a combustor-style turbulence generator was first reported by Ames in 1990 who built and tested several configurations in his initial study. In later studies (e.g. Ames, and Plesniak, 1997, and Kingery, and Ames, 2016) his team further refined the combustor simulator to generate higher turbulence and to reduce the flow variation. In general, a combustor simulator mixes incoming streamwise air and lateral jets in crossflow, emulating the aerodynamics of a rich-burn combustor. The orientation and relative geometric dimensions reflect real combustor geometry. Ames (1990) reported turbulence intensity as high as 19% in the test section with slight anisotropy. The measured turbulence had higher fluctuations in the lateral direction aligned with the axis of the jets than in the streamwise direction. Ames also found evidence of

a non-zero Reynolds shear stress in certain combustor simulator configurations at the edge of the boundary layer.

The benefit of jets in crossflow methods is that they simulate the fundamentals of combustor turbulence by replicating the jets in cross flow aerodynamics. The realities of combustor turbulence, such as potential anisotropy and length scale of turbulence, do not have to be determined *a priori*. The downside of combustor simulation is that it requires space to condition the flow upstream of the test section. This can be challenging to implement on existing rigs.

In summary, conventional grids are not able to re-create the turbulence intensity levels that are present at the inlet to the high pressure turbine. Modified grids, such as blown girds or grids of moving bars, can increase the turbulence intensity levels to those of combustor turbulence. Combustor simulators, which mimic jets in cross flow, introduce further reality by setting up correct turbulence structures.

2.3 Effect of freestream turbulence on a flat plate

A number of studies have examined the aerodynamic impact of high freestream turbulence on a flat plate. These studies have mainly focused on the wall shear stress. This is because in external aerodynamics, the measure for lost performance is drag. Unsurprisingly, the concept of drag has been carried over into turbomachinery flows despite the fact that it is of little use in identifying the loss generation in a blade passage (Denton, 1993).

2.3.1 Rise in skin friction

Early measurements in grid turbulence (e.g. Hancock and Bradshaw, 1983 and Castro, 1984) studied the effect of grid generated turbulence on skin friction. Hancock and Bradshaw (1983) were the first to identify that turbulence length scale, as well as intensity, had an impact on skin friction on a flat plate. They used two turbulence girds of square bars and varied the distance from the grid to the flat plate leading edge in order to achieve a range of freestream turbulence intensities (1.8%-6%) and length scales (0.7δ-5δ). Measurements of skin friction taken with a grid at the inlet, C_f, were compared to measurements taken with no turbulence grid at the inlet, C_{f0}, at the same boundary layer Reynolds number, Re_θ. The reported rise in skin friction, $(C_f - C_{f0})/C_{f0}$, was 2-24% depending on turbulence intensity and length scale (Hancock and

Bradshaw, 1983). However, the published dataset does not tabulate C_{f0} and Re_θ, making it difficult to compare to other experiments or to de-couple the effect of length scale and turbulence intensity.

The use of jets in crossflow greatly extended the range of turbulence intensities which could be experimentally studied. Ames (1990), Thole and Bogard (1996), and Stefes and Fernholz (2004) carried out similar skin friction measurements on a flat plate with turbulence intensity of 10-20% in the freestream generated by jets in crossflow. Figure 2.5 shows the skin friction measurements of Ames (1990). Turbulence intensities of 7% to 15% in the freestream were generated with a combustor simulator. Ames did not take skin friction measurements in low freestream turbulence but used an empirical correlation to compare the rise due to combustor turbulence. Figure 2.5 shows that the skin friction is 15% higher than predictions with an empirical correlation based on low freestream turbulence data.

Stefes and Fernholz (2004) used oil film interferometry to measure a 34% increase in skin friction due to inlet turbulence of 12.8% (generated with jets in crossflow), compared to grid turbulence of 0.9% intensity at a consistent Reynolds number of $Re_\theta = 1{,}730$.

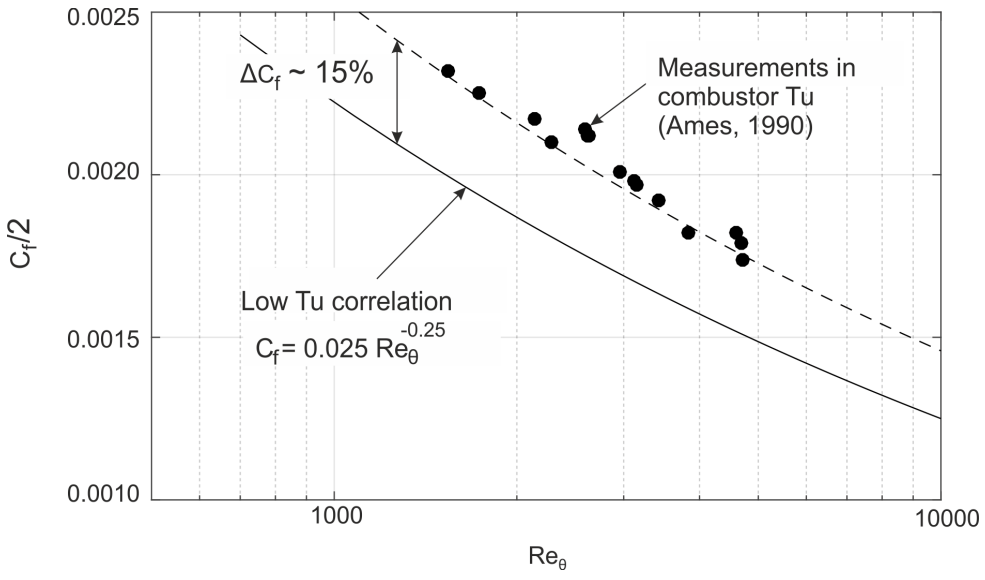

Figure 2.5: The measured impact of combustor turbulence on skin friction. Measurements in combustor turbulence, adapted from Ames (1990, data in Appendix H). Low turbulence correlation given by $C_f = 0.025 Re_\theta^{-0.25}$ (Kays, 1980).

Skin friction augmentation due to high freestream turbulence was confirmed in other facilities using a variety of different measurement techniques. However, most of the available data have been taken at inconsistent boundary layer Reynolds numbers, Re_θ. Sharp et al. (2009) measured a 19% rise in skin friction at a high freestream turbulence intensity of 10.5% (generated with an active grid) relative to low freestream turbulence intensity of 0.25% (no grid). However, the measured skin friction was taken at $Re_\theta = 2{,}460$ in low freestream turbulence and at $Re_\theta = 1{,}810$ in high freestream turbulence. Since skin friction is a function of Re_θ (Figure 2.5), care must be taken to compare measurements in high and low turbulence at the same Reynolds numbers.

Bons (2002) used a floating flat plate to measure a 16% increase in skin friction due to inlet turbulence of 11%, compared to grid turbulence of 1% intensity. Although the boundary layer Reynolds number was not reported, the Reynolds number based on axial distance along the flat plate, Re_x, was constant (Bons, 2002, Table 3). It is well known that the physical size of the boundary layer increases in the presence of high freestream turbulence. For example, at the same axial location on the flat plate, Dogan (2017) found the momentum thickness to be 46% larger in high freestream turbulence (Table 2.1). Therefore, measurements at constant Re_x in high and low freestream turbulence are likely to be at inconsistent Re_θ. The change in skin friction reported by many studies such as Bons (2002) and Dogan (2017) couple the effects of turbulence with Reynolds number and cannot be used to set a definitive trend.

In all of these studies, the shape of the boundary layer velocity profile was modified by the presence of high freestream turbulence. It was found to become fuller with increasing turbulence intensity (e.g. Figure 2.6a). Stefes and Ferhnolz (2004) measured a 13.5% reduction in the shape factor, $H_{12} = \delta^*/\theta$, due to inlet turbulence of 12.8%, compared to grid turbulence of 0.9% intensity.

Table 2.1: Boundary layer in high freestream turbulence (Dogan, 2017, Table 3.2).

Turbulence	$\boldsymbol{Re_x}$	$\boldsymbol{Re_\theta}$	$\boldsymbol{C_f}$
0.6%	2.2×10^6	3,830	0.00298
8.3%	2.3×10^6	4,870	0.00330
12.7%	2.3×10^6	5,590	0.00360

When normalized on inner units ($y^+ = yu_\tau/\nu$ and $U^+ = U/U_\tau$), the velocity profile was found to be self-similar near the wall (e.g. Figure 2.6b). The logarithmic-law of the wall, shown with a dashed line in Figure 2.6b, was found to be valid. On inner units, the difference in the velocity profiles was solely in the wake region ($y^+ > 400$ in Figure 2.6b), where the effect of freestream turbulence was to supress the wake.

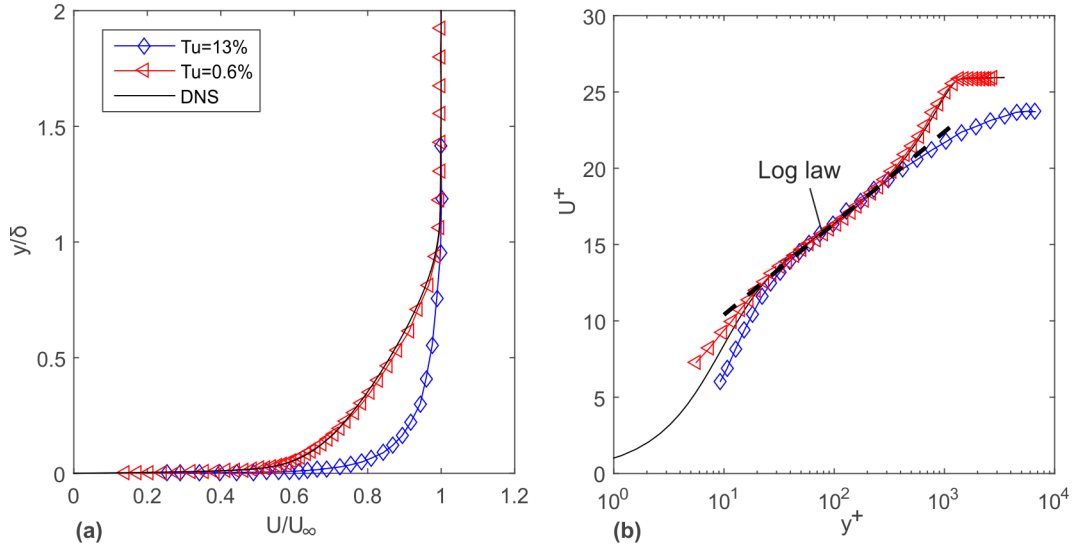

Figure 2.6: Impact of combustor turbulence on flat plate boundary layer. Mean velocity profile measured by Dogan (2016) and computed with DNS by Schlatter and Örlu (2010).

In conclusion, previous studies have found the effect of freestream turbulence is to cause a fuller velocity profile and therefore increase skin friction on a flat plate boundary layer. However, since skin friction varies inversely with boundary layer Reynolds number (e.g. $C_f = 0.025Re_\theta^{-0.25}$), comparison between boundary layer measurements made in high and low freestream turbulence must be made at a similar Reynolds number. The aforementioned studies have reported the results at inconsistent boundary layer Reynolds numbers (e.g. Table 2.1 and Figure 2.6). Therefore, a key motivation for this work is to study the effect of freestream turbulence at a consistent boundary layer Reynolds number.

2.3.2 Physical mechanism

By measuring the turbulent kinetic energy spectra through the boundary layer, Thole and Bogard (1996) found evidence that high freestream turbulence was able to penetrate deep into the boundary layer. The authors concluded that the rise in skin friction and the change in the velocity profile occurs because the large freestream turbulence eddies cause more mixing in

the boundary layer. Furthermore, the authors postulated that freestream turbulence eddies which are large in size are able to affect the smaller shear-generating scales near the wall.

Scale interaction in highly turbulent boundary layers was studied by Sharp et al. (2009) and Dogan (2016). In these studies, detailed spectral analyses of boundary layer hot wire measurements revealed two distinct peaks in the boundary layer in high freestream turbulence. The outer peak was caused by the freestream turbulence and occurred at a wavelength which corresponded to the turbulence generating device. The inner peak was caused by turbulence being generated at the wall. Dogan (2016) found that the large outer scales modulated the small near wall scales, thus confirming the early hypothesis of Thole and Bogard.

The theory of scale interaction is difficult to quantify practically because of an inconsistency in the definitions of freestream turbulence scales. The traditional length scale of turbulence is taken as the integral length scale, or the size of large coherent structures in the flow. On the other hand, studies in high turbulence, such as Hancock and Bradshaw (1983) and Ames (1990), propose that the most important length scale is the dissipation length scale, L_e, defined from Equation 2.3. This length scale physically represents the turn-over rate of large eddies, which in turn dictates the rate of decay of turbulent kinetic energy. Experimentally it is determined by measuring the streamwise development of freestream turbulence.

$$\bar{U}_\infty \frac{d(\overline{uu})_\infty}{dx} = -\frac{(\overline{uu})_\infty{}^{3/2}}{L_e} \tag{2.3}$$

Recent investigations by Sharp (2009) and Dogan (2017) describe yet another important length scale in high freestream turbulence, the most energetic length scale. It is the wavelength associated with a dominant peak in the pre-multiplied spectrum of turbulent kinetic energy. In a canonical boundary layer, the spectral peak close to the wall shows trace of the near wall cycle of streaks and streamwise vortices and always occurs at a fixed wavelength (normalised by shear velocity). In a turbulent boundary layer, a different spectral peak is found to dominate the flow and this is related to the freestream turbulence. An example of the spectral peak wavelength is presented later in the thesis, in Chapter 7 and 8.

The discrepancy in the various definitions of turbulent length scale suggests that the physical mechanism of scale interaction in high freestream turbulence is not well understood. Furthermore, the effect of turbulence intensity and length scale have not been investigated

independently at a constant Reynolds number. This shows that the fundamental mechanism responsible for augmented skin friction on a flat plate in high freestream turbulence is not well understood.

2.3.3 Summary

The response of a flat plate boundary layer to high freestream turbulence has been the subject of a number of investigations. The studies have been limited to skin friction, the shape of the velocity profile, and local turbulence statistics.

Measurements of skin friction show a rise in C_f with increasing freestream turbulence ranging from 13% to 34% relative to a low freestream turbulence baseline. Most of the data is reported at an inconsistent Reynolds number between high turbulence and the low turbulence baseline, which explains part of the scatter in C_f. In addition, the competing effects of turbulence length scale and turbulence intensity has made it difficult to establish a fundamental understanding.

Finally, the focus in existing literature on skin friction and drag is of little use in turbomachinery where the performance metric of importance is loss. The effect of combustor turbulence on dissipation has not previously been considered.

2.4 Effect of freestream turbulence on a turbine cascade

Several studies have examined the effect of freestream turbulence on turbine cascades. Most of these studies are confined to local skin friction and local heat transfer measurements. For example, Ames and Plesniak (1997) measured a 27% increase in local skin friction on an airfoil due to inlet turbulence of 12%, compared to grid turbulence of 1% intensity. Using the same experimental set up, Ames (1998) measured a 16% increase in local skin friction at a different location on the same airfoil. Few holistic studies have been done to consider the effect of combustor turbulence on a number of loss mechanisms in the turbine.

2.4.1 Impact on loss

Two questions are of interest for a turbine cascade: 1) how does combustor turbulence impact profile loss and 2) how does combustor turbulence impact endwall loss?

Ames and Plesniak (1997) measured the effect of combustor freestream turbulence on profile loss in a linear turbine cascade. They report that combustor turbulence (Tu=12% intensity) caused a 20% rise profile loss compared to grid turbulence (Tu=1% intensity).

Measurements on a transonic turbine cascade were also undertaken by NASA with low (0.4%) and high (8-15%) inlet turbulence intensity (Flegel et al., 2014). The high turbulence intensity was generated using a blowing grid. The midspan wakes in low and high turbulence, measured with a five hole probe downstream of the trailing edge, are shown in Figure 2.7. Like Ames and Pleskiank's experiments, the vane wakes measured in high freestream turbulence were wider and shallower. However, there was also an unexplained region of negative loss in the freestream in the high turbulence case. In contradiction to Ames and Pleskiank, Flegel concluded that the high freestream turbulence causes a reduction in profile loss.

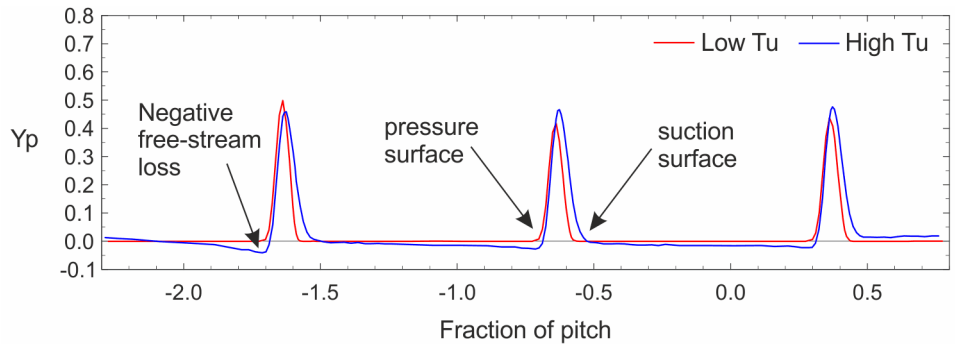

Figure 2.7: Midspan loss coefficient measured in low and high freestream turbulence. Adapted from Figure 15 of Flegel et al., 2014.

Flegel et al. (2014) also attempted to quantify the effect of high freestream turbulence on the endwall loss. However, the presence of the blowing grid doubled the size of the endwall boundary layer entering the turbine cascade, from 24% of span to 12% of span. Since endwall secondary flow is highly coupled with the inlet boundary size, no conclusion can be drawn from the endwall measurements.

Chowdhury et al. (2011) is the only study to investigate the effect of combustor turbulence on the overall loss coefficient of a turbine cascade. They found that combustor turbulence (Tu=14% intensity) causes a 55% - 93% rise in the overall cascade loss coefficient over grid turbulence (Tu<1% intensity), depending on the vane geometry. The reported breakdown of loss into profile and endwall loss, along with the reported uncertainties, is shown in Figure 2.8.

The first question is how does combustor turbulence impact profile loss? Figure 2.8 shows that the effect of combustor turbulence was to raise the profile loss by 99% in one vane configuration and by 146% in the second vane configuration. The large increase in profile loss is primarily attributed to transitional effects. Heat transfer mapping revealed that in low turbulence, the suction surface boundary layer remained laminar while in combustor turbulence, transition occurred at approximately 27% of surface length. In a real engine, the point of transition is typically set by the presence of cooling holes on the early suction surface. Therefore, a more appropriate comparison would be on a vane with a fully turbulent boundary layer or one where the transition point was fixed to be the same in low and in combustor turbulence.

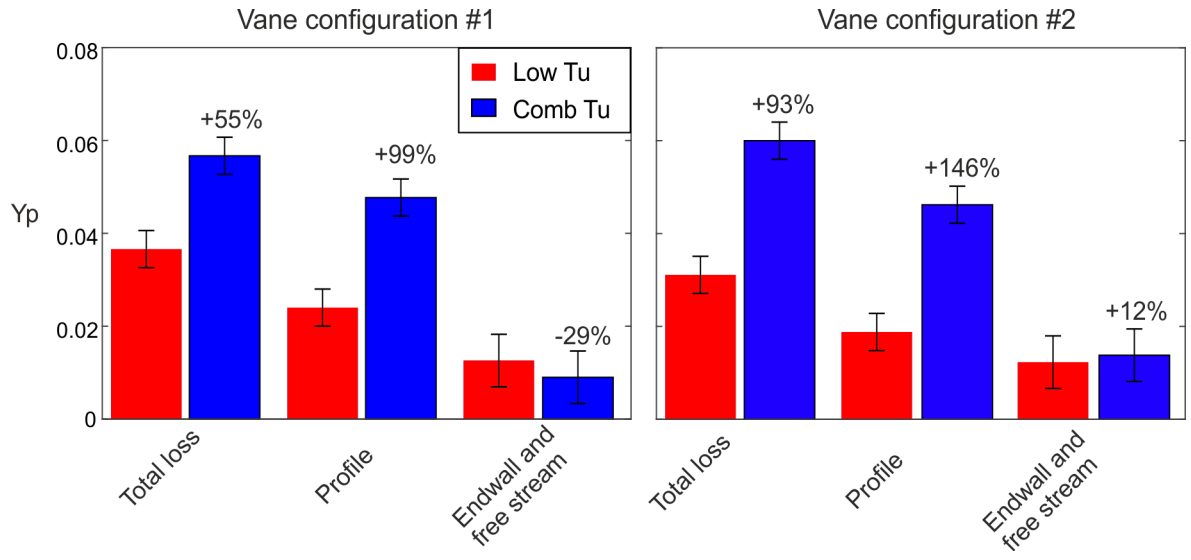

Figure 2.8: Impact of combustor turbulence on vane loss. Measured total pressure loss downstream of a vane cascade in low (<1%) and high (14%) freestream turbulence at exit Reynolds number of 1×10^6. Adapted from Table 2 in Chowdhury et al., 2011.

The second question is how does combustor turbulence impact endwall loss? Endwall loss was determined as the difference between overall loss and profile loss. Figure 2.8 shows that effect of combustor turbulence was to decrease endwall loss by 29% in the first vane configuration and to raise the endwall loss in the second vane configuration. Included in this definition of loss was the effect of loss in the freestream. However, because the effect of endwall loss and freestream loss are coupled, it is difficult to form a general conclusion on the effect of combustor turbulence on endwall loss alone.

2.4.2 Physical mechanism

The only study to offer insight into increased loss on a cascade was the study of Ames and Plesniak (1997). This study was limited to the profile and freestream loss. The authors attributed the measured increase in profile loss to three regions: suction surface boundary layer, freestream, and mixing in the wake. The source of the increased wake loss was found to be enhanced wake mixing caused by combustor turbulence. The cause of the increased freestream loss was partly attributed to turbulence production as the combustor turbulence was stretched by the vane acceleration. The cause of increased boundary layer loss was not discussed.

2.4.3 Summary

The response of a turbine bladerow to high freestream turbulence has only appeared in a limited number of studies. Most of the available data have been limited to local skin friction and profile loss. No comprehensive study exists which breaks down the effect of combustor turbulence on individual loss mechanisms in a turbine cascade consistently. There is a clear need to understand the complicated behaviour of loss in the turbine cascade in the presence of combustor turbulence.

2.5 Research questions

The literature review has shown four deficiencies in the current literature:

1. The first question addresses the nature of combustor turbulence. What is the shape and structure of combustor turbulence? Is combustor turbulence isotropic? Can the interaction of combustor turbulence and the downstream boundary layer be considered turbulence or is it unsteadiness? Chapter 4 will present measurements downstream of a new combustor simulator and address these questions.
2. The second question is regarding boundary layer dissipation in combustor turbulence. How does combustor turbulence change loss on a flat plate boundary layer? What are the physical mechanisms responsible? Chapters 5 and 6 will establish a framework for measuring dissipation in high freestream turbulence, and Chapter 7 will use the new framework to answer the aforementioned questions.
3. The third question is to do with loss on a turbine cascade. How does combustor turbulence change overall loss of a realistic bladerow? How does combustor

turbulence affect the profile and the endwall losses? Chapter 8 will present detailed measurements on a cascade to answer these questions.

4. Finally, a real engine application is considered. What is the effect of combustor turbulence on stage efficiency? Chapter 9 will apply the knowledge established in this research to quantify the effect on the efficiency of a turbine stage in the presence of combustor turbulence.

Chapter 3
Experimental Methods

Experimental results presented in this thesis were performed in an open-circuit, low Mach number wind tunnel at the Whittle Laboratory in Cambridge. This chapter details the methods used in producing the results.

3.1 Experimental configurations

The experimental matrix has four configurations which are shown in Figure 3.1. Two turbulence generators were used in the testing: a conventional turbulence grid and a combustor simulator. Two downstream working sections were used. The first working section was a flat plate, and the second was a linear turbine cascade.

The first research objective is to characterise the nature of combustor turbulence. This is done by measuring turbulence at the exit of the combustor simulator (configuration 2) and comparing it to the conventional turbulence grid (configuration 1).

The second research objective is to identify the physical mechanisms which are responsible for the rise in loss due to combustor turbulence. To address this question, the flat plate configurations 1 and 2 in Figure 3.1 were studied, because a flat plate boundary layer is much more accessible for detailed measurements and has a well-known canonical behaviour in low freestream turbulence.

The third research objective is to investigate effect of combustor turbulence on the loss mechanisms in a turbine cascade. To address this question, configurations 3 and 4 with a cascade were tested. The Harrison cascade (Harrison, 1989) was selected for the turbine test. This blade was chosen for two reasons. First, it has been extensively studied and is a well

understood baseline (e.g. Harrison, 1989, Denton and Pullan, 2012, Grewe, 2013). Second, the large scale of this cascade allows the loss to be determined with greater certainty.

The design of the combustor turbulence generator in configuration 2 and 4 was based on the work of Kingery and Ames (2016). In the design, 1/3 of the mass flow enters through slots in the back wall and 2/3 from the side through impingement jets. A turbulence grid installed in a rectangular duct replaced the combustor simulator for low turbulence tests in configuration 1 and 3. The grid was designed following Roach (1987) to have a lower turbulence intensity than the combustor turbulence but a similar length scale. At the inlet plane of the turbine control volume, the combustor turbulence intensity is 10% and the grid turbulence intensity is 1.3%. Details of the nature of inlet turbulence are discussed in Chapter 4.

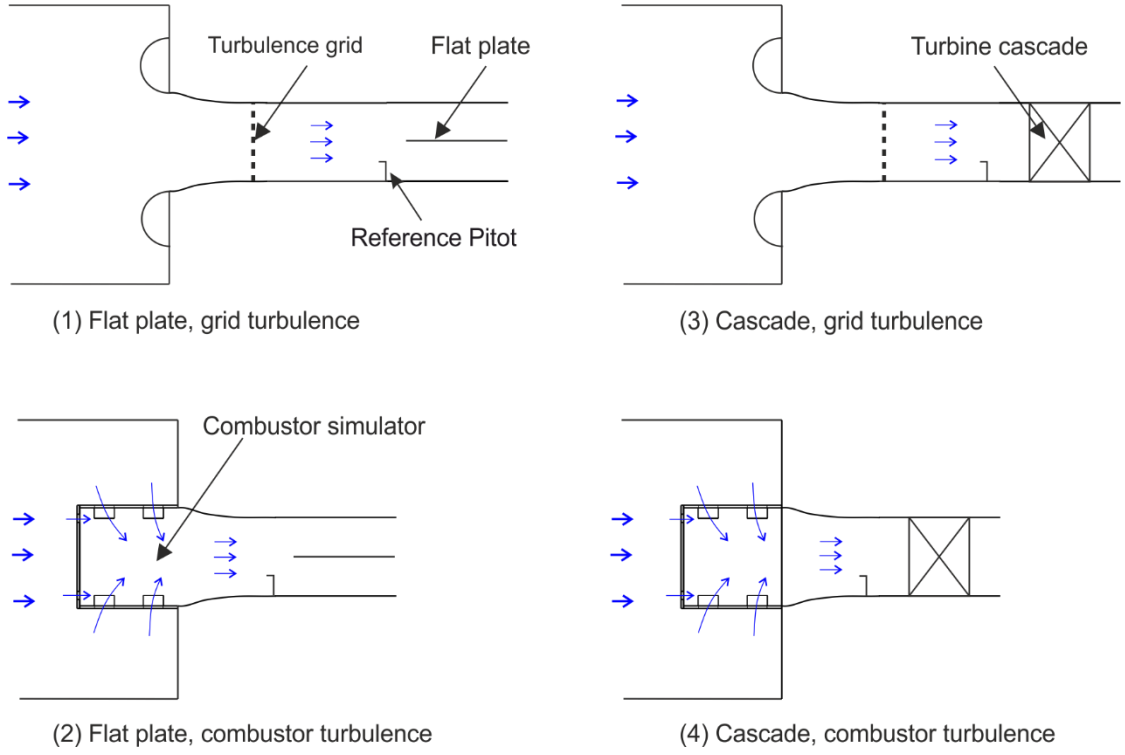

Figure 3.1: Schematic of the four experimental set up configurations.

The flat plate shown in configurations 1 and 2 was one meter long and was aligned with the centreline of the working test section. The leading edge was a smooth 6:1 ellipse, and the boundary layer was tripped immediately downstream of the leading edge with a thin metal hypodermic tube. Measurements were made with a single component boundary layer hot wire and a two component hot wire probe. Results from the flat plate experiments are discussed Chapter 7.

The cascade shown in configurations 3 and 4 was a linear cascade with four airfoils that are typical of high pressure turbine design. Measurements were made with a single component boundary layer hot wire, five hole probes, and surface static pressure tapings. Results from the cascade experiments are discussed in Chapter 8.

3.2 Instrumentation

Reference total and static pressures were recorded upstream of the test section inlet in order to maintain a constant operating point. In the flat plate configuration, a single reference Pitot probe (shown in Figure 3.1) was located at the flat plate midspan. In the cascade configuration, two reference Pitot probes were staggered in the pitchwise direction about the centre measured passage. Static pressure was recorded at the endwall at the same location as the Pitot probe.

Steady pressure measurements were taken using a 16-channel Scanivalve DSA 3217 with a range of 10 inches of water (2,489 Pa). The reference pressure on the DSA unit was the exit static pressure (which was equal to ambient pressure). The unit was initialized with a zero offset calibration at the start of every experiment to remove any offset caused by the module orientation.

Reference temperature was measured at the exit of the test section. When a hot wire was used, an additional thermocouple located on the hot wire stem was used to compensate for temperature drift. Temperature was measured with a K-type thermocouple and recorded on an Omega TC-08 logger.

The boundary layer and freestream turbulence was measured using a hot wire with constant temperature anemometry (CTA). The CTA probes were set up and recorded on the Dantec StreamLine Pro CTA System. Voltage readings of the hot wire were taken using a National Instruments PXIE system with an NI 4431 device. This unit logs four channels simultaneously at 102.4 kHz with a range of ± 10 V.

Atmospheric pressure and temperature were taken from a Vaisala PTH data logger placed near to the low speed wind tunnel rig. The atmospheric pressure and temperature were logged continuously over the course of an experiment. Reynolds number was established based on isentropic velocity, determined from the inlet total pressure and the exit static (atmospheric) pressure. Density, ρ, was taken at the exit. Viscosity was calculated from Sutherland's law

based on temperature measured at the exit. The appropriate length scale was the axial distance in the case of the flat plate or the true chord in the case of the cascade.

3.2.1 Steady state pneumatic measurements

A miniature flattened Pitot probe was used to traverse the inlet boundary layer in the cascade measurements. The boundary layer probe outer and inner diameters were 0.635 mm and 0.33 mm, respectively.

Two different five hole probes were used during the testing in a non-nulling operation to measure steady stagnation and static pressures and flow angles. The first was a bespoke miniature five hole probe, manufactured by Cambridge Aerothermal (Figure 3.2.a). It was mounted parallel to the blade span (z) direction and was inserted into the cascade through a slot in one endwall. The miniature probe had a sensing head diameter of 1.7 mm. The stem featured a kink design to allow measurements close to the cascade suction surface.

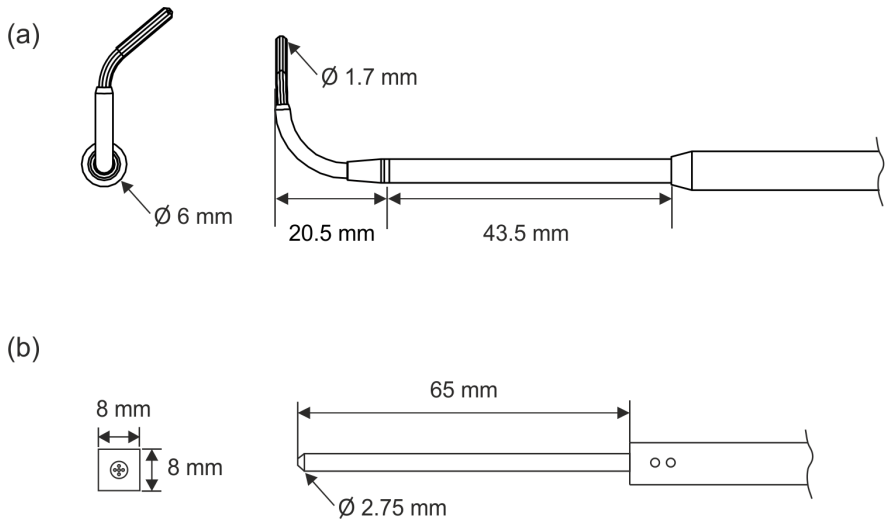

Figure 3.2: Dimensional drawing of the two five hole probes used in measurements.

The second was a straight five hole probe (Figure 3.2b) used by Grewe on the same cascade (Grewe, 2013). The probe sensing head diameter was 2.75mm. The probe was mounted on a probe arm at the exit of the cascade (Figure 3.18). The probe arm holding the probe was mounted on a rotary table which was used to position the probe to the mean flow exit angle.

The ports of the probe were connected to the pressure transducers with plastic tubes of approximately 300 mm in length. The short length of the plastic tubes reduced the volume of

air that is needed to fill from the probe head to the pressure transducer, minimising the settling time required to less than 1 second.

Both five hole probes were calibrated using the same methodology. The probe calibration map was determined by pitching and yawing the probe in 2° increments in a calibration tunnel. Standard calibration coefficients, defined in Equation 3.1, were used to relate measured pressures to flow properties.

$$
\begin{aligned}
C_{\alpha} &= \frac{P_2 - P_4}{P_5 - 0.25(P_1 + P_2 + P_3 + P_4)} \\
C_{\beta} &= \frac{P_1 - P_3}{P_5 - 0.25(P_1 + P_2 + P_3 + P_4)} \\
C_{Po} &= \frac{P_o - P_5}{P_5 - 0.25(P_1 + P_2 + P_3 + P_4)} \\
C_{Ps} &= \frac{P_o - P_s}{P_5 - 0.25(P_1 + P_2 + P_3 + P_4)}
\end{aligned}
\tag{3.1}
$$

The five hole probe calibration was performed in a low-noise calibration tunnel over ±35° in pitch and yaw (Figure 3.3). The probe was positioned in the centre of a 110 mm diameter nozzle at approximately 0.2 nozzle diameters downstream. To fix the position of the probe in the jet through all pitch and yaw angles, an offset arm was used which set the probe tip at the centre of rotation. Reference Pitot and static probes were mounted on the plane just upstream and downstream of the probe in the nozzle jet core. Relative to the nozzle diameter, the size of the probes was assumed not to cause significant blockage. Calibrations were performed over the range of velocities anticipated in the cascade but the maps showed no significant Reynolds number dependence. In Figure 3.3, the overlaid cascade measurements are located in a well-defined region of the map.

The total magnitude of error in the derived flow quantities was determined from the bias and the precision errors of the independent measurements and the uncertainty of the calibration. In the freestream, where the probe was aligned with the flow, the anticipated error is ±0.1° in flow angles, ±0.4% in local stagnation pressure normalized by dynamic head, and ±1% in local static pressure normalized by dynamic head. In the wake or in the secondary flow region, where the incidence angle onto the probe is larger, the anticipated error is ±1° in flow angles, ±5.5% in local stagnation pressure normalized by dynamic head, and ±6.4% in local static pressure normalized by dynamic head.

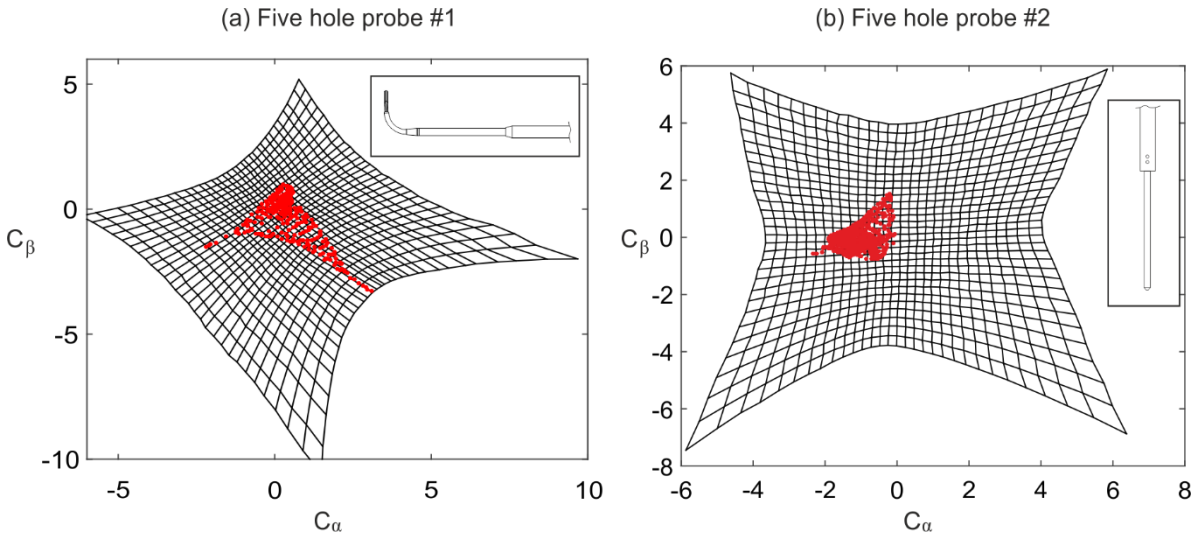

Figure 3.3: Five hole probe calibration maps (black lines) and cascade data (red symbols).

3.2.2 Unsteady single component hot wire

Two types of single component hot wire probes were used: a straight miniature hot wire (Dantec 55P11) was used to measure freestream turbulence and a boundary layer gold plated hot wire (Dantec 55P05) was used to measure the boundary layer velocity and turbulence.

The boundary layer hot wire is shown in Figure 3.4. The diameter of the hot wire was 5µm, the prong spacing was 3mm and the sensing width was 1.3 mm. It was used to measure boundary layers with thicknesses ranging from 6mm at the mid suction surface of cascade to 22 mm at the aft most location on the flat plate. The size of the probe allowed for resolution to within microns of the wall.

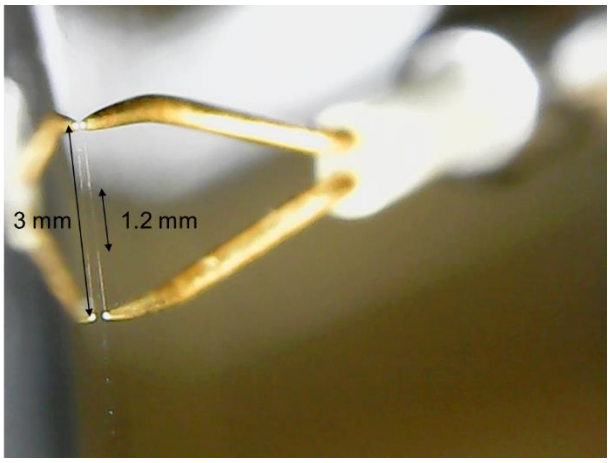

Figure 3.4: Photograph of the boundary layer hot wire probe.

The hot wire was assembled into a short probe support stem (Dantec unit 55H20) which was connected, via a four metre BNC cable, to the hot wire anemometer (Dantec Streamline). The anemometer contained a constant temperature bridge and signal conditioner and was used to set the overheat ratio at the start of each test. The anemometer was also used to measure the frequency response of the wire to velocity fluctuations. This was carried out by applying a square wave signal to top of the bridge. The time it takes for the bridge to get into balance, or the time it takes for the signal to drop by 97% of its peak, is the time constant, Δt, of the system. The cut off frequency of the wire is related to the time constant by Equation 3.2 (Brunn, 1995). A typical time constant was 0.012 ms which gives a cut off frequency of 64 kHz.

$$f_c = \frac{1}{1.3\Delta t} \tag{3.2}$$

The signal from the anemometer was acquired via an A/D converter board (National Instrument unit USB 4431) at 102.4 kHz and saved as data-series in a computer. Figure 3.5 shows sample measured spectra in grid and combustor turbulence. Since the sampling frequency sufficiently exceeds the frequency content of the bulk of the turbulent energy, the Nyquist criterion is met.

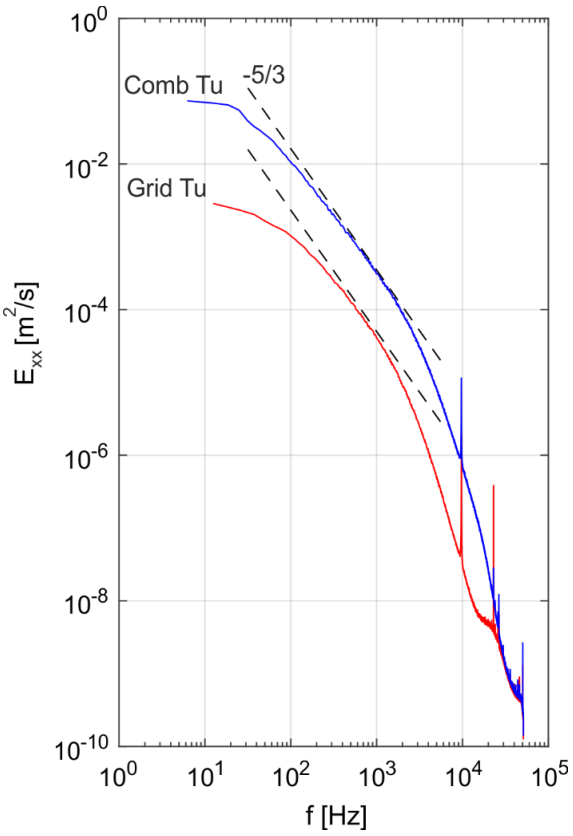

Figure 3.5: Example of hot wire measured turbulence spectrum.

In Figure 3.5, the Kolmogorov 1941 prediction with slope of -5/3 is also included for comparison. The hot wire clearly resolves the inertial range and well into the dissipation range both in grid and in combustor turbulence.

The hot wire was calibrated following the method outlined by Brunn (1995, Ch. 4.3). The calibration tunnel was the Dantec Calibrator System which is capable of providing low turbulent flow at a range of speeds between 0.5 m/s and 60m/s. The hot wire and a thermocouple were set up perpendicular to the nozzle, about one diameter downstream of the nozzle exit (Figure 3.6). The entire system was enclosed in a box with an open top to reduce the impact of ambient air draft (not pictured in Figure 3.6). The flow velocity was determined by measuring the stagnation pressure in the settling chamber, P_0, relative to the ambient pressure. One diameter downstream from the nozzle exit, the static pressure is equal to atmospheric pressure. The velocity was determined from $P_0 - P_{atm} = \frac{1}{2}\rho U^2$.

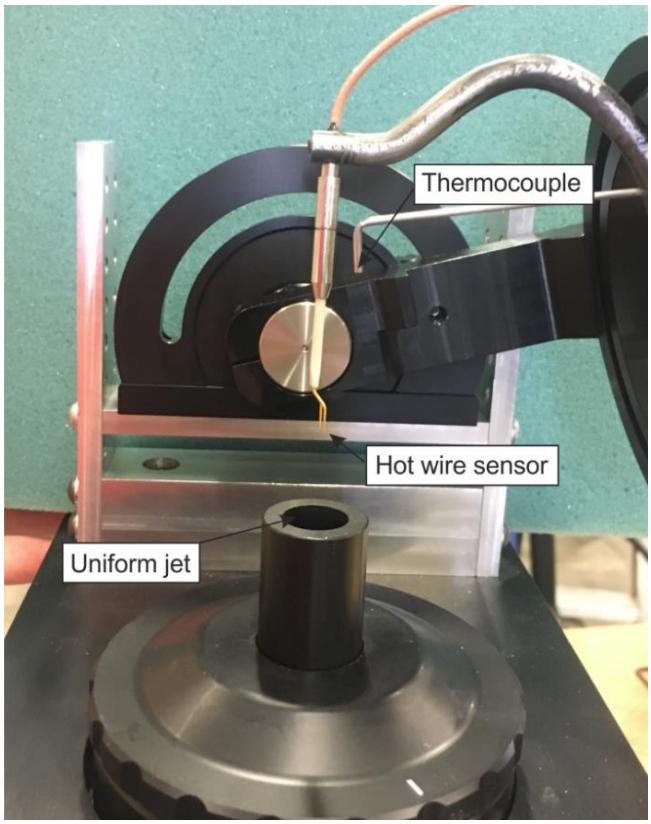

Figure 3.6: Photograph of the hot wire calibration system.

King's Law (Brunn, 1995) was used to establish the relationship between flow velocity, U, and the hot wire voltage, E, shown in Equation 3.3.

$$E^2 = A + BU^n \tag{3.3}$$

In Equation 3.3, the value for *n* was determined by minimising the error between the data and the fit. Typical values of *A*, *B*, and *n* were 0.6, 1.86 and 0.32 respectively.

Typically, 10-15 points were measured between 2 m/s to just above the maximum velocity (which was 20 m/s in the flat plate and ranged from 25 m/s to 55 m/s through the cascade). A sample calibration map is shown in Figure 3.7. There are nine calibration points, and the fit according to Equation 3.3 represents the relationship well. Figure 3.7 also shows that the hot wire calibration map covered the maximum and minimum values of velocity measured during an experiment.

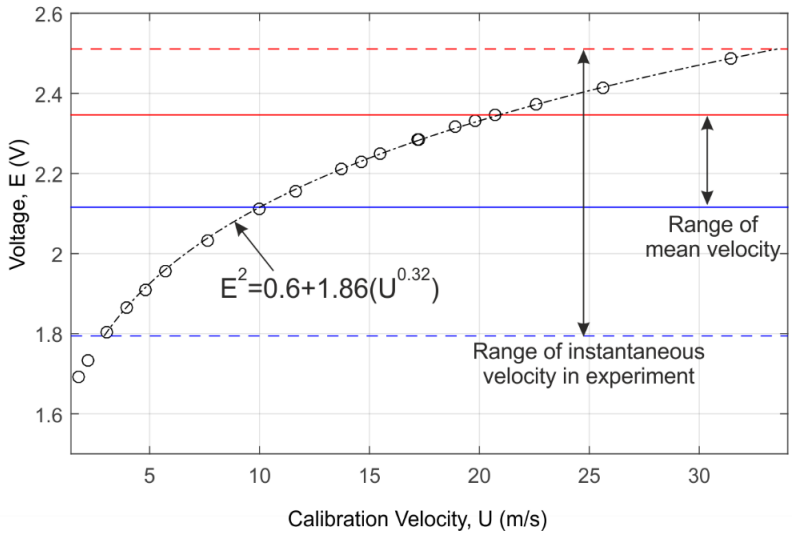

Figure 3.7: Example of a hot wire calibration map.

To avoid bias due to temperature drift, the hot wire voltage was adjusted using Equation 3.4 (Brunn, 1995, p. 215).

$$E_{corr} = E_{meas}\left(\frac{T_w - T_0}{T_w - T_{meas}}\right)^{0.5} \tag{3.4}$$

The temperature of the wire, T_w, is a property of the overheat ratio and the wire properties.

$$T_w = T_0 + \frac{OHR}{\alpha_0} \tag{3.5}$$

The overheat ratio (OHR) was typically set to 0.8, and the temperature coefficient of resistance, α_0, for the Dantec wires was 0.36%/K and the wire cold temperature, T_0, was typically 295 K. The typical wire temperature was 518 K.

To avoid bias due to near wall conduction, the hot wire voltage was adjusted using near wall correction, shown in Equation 3.6 (Cox, 1957):

$$E^2 = A\left(\frac{E_0^2(y)}{E_0^2(\infty)}\right) + BU^n \tag{3.6}$$

The still air voltage, E_0, was obtained by traversing a hot wire away from the wall while there was no flow in the tunnel. Near wall effects were found to persist up to 1.2 mm away from the wall. All velocity profiles measured with a boundary layer hot wire were adjusted in the same manner.

Mean and fluctuating velocities were determined from the instantaneous hot wire velocity trace following Equation 3.7:

$$U(t) = \overline{U} + u(t) \tag{3.7}$$

Turbulence intensity was calculated by:

$$Tu = \frac{\sqrt{\overline{uu}}}{\overline{U}} \tag{3.8}$$

Spectral analysis was used to analyse the scales of turbulence. The power spectral density was calculated from the discrete Fourier transform of the fluctuating velocity, $u(t)$. The spectrum shows the amount of energy which is available at a given frequency or wavenumber. The integral of the spectrum is the variance of the signal (Bendat and Piersol, 1968, Equation 1.37).

$$\overline{u^2} = \int_0^\infty E_{xx}(f)df \tag{3.9}$$

Signal windowing was performed through Welch power spectral density estimate in MATLAB (Figure 3.8, left hand side). A windowing parameter was used to divide the signal into overlapping segments from which spectra were determined. The final spectrum is the average of the segment spectra.

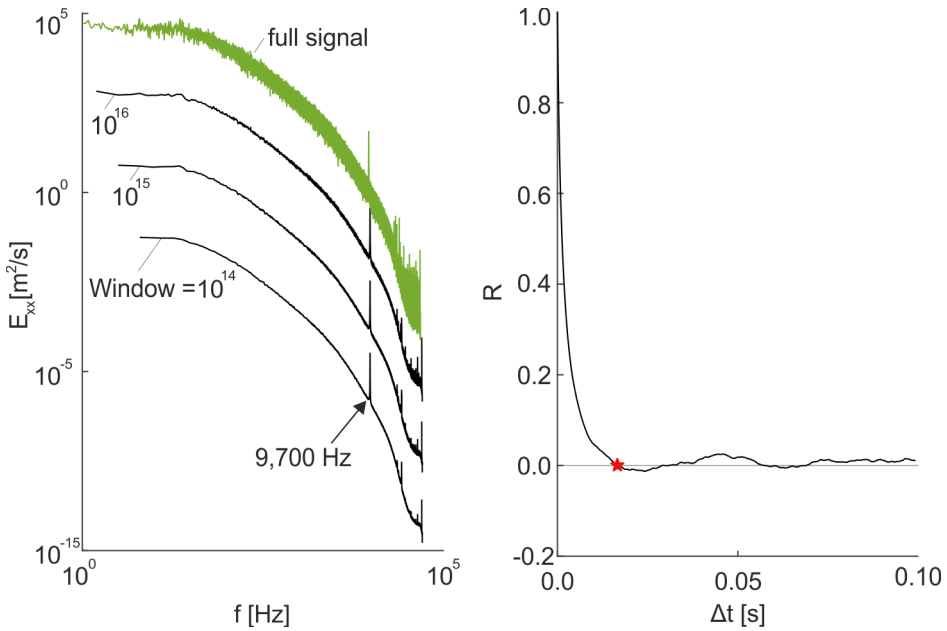

Figure 3.8: Example of hot wire power spectrum (left) and autocorrelation (right). Spectra are staggered relative to the lowest spectrum. From bottom to top, the offset of each spectrum relative to the lowest one is two, four and six decades.

A small window makes more segments and yields a smooth spectrum but attenuates the signal at low frequencies (akin to high-pass filtering). A very large window (e.g. the size of the full signal) results in a noisy spectrum which can mask important frequency trends. The effect of the windowing parameter is illustrated in Figure 3.8 (left hand side). Windowing and averaging the spectrum results in a high-pass filter error which could be as large as 3% (Table 3.1). For every given dataset, the windowing function was set up to reduce the error between the left hand side and right hand side of Equation 3.8 to less than 1%.

Table 3.1: The effect of windowing parameter in predicting turbulence intensity.

Window length	$\sqrt{\overline{u^2}}$ $[m/s]$	$\sqrt{\int_0^\infty E_{xx}(f)df}$ $[m/s]$	$Error$
10^{14}	2.44	2.36	3.2%
10^{15}	2.44	2.34	1.7%
10^{16}	2.44	2.42	0.9%

Figure 3.8 shows high frequency noise, particularly a spike at around 9.7 kHz. This spike was present in combustor and gird turbulence data and was likely caused by electronic noise in the system. The effect of high frequency noise on the overall energy content was minimal.

Low-pass filtering the signal at 9.7 kHz resulted in less than 0.1% error in the overall turbulent kinetic energy.

Taylor's hypothesis of frozen turbulence was used to relate spatial variation to temporal variation at a point. This hypothesis assumes that a 'frozen' turbulence structure convects past the measurement point with the mean velocity (Brunn, 1995).

$$\frac{\partial}{\partial x} = -\frac{1}{\overline{U}}\frac{\partial}{\partial t} \tag{3.10}$$

Using this hypothesis, the wavenumber spectrum is related to the frequency spectrum by:

$$E_{uu}(\kappa) = \frac{\overline{U}}{2\pi}E_{uu}(f) \tag{3.11}$$

where the wavenumber is given by $\kappa = 2\pi f/\overline{U}$. The wavenumber is converted to a wavelength by the definition $\lambda = 2\pi/\kappa$.

Taylor's hypothesis was also used to relate the integral length scale to the integral time scale:

$$\Lambda_{\text{int}} = \overline{U}T_{int} \tag{3.12}$$

where the integral time scale, T_{int}, is calculated from the integral of the autocorrelation function. The autocorrelation function describes the time it takes for a signal to become uncorrelated with itself (i.e. the time it takes for a coherent structure to convected past a sensor). It is given by Equation 3.13 and is presented in Figure 3.8, right hand side.

$$R(\Delta t) = \frac{\overline{u(t)u(t+\Delta t)}}{\overline{uu}} \tag{3.13}$$

The integral time scale, T_{int}, was calculated from the integral of the autocorrelation function to the first zero crossing.

3.2.3 Unsteady double component hot wire

Lateral components of velocity were measured with a custom built two-component Dantec hot wire (also called a cross wire). This was required to calculate the isotropy of turbulence and to determine the magnitude of Reynolds stresses in the flow.

Two platinum plated tungsten wires, 5 μm in diameter, were strung between two pairs of 45° slanted prongs, as shown in Figure 3.9. The wires were located in parallel planes separated by a distance of 1 mm. The wire mounts in an axis parallel to the direction of the main flow so that the predominant flow vector approaches the two wires at 45°. This configuration allows for instantaneous measurements of two velocity components in the plane of the wire, the streamwise component and one lateral component. By orientating the probe 90° about the stem, a second configuration allows instantaneous measurements of the streamwise component and the other lateral component. Of the total nine components in the Reynolds stress tensor, the cross wire could resolve only 7 ($\overline{uu}$, $\overline{vv}$, $\overline{ww}$, $\overline{uv}$, $\overline{vu}$, $\overline{wu}$, and $\overline{uw}$).

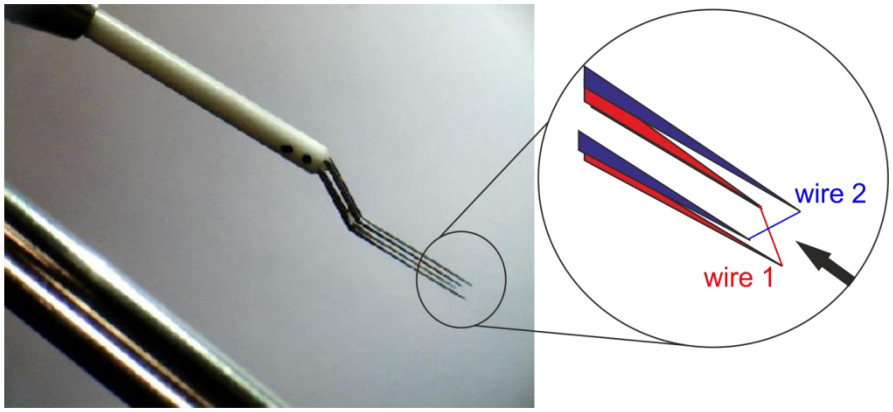

Figure 3.9: Photograph and schematic of cross wire.

The cross wire probe was mounted on a rotary table and rotated through ±65° about the centre of the calibration jet. To calibrate the cross wire, an angle sensitivity was first performed to determine the angle of each wire relative to the set up. For an ideal and infinitely long hot wire, the parallel component of velocity will have no cooling effect. When placed into the flow at an angle, the hot wire will respond primarily to the component of velocity normal to the wire.

The angle of maximum response for each wire was determined by fitting a polynomial over the relatively flat top of the curve. Figure 3.10 shows an example of the cross wire response to yaw. On average, the maximum response of wire 1 and wire 2 occurs at 44.4° and -45.3°,

respectively. At these yaw angles, the wires are perpendicular to the flow. The difference between the two max-response angles is 89.7°. Ideally these should add up to 90°, but the 0.3° error was determined to be acceptable.

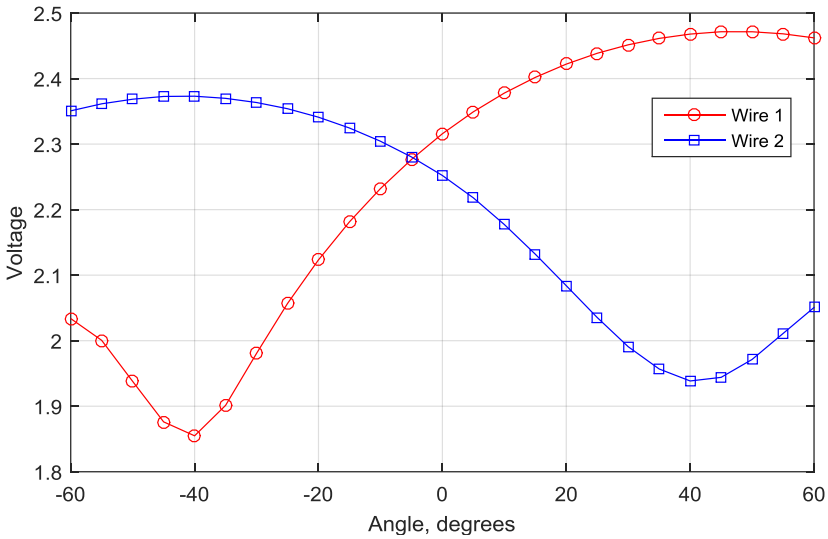

Figure 3.10: Example of cross wire response to yaw.

The two wires of the probe were then independently calibrated through a range of velocities at their maximum response angle. Equation 3.2 was used to determine the relationship between voltage and velocity in the same manner as for a single-component hot wire.

The yaw response of the wire was determined by measuring the effective cooling velocity, U, relative to the total flow velocity, U_∞. The yaw response function for the cross wire was given by Hinze (1975, p. 127), shown in Equation 3.13.

$$U = U_\infty[\cos^2(90-\alpha) + k_{xw}^2 \sin^2(90-\alpha)]^{0.5} \tag{3.13}$$

The term $(90-\alpha)$ is the yaw angle of the wire. The cross wire constant, k_{xw} was determined by fitting the measured response, shown in Figure 3.10, to Equation 3.13 and found to be 0.04. A value of $k_{xw} = 0$ would represent an ideal, infinitely long hot wire that was insensitive to the cooling effect of velocity parallel to the wire. Stem effects and a finite wire thickness, however, mean that the wire is able to recover some the parallel component cooling effect, which is captured by the term $k_{xw}^2 \sin^2(90-\alpha)$ in Equation 3.13.

Figure 3.11 shows that the yaw response function is the same at four velocities for small yaw angles. At high flow angles, approximately 40°, away from maximum response, there is evidence of Reynolds number dependency.

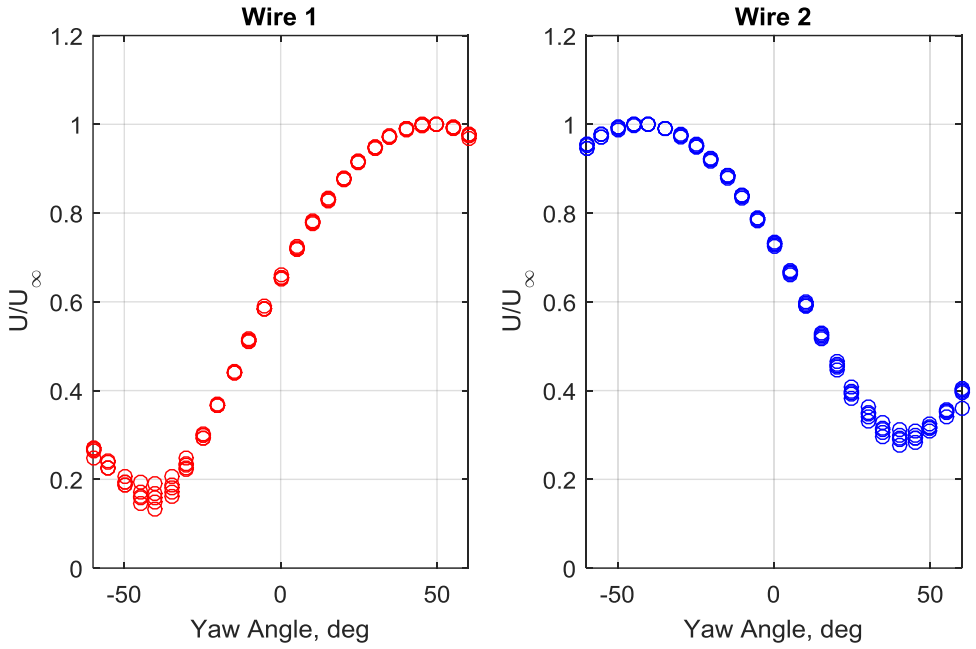

Figure 3.11: Example of cross wire calibration.

The relationship between two perpendicular components of velocity (e.g. u and v) can be expressed following the method described by Sagrado (2007). The perpendicular component of the velocity vector are given by Equation 3.14.

$$u = \frac{U_2 F_1^2(\alpha_1) + U_1 F_2^2(\alpha_2)}{F_1^2(90-\alpha_1)F_2^2(\alpha_2) + F_1^2(\alpha_1)F_2^2(90-\alpha_2)}$$

$$v = \frac{U_1 F_2^2(90-\alpha_2) - U_2 F_1^2(90-\alpha_1)}{F_1^2(90-\alpha_1)F_2^2(\alpha_2) + F_1^2(\alpha_1)F_2^2(90-\alpha_2)} \quad (3.14)$$

In Equation 3.14, U_1 and U_2 are the velocities measured by wire 1 and wire 2, respectively. The functions $F_1(\alpha_1)$ and $F_2(\alpha_2)$ are given by Equation 3.15.

$$F_1^2(\alpha_1) = [\cos^2(\alpha_1) + k_1^2 \sin^2(\alpha_1)]^{0.5}$$

$$F_2^2(\alpha_2) = [\cos^2(\alpha_2) + k_2^2 \sin^2(\alpha_2)]^{0.5} \quad (3.15)$$

A verification test showed that the method of calibration is accurate in the range of ±20° across the range of velocities expected in the turbulent boundary layer.

3.3 Flat plate test section

The first working section which was tested is a flat plate with zero pressure gradient. The aim of these tests was to determine the effect of combustor turbulence on a boundary layer with no acceleration or surface curvature. Measurements were made both with a single component boundary layer hot wire and with a two component hot wire probe discussed above. Static pressure measurements were recorded on wall tapings along the flat plate midspan.

The flat plate (1,000 mm x 685 mm x 10 mm) was mounted vertically in the middle of a rectangular test section downstream of the turbulence generating device (Figure 3.12). The plate was manufactured from stainless steel. It had an elliptical leading edge of a 6:1 ellipse with three pairs of symmetric pressure tapings. A trailing edge tailboard was used to adjust the stagnation point for zero incidence. The boundary layer was tripped downstream of the leading edge with a 0.4 mm cylinder.

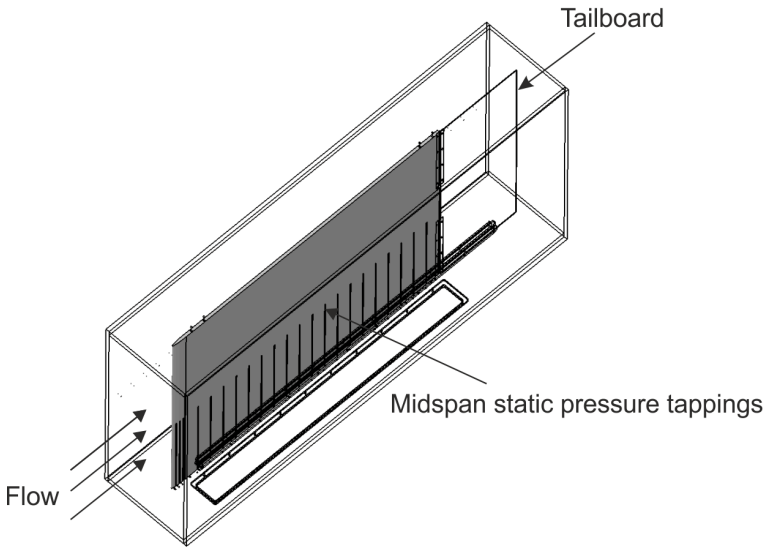

Figure 3.12: CAD model of flat plate test section.

3.3.1 Boundary layer traverse

Measurements of the turbulent boundary layer were performed at the plate midspan in thirteen different streamwise stations spaced 50 mm apart. Figure 3.13 is a photograph of the boundary layer hot wire during a typical velocity profile traverse.

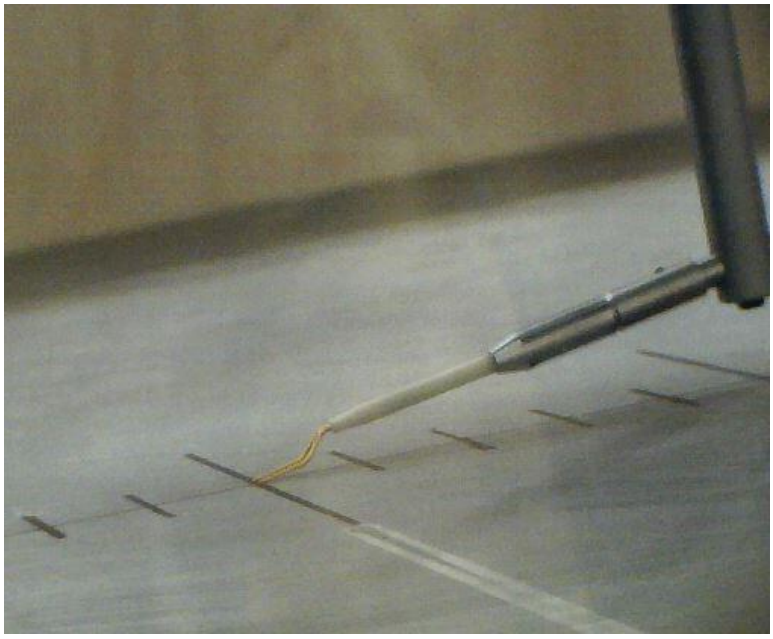

Figure 3.13: Photograph of boundary layer hot wire traverse set up.

The hot wire was moved through the boundary layer on a precision grade Parker 404XR traverse table which had an accuracy of 14 μm. The wall position was determined at the start of every experiment by first establishing electrical contact between the cold (no voltage) hot wire and the steel surface while the tunnel was on. Electrical contact was established with a resistance meter which had a lead from the flat plate and a lead from the hot wire cable. Initially, the hot wire was positioned at a safe distance of approximately 5mm away from the wall. In this case, the circuit was not completed and the resistance meter read zero resistance. Next, the hot wire was gradually stepped closer to the wall in micro steps ranging from 500 to 12.5 μm. Each micro step was manually input into the traverse control program and the resistance between the hot wire and the flat plate was checked on the resistance measurer. Once the hot wire prongs made contact with the wall, the circuit was completed and the resistance meter showed a non-zero voltage. Since the actual hot wire is soldered in the middle of the prongs, lightly touching the outside of the prongs to the flat plate did not damage the sensing element. After the zero position was recorded, the wire was moved out into the freestream and set to operate, and the measurement traverse began. Approximately 30 points were recorded inside the boundary layer and 15 more in the freestream. During the measurement traverse, the closest measurement to the wall was approximately 100 μm.

3.3.2 Wall fitting routine

To determine integral parameters, the discrete measured velocity profile needed to be converted to a smooth profile which extended all the way to the wall. The method of interpreting the velocity profile between the last measured point to no-slip at the wall is called wall fitting.

The measured mean velocity profile was fit to a canonical boundary layer following the method of Rodríguez-López et al. (2015). An output of this fitting method is the shear stress velocity, u_τ, which is used to calculate skin friction. This procedure of determining skin friction has been recently validated against oil film interferometry in high freestream turbulence flows by Esteban et al. (2017). In freestream turbulence of 12.6%, the error between the skin friction predicted using the wall fitting routine and oil film interferometry was less than 0.2%.

Figure 3.14 shows a typical turbulent boundary layer at Re_θ=2,000. The solid black line is from DNS with very low freestream turbulence (Schlatter and Örlu, 2010). The red circles are measurements in grid turbulence. The error bars represent ±2% velocity uncertainty determined from the hot wire calibration. The red solid line is the fit to the data. Figure 3.14 shows that the agreement between measured data, DNS, and the fit is very good.

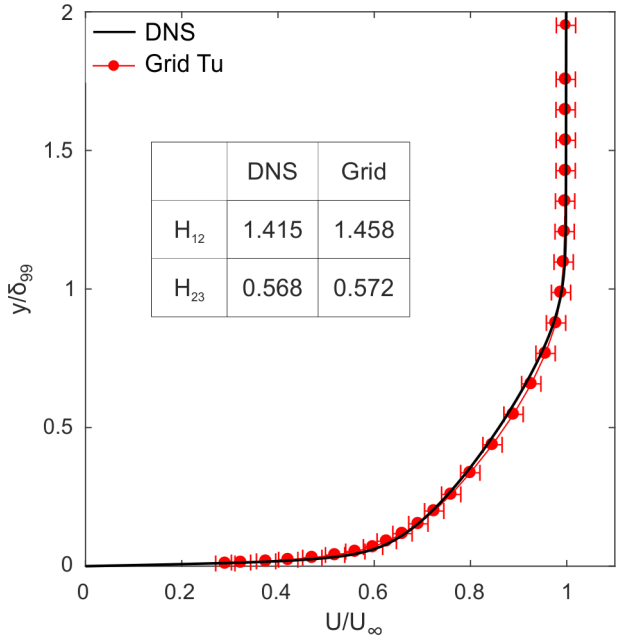

Figure 3.14: Measured and calculated velocity profile of a flat plate boundary layer. DNS calculations are after Schlatter and Örlu (2010).

The shape factors, H_{12} and H_{23}, are listed in Figure 3.14. The difference between DNS and the measured boundary layer are small and can be attributed to the uncertainty in determining the boundary integral parameters. In general, the agreement between DNS and the boundary layer integrated values measured in grid turbulence is very good.

3.3.3 Skin friction and dissipation

Skin friction on the flat plate was determined in two ways: a direct method and an indirect method. The direct method involves fitting a canonical velocity profile to the measured velocity and using the resulting u_τ to calculate skin friction. The indirect method is based on the rate of growth of momentum thickness. Chapter 6 will show that care needs to be taken to account for additional Reynolds stress shear in the freestream for the case of combustor turbulence. However, when this is accounted for, the two methods of determining skin friction agree to within 4%. The flat plate dissipation coefficient was determined with the indirect method, i.e. the growth of the energy thickness.

3.3.4 Uncertainty analysis

The overall error was determined from square root of squared bias and precision errors. For derived quantities, such as skin friction, relationship between the measured parameters ($u_\tau \ and \ U_\infty$) and the derived parameters was included in the analysis.

To determine the bias error of the integral properties and the skin friction, the fitting routine was tested against an external data set of velocity profiles on a flat plate in low freestream turbulence (Österlund, 1999). The detailed profiles of Österlund were truncated to have similar near wall resolution and boundary layer sampling. In evaluating the 70 profiles, it was found that the bias error in boundary layer integral parameters due to the fitting routine and near wall resolution was ±0.85% to 95% certainty. The bias error in skin friction was ±0.55%.

The precision error was determined by repeating the measurement five times on the same day in the same conditions. The precision error in integral measurements was found to be ±0.92% in grid turbulence and ±2.3% in combustor turbulence, to 95% certainty. The precision error in skin friction was ±1.7% in grid turbulence and ±0.55 in combustor turbulence.

The uncertainty of the boundary layer integral parameters ($\delta^\star, \theta, \delta_e$) was determined to be within ±1.2% in grid turbulence and ±2.5% in combustor turbulence. The uncertainty of skin friction measured directly from the near wall velocity profile is ±3.6% in grid turbulence and

±1.6% in combustor turbulence. The uncertainty in determining skin friction from the indirect method, $C_f = 2(d\theta/dx)$, was found to be ±3% for grid turbulence and ±6.5% for combustor turbulence.

3.4 Cascade

The second working section which was tested was a linear turbine cascade. The Harrison cascade (Harrison, 1989) was chosen for the turbine section, due to its previous extensive study (e.g. Harrison, 1989, Denton and Pullan, 2012, Grewe, 2013). The blade is specifically designed to have large secondary flow structures so that the changes in secondary flow can be studied with great fidelity.

The cascade has four blades with a span of 300 mm, true chord of 278 mm, and axial chord of 222 mm. Inlet flow was 40° and exit flow was -65.5° relative to axial. The trailing edge thickness was 2.2 mm. The Reynolds number of the flow, based on true chord and exit velocity, was 800,000 with an exit Mach number of 0.14.

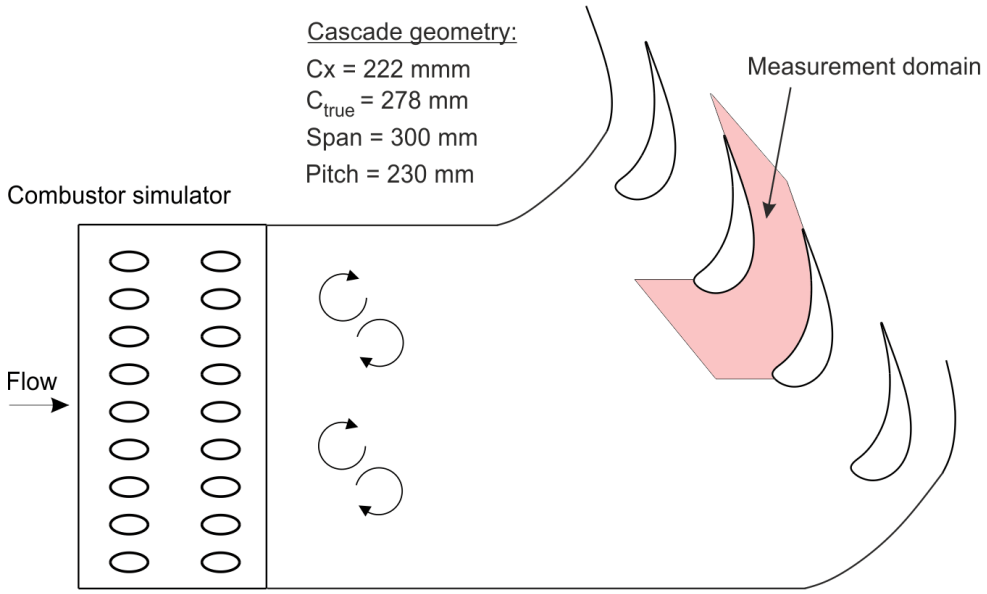

Figure 3.15: Schematic of cascade set up with combustor simulator.

The cascade control volume is shown in Figure 3.16. The inlet plane was located 50% axial chord upstream of the leading edge, and the exit plane was located 21% axial chord downstream of the trailing edge.

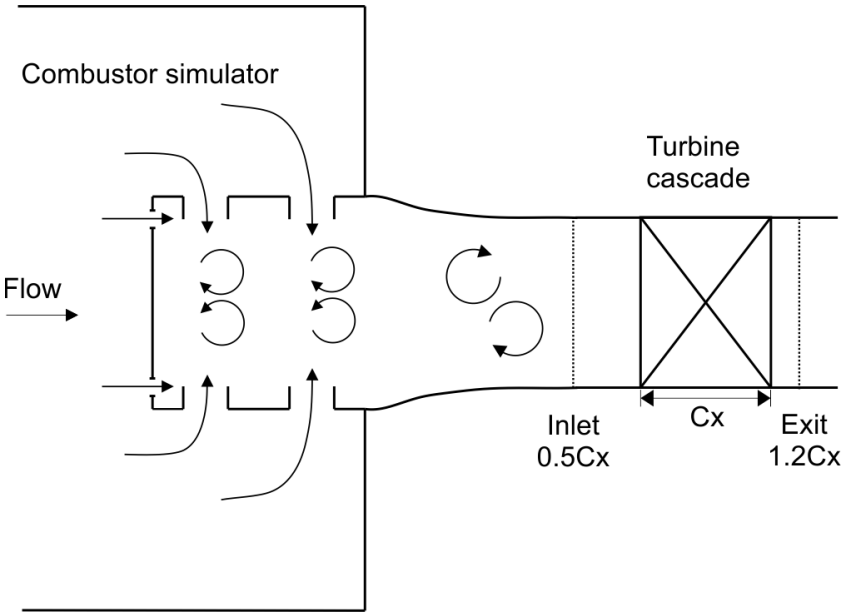

Figure 3.16: Schematic of turbine control volume.

The inlet boundary layer, shown in Figure 3.17, was measured with a flattened Pitot probe at the inlet plane. The inlet boundary layer thicknesses are 6.3% and 8% of span for the grid and combustor case. The shape factors (H_{12}) in grid and combustor turbulence are 1.35 and 1.27, respectively.

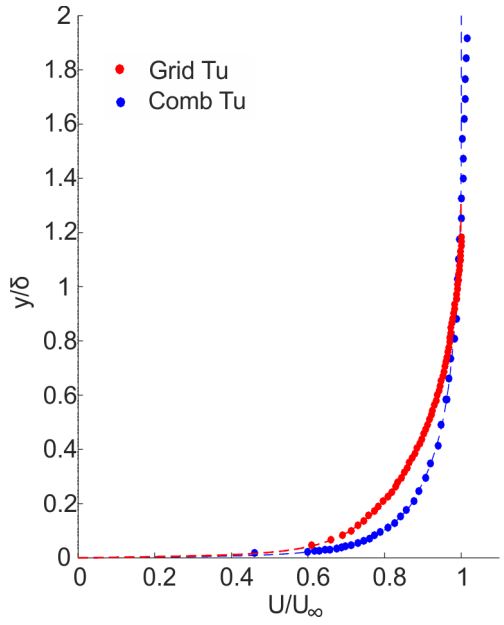

Figure 3.17: Measured boundary layer profile at the turbine cascade inlet.

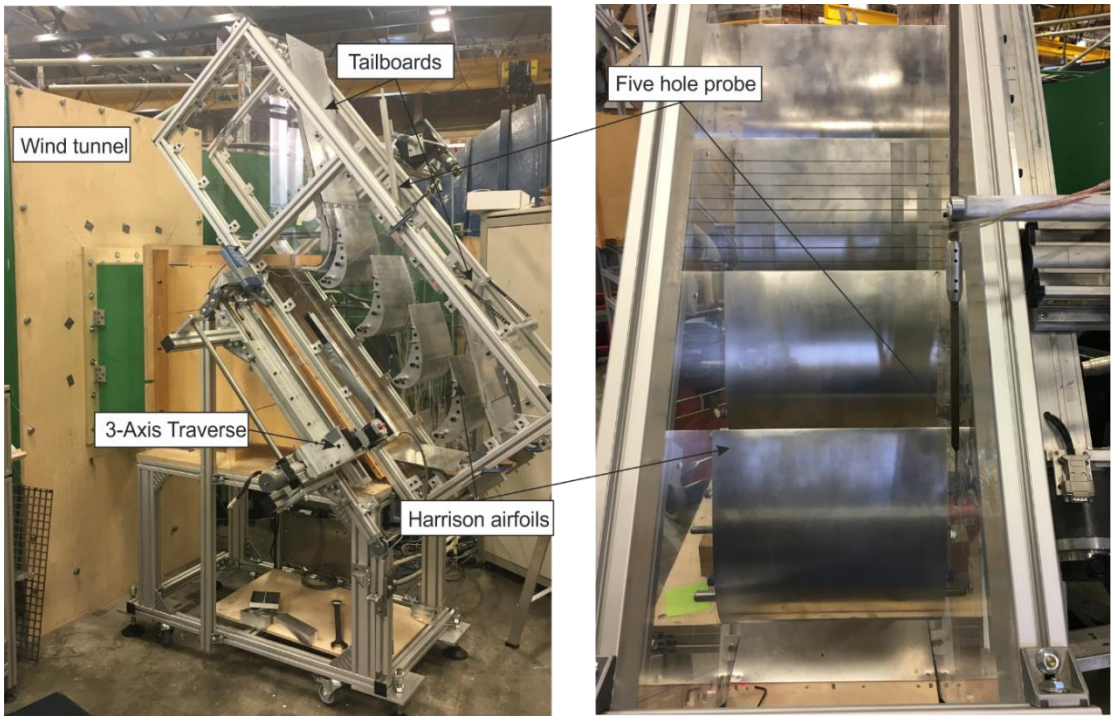

Figure 3.18: Photograph of cascade set up: side view (left), and aft looking forward (right).

Figure 3.18 shows a photograph of the experimental set up. The mass flow split through the passages was controlled by adjusting tailboards at the outer and inner tunnel walls to ensure that each blade operated in exactly the same conditions.

3.4.1 Area traverse

The large scale of this experiment allowed detailed area surveys within the passage and downstream of the vane. Access within the passage was provided via a window cut out of one of the Perspex endwalls of the cascade. A Perspex insert was manufactured to fit into this opening with an instrumentation slot that extended in the pitchwise direction from the suction surface of one blade to the pressure surface of the adjacent blade. Several inserts were made up with the instrumentation slot at a different location. The axial locations of the four final measurement planes inside the passage are indicated on the loading plot in Figure 3.21.

The five hole probe was traversed using two precision grade Parker 404XR traverse rail mounted in blade span and blade-to-blade direction. Each area traverse contained between 700 to 1,000 data points which were clustered around regions of high loss. The final traverse grid was manually refined after several iterations of coarse traverses. Figure 3.19 shows an example

of the area traverse at an axial location of x=0.87Cx. There are eight points inside the suction surface boundary layer and four inside the endwall boundary layer.

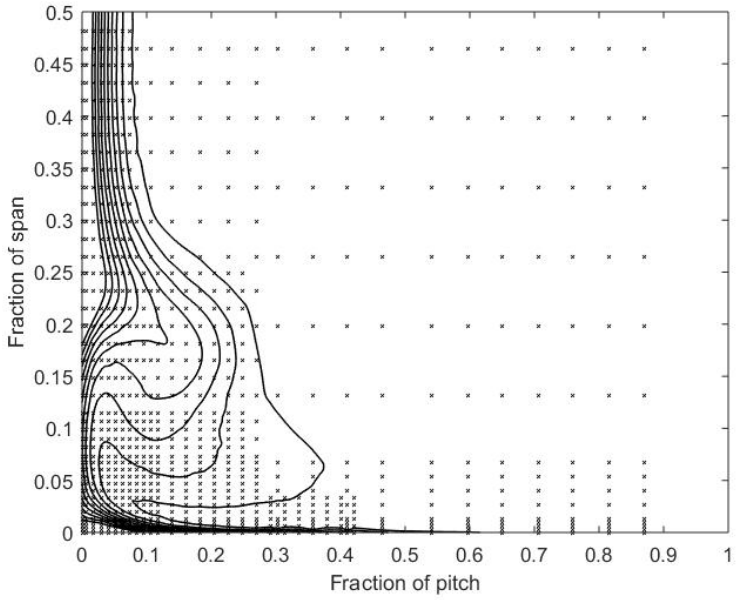

Figure 3.59: Example of traverse grid and the resulting contours of stagnation pressure loss.

3.4.2 Periodicity and loading

Measurements were performed on the inner two blades of the four blade cascade. Periodicity was checked with a midspan wake traverse. Figure 3.20 shows the wakes from two adjacent blades measured at x=1.23Cx (exit of the control volume). These wakes were measured with grid turbulence. The periodicity is excellent and the mass average loss coefficient agrees within 3%.

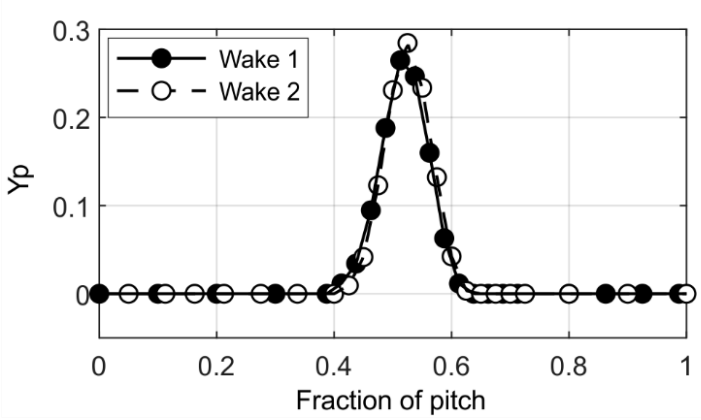

Figure 3.20: Midspan loss coefficient across two adjacent wakes at x=1.23Cx (grid Tu)

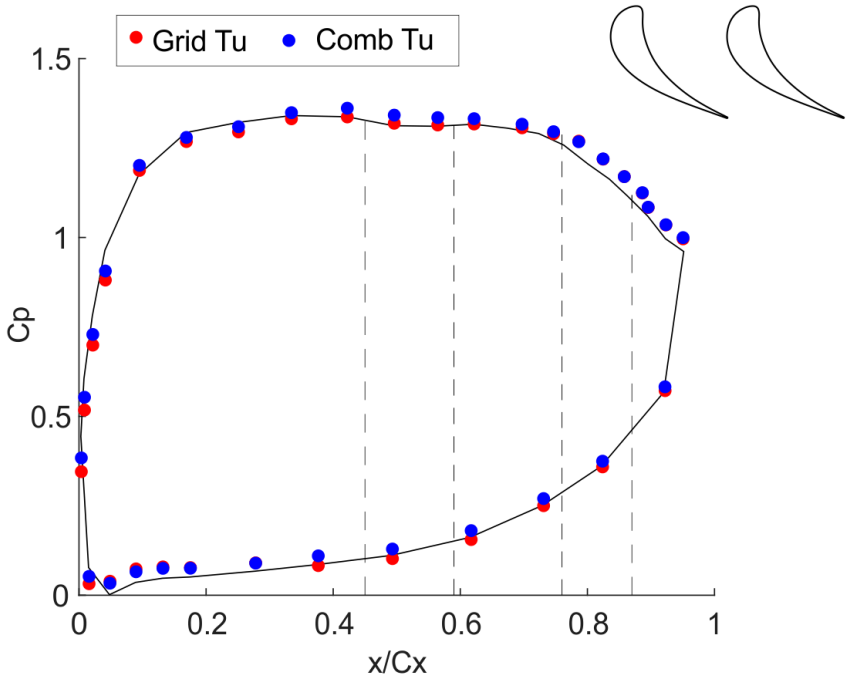

Figure 3.21: Midspan loading distribution measured in grid and combustor turbulence. Black line indicates CFD results, solid points indicate measurements.

The cascade was equipped with midspan pressure tappings on the inner two blades. The pressure distributions are shown in Figure 3.21 using the definition:

$$C_p = \frac{P_{o1} - P}{P_{o1} - P_2} \tag{3.16}$$

The loading distribution is a "flat top," with rapid acceleration around the leading edge and slight diffusion on the late suction surface. The loading distribution shown in Figure 3.21 also proves that combustor turbulence did not affect the loading. In Figure 3.21, the black line is from a RANS calculation at midspan.

3.4.3 Loss coefficient

The measurements on the cascade were designed to examine the impact of combustor turbulence on turbine loss mechanisms. The loss coefficient is calculated from the difference in the mass-averaged total pressure from the inlet to the exit of the turbine control volume. The total loss is broken down into profile loss, freestream loss, and endwall loss. To understand the physical mechanisms responsible for the profile and endwall loss, additional measurements are taken within the blade passage.

The total loss was calculated from the difference in the mass averaged total pressure from the inlet to the exit of the turbine cascade control volume shown in Figure 3.16. The loss coefficient is given by:

$$Y_p^{MA} = \frac{P_{o,inlet}^{MA} - P_{o,exit}^{MA}}{P_{o,inlet}^{MA} - P_{exit}} \tag{3.17}$$

where the mass averaged stagnation pressure was determined by:

$$P_o^{MA} = \frac{\int_A \rho U_x P_o dA}{\int_A \rho U_x dA} \tag{3.18}$$

The mixed out loss coefficient is given by

$$Y_p^{MIX} = \frac{P_{o,inlet}^{MA} - P_{o,exit}^{MIX}}{P_{o,inlet}^{MA} - P_{exit}} \tag{3.19}$$

The profile loss was calculated by measuring one pitch at the midspan with a five hole probe. The mass averaged and mixed out loss coefficients were calculated by applying Equations 3.17 and 3.19 across the pitch respectively.

The development of suction surface loss was quantified by measuring the suction surface boundary layer. Hot wire measurements were performed on the suction surface of the cascade between x=0.8Cx and just upstream of the trailing edge. To traverse the boundary layer, the hot wire was rotated away from the blade in an arc. The arc motion of the hot wire was simulated in the CAD model and recast into wall normal coordinates. The wall fitting routine discussed in Section 3.2.2 was used to determine boundary layer integral quantities. The energy thickness represents the mass averaged loss coefficient.

$$Y_p^{MA} = \frac{P_{o,inlet}^{MA} - P_o^{MA}}{P_{o,inlet}^{MA} - P_{exit}} = \frac{\delta_e}{\sigma \cos\alpha_2} C_p^{3/2} \tag{3.20}$$

The momentum thickness represents the mixed out loss coefficient.

$$Y_p^{MIX} = \frac{P_{o,inlet}^{MA} - P_o^{MIX}}{P_{o,inlet}^{MA} - P_{exit}} = \frac{2\theta}{\sigma \cos\alpha_2} C_p \tag{3.21}$$

3.4.4 Secondary flow

The strength of the secondary flow can be determined by integrating the secondary kinetic energy on each traverse plane. The secondary velocity is defined as:

$$\boldsymbol{V}_{sec} = \boldsymbol{V} \times \boldsymbol{e}_p \tag{3.22}$$

where $\boldsymbol{e}_p$ is a unit vector in the primary direction. The primary flow direction was taken to be at the midspan, where the flow is two-dimensional. The secondary kinetic energy at a given measurement location was determined relative to the flow direction at the same pitch and axial location but at the midspan radial (spanwise) location.

The secondary velocity was determined with a coordinate transformation proposed by Gregory-Smith et al. (1988). The radial component (z-direction) of the secondary velocity is unchanged. The y-direction of the secondary velocity is given by:

$$V_{sec,y} = V_x \sin(\alpha_p) + V_y \cos(\alpha_p) \tag{3.23}$$

where α_p is the primary flow angle, determined at midspan. It follows that the secondary kinetic energy is given by:

$$SKE = \frac{1}{2}\left|V_{sec,y}^2 + V_{sec,z}^2\right| \tag{3.24}$$

The secondary kinetic energy is normalised with the exit kinetic energy.

3.4.5 Uncertainty analysis

The uncertainty in the passage loss at the control volume exit was ±0.0003 of exit dynamic head in grid turbulence and ±0.001 of exit dynamic head in combustor turbulence. This error was determined by a Monte Carlo simulation based on the measured uncertainty in total and static pressure and tangential and radial flow angles. For each measured variable in the passage traverse, the average value and uncertainty were calculated based on bias and precision error to 95%, or ± two sigma. In the Monte Carlo analysis, a traverse was recreated with each local variable drawn at random from a normal distribution of that local variable. The mass average loss coefficient from 100 of such simulated traverses was found to be within ±0.00031 of the mean-value traverse.

3.5 Summary

This chapter explained the experimental methodology used in this research. The tests consisted of measurements on a cascade and a flat plate in grid and in combustor turbulence. Steady state measurements of velocity, stagnation pressure, and flow angles with a five hole probe were used to determine loss and secondary kinetic energy. Unsteady measurements with a hot wire were used to determine turbulence intensity, isotropy, and length scale. A key component of the research was resolving the boundary layer.

Chapter 4
Inlet Turbulence

4.1 Introduction

This chapter has two aims. The first is to provide guidance for generating combustor turbulence in laboratory testing. Two questions regarding the combustor simulator design are answered.

1. How to design a combustor simulator to achieve uniform flow and high turbulence?
2. To what extent can RANS CFD be used to predict the performance of a combustor simulator?

The second aim of this chapter is to characterise the two inlet conditions created by the turbulence grid and the combustor simulator.

4.2 Design of a high turbulence generator

This research is concerned with understanding the impact of realistic turbulence in a gas turbine. It is therefore important that the incoming turbulence is simulated correctly.

4.2.1 Selection of the type of turbulence generation

Jets in crossflow was chosen as the means of generating the turbulence, because this is the main mechanism that generates turbulence in a real combustor (see Chapter 2.1). The biggest difference between a combustor simulator based on jets in crossflow and a real combustor is heat release. The measurements of Zimmerman (1979), Bicen, Tse, and Whitelaw (1988), and

Moss and Oldefield (1991) showed that turbulence is not affected by the combustion process itself. Thus, combustor turbulence can be well replicated with isothermal jets in crossflow.

The length scale of turbulence generated with jets in crossflow is known to scale with the jet diameter (e.g. Thole and Bogard, 1996, and Cresci et al., 2015). Therefore, if the geometric scales in the combustor relative to the turbine are chosen to be representative of a real gas turbine engine, then the scale of turbulence in the test will also be representative of a real gas turbine engine. In addition, the interaction of the jets in crossflow may create structures in the turbulence which are not yet understood and can therefore be neglected in a different set up. Ames (1990) observed that a non-zero Reynolds stress formed in the combustor simulator affected the growth of a turbulent boundary layer downstream.

A combustor simulator based on jets in crossflow is still different from a real combustor. In a real combustor, a myriad of flow features, including swirl, liner film cooling, and turbine endwall cooling, will affect loss in the downstream turbine. The aim in this investigation is to decouple the flow pattern of a real combustor and its turbulence field. This study aims to isolate the effect of jet generated combustor turbulence alone.

4.2.2 Design of the combustor simulator

Figure 4.1 shows the general design of the combustor simulator. Slow moving air from the plenum enters the combustor through one of the three porous panels, mixes inside the combustor and proceeds through a contraction to the test section. One third of the flow enters the liner through the first row of opposing ports (primary cooling jets), and one third of the flow enters through the second row (dilution jets). The rest of the flow enters through slots which simulate wall jets.

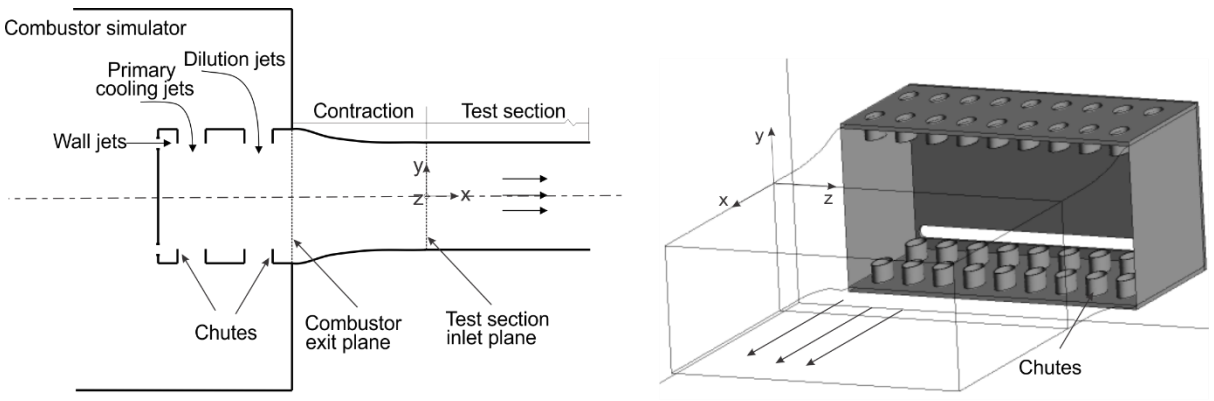

Figure 4.1: Schematic and CAD model of a combustor simulator.

The ports for the primary and dilution jets had an oval shape and were plunged with thin-walled chutes. An oval shape was selected over a circular one based on the findings of Kingery and Ames that thin-walled elliptical tubes produce less flow blockage than circular plunged holes. Chutes are typically fitted in modern gas turbine combustors (e.g. Rolls-Royce RB211 and Trent) to improve jet penetration (Lefebvre, 1999, pg. 111). The ports in the combustor simulator therefore also have chutes which protrude a distance of 40 mm into the liner to increase the jet penetration.

The sizing of the ports is important. It was shown in Chapter 2 that in turbulence generated by jets in crossflow, the integral length scale is on the order of the jet port diameter. To generate engine representative turbulence, the geometric scaling of combustor ports to turbine chord should be consistent with engine hardware. In this turbulence generator, the ports have a hydraulic diameter, D_{port}, of 48 mm. The ratio of jet port diameter and the turbine axial chord is 0.21. This ratio is not readily available from gas turbine manufacturers because combustor geometry is highly proprietary; however, there are a few open literature combustor-turbine facilities which are based on real engines that do report this ratio. One such rig is the Oxford combustor turbine interaction (CTI) rig which was based on Rolls-Royce designs. The ratio of jet diameter to axial chord on the Oxford rig is between 0.16, for the smallest jets, and 0.30, for the largest jets (Cresci et al., 2015). In a separate engine-representative CTI rig at Virginia Polytechnic Institute, based on Pratt & Whitney designs, the ratio of jet diameter to axial chord was between 0.28, for the smallest jets, and 0.41, for the largest jets (Barringer et al., 2002). The jet scaling of the combustor simulator in this thesis is therefore consistent with previous work and representative of real engines.

Steady RANS CFD simulations of the combustor simulator were performed during the design process to predict the general flow pattern. The unstructured computational mesh, Figure 4.2, was generated with ANSYS ICEM and typically contained 10 million cells. The mesh was coarse in the plenum (average cell size of $0.27D_{port}$) but refined inside of the combustor simulator (average cell size of $0.07D_{port}$). Eight prism layers were used to resolve the boundary layer on all viscous surfaces. There were approximately 28 cells across each port (x-direction), 20 across each wall jet slot (y-direction), and 169 across the height of the liner (y-direction). Calculations were performed using ANSYS Fluent with a realizable k-ε model at a Reynolds number based on exit velocity and port diameter of 128,644.

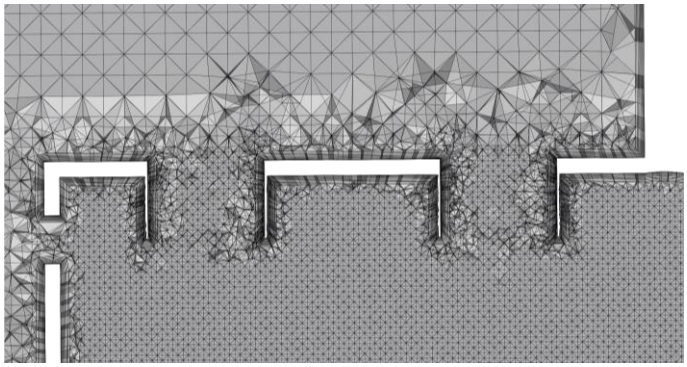

Figure 4.2: Detail of the computational mesh used with RANS CFD (close up view on x-y plane with one slot and two ports).

The key challenge when designing a combustor turbulence generator is to achieve high levels of turbulence while creating a uniform mean flow. This is important because if the total pressure at test section inlet is non-uniform, then the secondary flow will be changed in the downstream cascade. It is important not to change these endwall flows because this study aims to isolate the effect of combustor turbulence alone.

Flow uniformity

Two designs were studied with RANS CFD. These are shown in Figure 4.3. Design A, the initial design, was designed according to Kingery and Ames (2016). Design B is an improved design that achieved better flow uniformity.

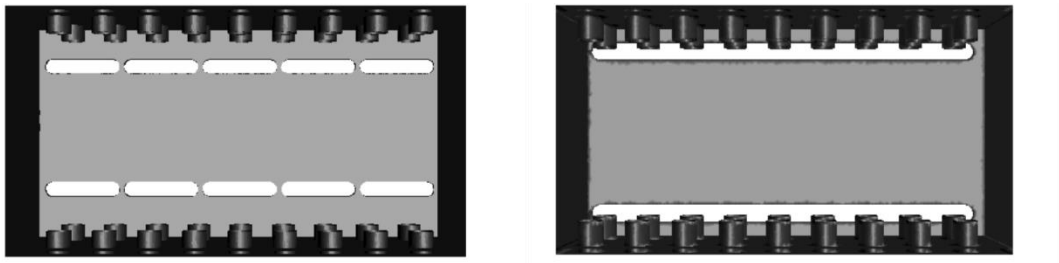

Figure 4.3: CAD models of combustor simulators: Design A (left) and Design B (right). View is aft looking forward.

The radial profiles of stagnation pressure coefficient at combustor exit are shown for both designs in Figure 4.4. These radial profiles have been circumferentially mass-averaged across the entire combustor (which spans four cascade pitches). Figure 4.4 shows that the midspan peak and endwall deficit in Design A have been reduced in Design B by 57% (calculated from the standard deviation of the profiles).

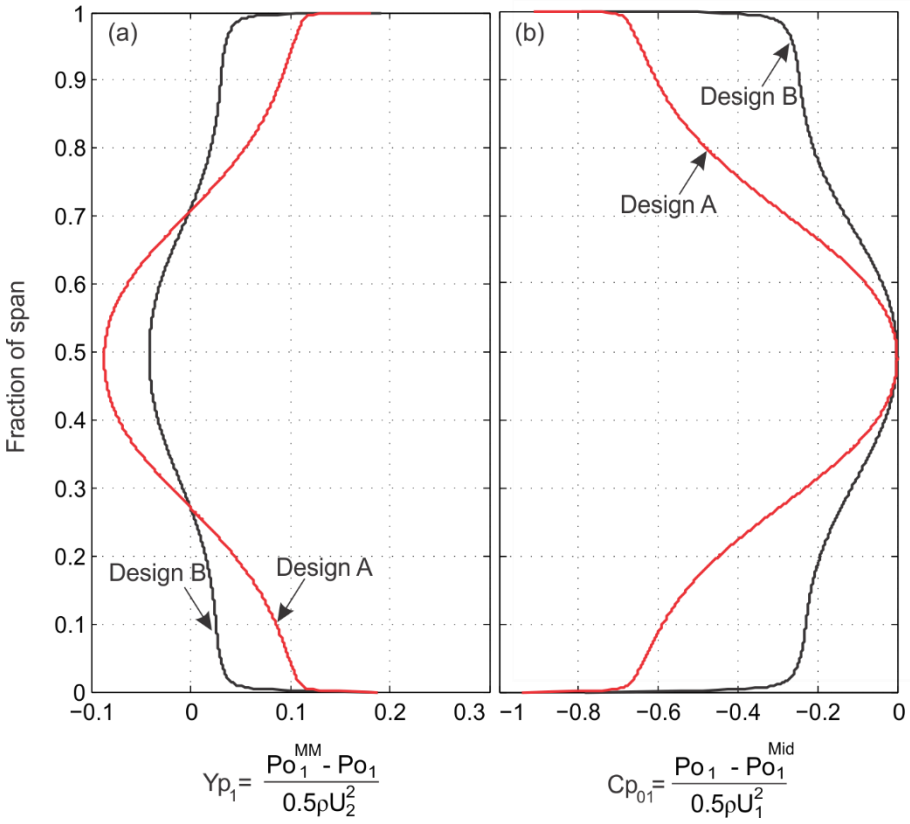

Figure 4.4: Radial profile of stagnation pressure calculated from CFD for two designs of combustor simulator.

The left hand side of Figure 4.4 shows stagnation pressure inlet relative to the overall mass-averaged inlet stagnation pressure and normalised by the turbine exit dynamic head. The mixed out loss coefficient of Design B is 0.32%, which is approximately one third of the mixed out loss coefficient of Design A (1.01%). Relative to the turbine loss coefficient (nominal Y_p=4.8%, Harrison, 1987), the mixed out loss of Design A is 21%. This would cause significant difficulties in decoupling the effect of turbulence on loss mechanisms. By contrast, the mixed out loss coefficient of Design B is only 7% of the nominal turbine loss coefficient.

The right hand side of Figure 4.4 plots a normalised stagnation pressure coefficient, Cp_{01}, defined as the midpsan stagnation pressure subtracted from the local stagnation pressure and normalised by the turbine inlet dynamic head. Note that by this definition, Cp_{01} is equal to zero at midspan. This parameter has been calculated to compare the combustor simulator profile to other simulators and to real engines. Real engines exhibit endwall Cp_{01} values in the range of -0.5 to 2.0. A large positive value of Cp_{01} results from a high level of liner film cooling. Without film cooling, the endwall Cp_{01} measured on an engine representative rig at the Air

Force, was in the range of -0.7 and -0.2 (Barringer, Thole, and Polanka, 2007). The present combustor simulator had a similar endwall deficit. Just outside of the boundary layer, Cp_{01} is -0.25 for Design A is and -0.67 for Design B.

Turbulence intensity

Combustor turbulence generated by jets in crossflow depends on the trajectory of the jet. There are two key regions of turbulence generation. These are illustrated with CFD results of Design B in Figure 4.5. The first region is the primary cooling jet impingement, where the jets penetrate into the middle of the liner and interact. The second region is the shear as the dilution cooling jet, which has a shallower penetration, is deflected by the bulk streamwise flow.

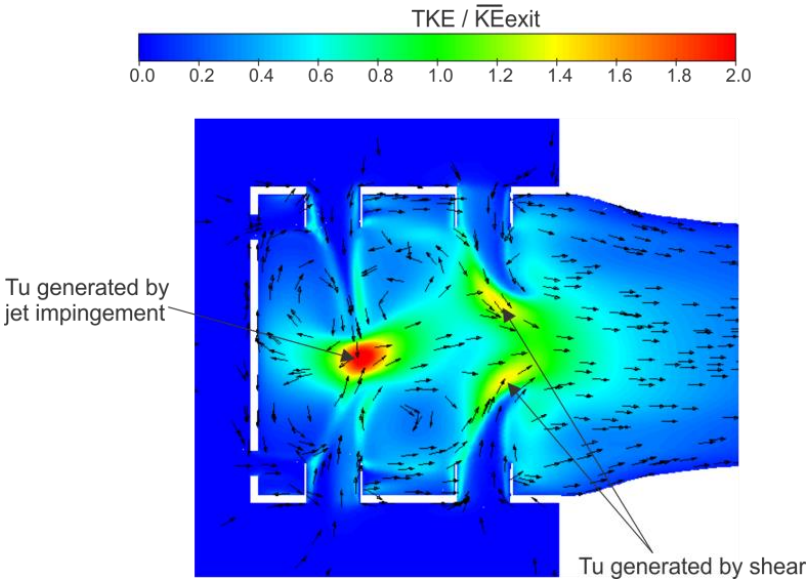

Figure 4.5: Contours of normalised turbulent kinetic energy calculated with RANS CFD.

Jet impingement is known to be a dominant source of turbulent kinetic energy production (Koutmos and McGuirk, 1989). In Figure 4.5, the turbulent kinetic energy in the impingement region is twice as large as the exit mean kinetic energy of the flow. As jets collide in the centre of the combustor, the cooling air is split into four re-circulation regions. These are identified with in-plane vectors in Fig. 4.5. In addition, the blockage effect caused by jets merging redirects the remaining fluid in the lateral direction (out of the page in Figure 4.5). Similar findings were reported by Cha et al. who used experiments and computational simulations of real engine hardware to show that the high levels of turbulence in a combustor are created by the unstable, opposed cooling jets (e.g. Cha et al., 2012b).

The area with the second highest amount of turbulent kinetic energy is where a second set of jets are strongly deformed by the streamwise bulk flow. The dilution jets have a weaker impingement but a strong interaction between the jets and the crossflow. Shear is known to be the dominant mechanism of turbulence generation when impingement is not present (Koutmos and McGuirk, 1989). In Figure 4.5, the turbulent kinetic energy at the interface of the dilution jets and the bulk flow is on the same order as the exit mean kinetic energy.

In summary, the combustor simulator aerodynamics were designed to produce a uniform flow field at the turbine inlet with high levels of freestream turbulence.

4.3 Build and test of the combustor simulator

Design B was manufactured and installed in an open loop, low speed wind tunnel. The details of the geometry are given in Figure 4.6. Steady and unsteady measurements were taken with a five hole probe and hot wire at approximately $9.3D_{port}$ downstream of the combustor exit. The focus of the combustor simulator characterisation was (1) uniformity of the steady field, (2) turbulence intensity and its development, and (3) details of turbulence structure.

The measured and RANS predicted flow field in the measurement plane are shown in Figure 4.7. The computational data has been clipped to cover the same area as the experimental traverse. It covers six port pitches in the circumferential (z-axis) direction and 93% of span y-axis). Figure 4.7 top left shows that good uniformity (standard deviation in plane of 4.9%) has been achieved. The measured velocity profile shows no trace of the upstream jets. Any steady structures have been mixed out by turbulent mixing. The RANS CFD predictions, shown in Figure 4.7 bottom left, show a higher degree of non-uniformity (standard deviation in plane of 6.9%). It is likely that standard RANS CFD under-predicts the turbulent mixing and hence retains some of the structures from the upstream flow.

The measured and RANS predicted radial distributions of stagnation pressure, circumferentially mass-averaged across the entire combustor exit, are shown in Figure 4.8 (this should be compared with Figure 4.4). Figure 4.8 shows that the measured inlet profile is flatter, with a lower midspan peak and less endwall stagnation pressure deficit, than had been predicted with RANS.

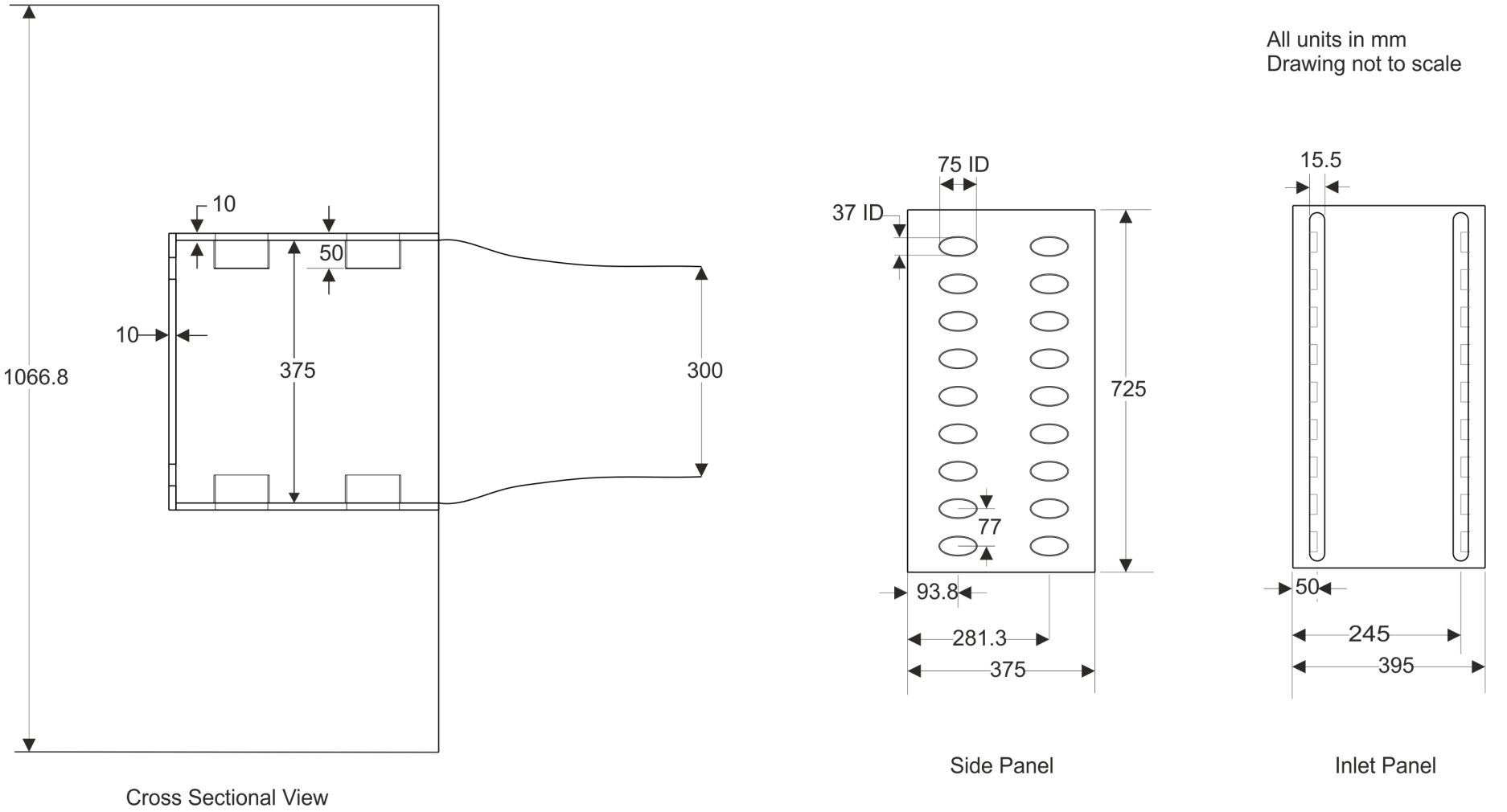

Figure 4.6: Geometry of combustor design

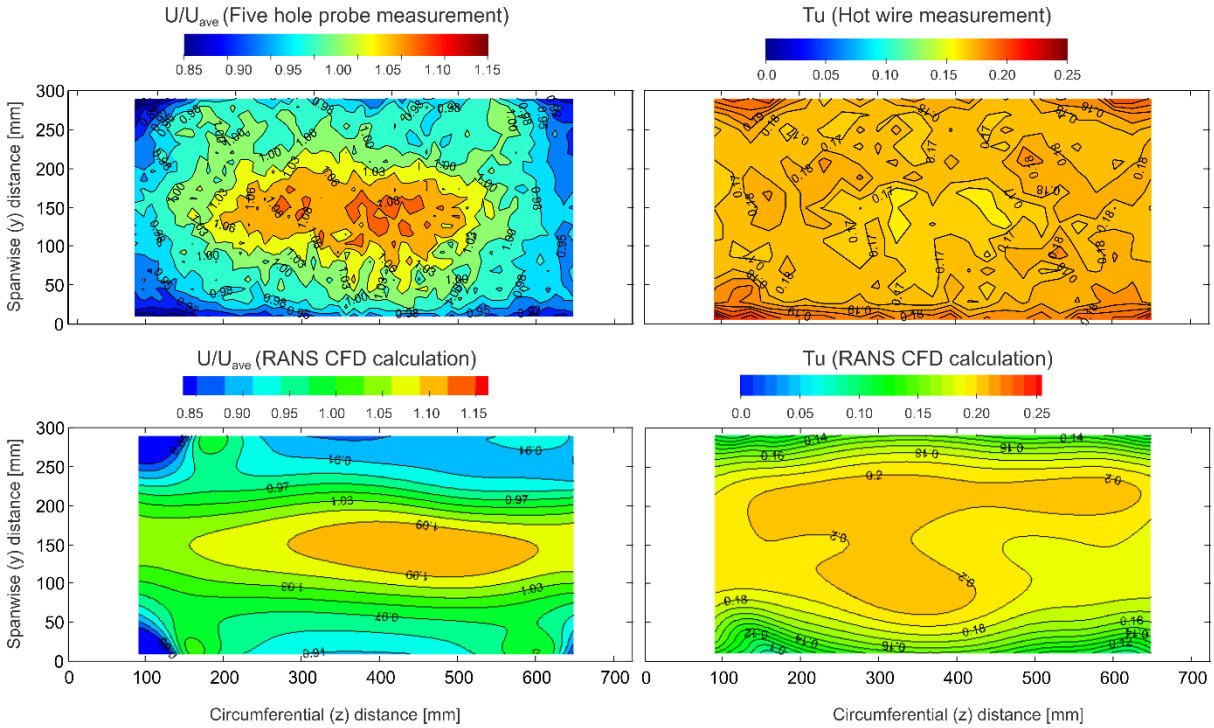

Figure 4.7: Measurement (top) and CFD (bottom) of mean velocity and turbulence intensity.

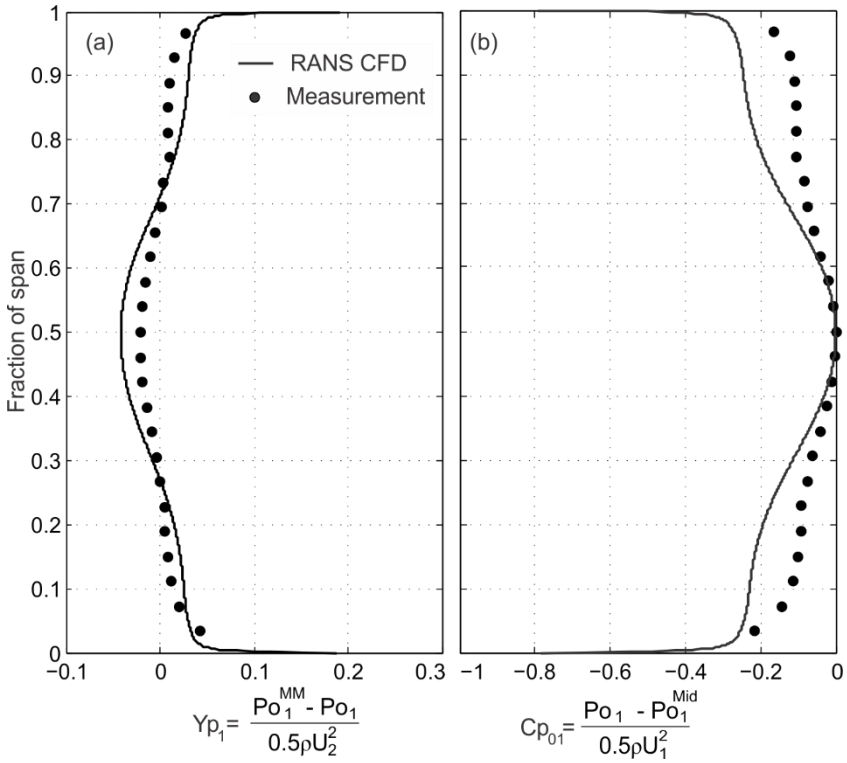

Figure 4.8: Radial profile of stagnation pressure, calculated and measured values.

Figure 4.7 top right shows that the measured turbulence intensity at the combustor exit is high (17.5% intensity on average) and relatively uniform. The standard deviation in the plane is 0.8% turbulence intensity, which is 4.5% relative to the average. Again, there is no evidence of the upstream jet structures in the measured turbulence field. The RANS CFD turbulence intensity was calculated with Equation 4.1. Figure 4.7 bottom right, shows that RANS turbulence is higher (19.1% intensity on average) and less uniform (standard deviation is 2.6% turbulence intensity, or 13.6% relative to the average) than the measured turbulence. The over prediction of turbulence intensity by RANS CFD has also been found by Cha et al. (2012a) and Cresci et al. (2015).

$$Tu = \frac{\sqrt{\frac{2}{3}k}}{\bar{U}} \tag{4.1}$$

The measured integral length scale, calculated from the autocorrelation of the instantaneous streamwise velocity, was found to be on average 40.6 mm ($0.85D_{ports}$) with a standard deviation of 21%. These results are consistent with previous research which shows that, in a jets in crossflow case, the integral length scale of turbulence is of the order of the size of the feature which generated it (e.g. Thole and Bogard, 1996, Cresci et al., 2015). The RANS CFD integral length scale, calculated from the k-ε model turbulence model with Equation 4.2, was twice as large. On average, in the same plane, the CFD integral length scale was 85 mm ($1.77D_{ports}$).

$$\Lambda_{\text{int}} = \frac{k^{\frac{3}{2}}}{\varepsilon} \tag{4.2}$$

The axial decay of the combustor turbulence is shown in shown in Figure 4.9, along with predictions from CFD. The axial location is taken from the exit plane of the combustor and is normalized by D_{ports}. The turbulence intensity predicted with RANS CFD is 20% higher (relatively) than the measured turbulence downstream of the combustor simulator. The turbulence develops inversely with axial distance as $Tu \sim \left(\frac{x}{D_{port}}\right)^{-0.644}$. The power law behavior fits the RANS CFD data only downstream of approximately $9D_{port}$ of the combustor exit. The same exponent matches the measured development of freestream turbulence.

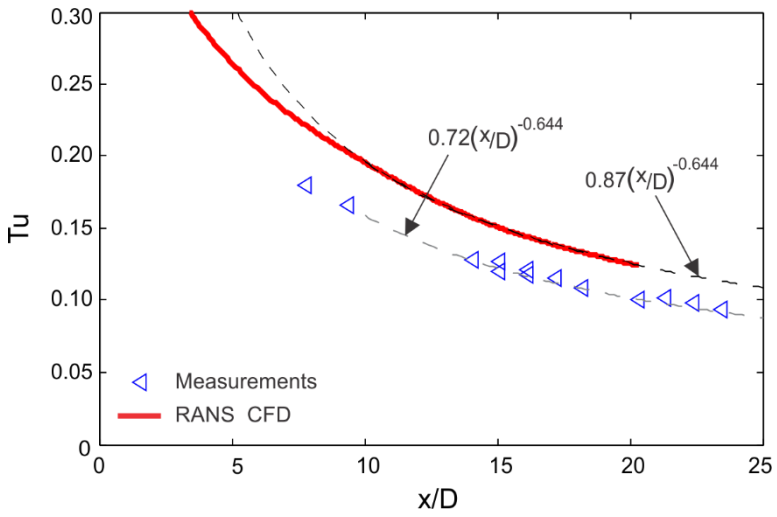

Figure 4.9: Measurement and CFD predictions of turbulence development.

An analogy could be drawn to grid turbulence which develops as $Tu \sim \left(\frac{x}{d}\right)^{-0.7}$ at a distance of at least ten mesh lengths downstream of the grid (beyond which it is considered homogeneous, after Roach, 1987). From this analogy we may suppose that combustor turbulence decays slightly slower than grid turbulence. This is consistent with measurements in combustor turbulence (Thole et al., 1994). However, the power fit is sensitive to the choice of origin and the current study does not provide sufficient data to determine where combustor turbulence may be considered homogeneous. Care should be taken to determine the starting point of homogeneous turbulence if an accurate decay rate is required (e.g. for testing at different inlet turbulence levels by changing the axial spacing between test section inlet and combustor exit).

In summary, the manufactured combustor simulator was found to produce high turbulence (17.5%) and good exit uniformity (within 7% of average velocity). RANS CFD was found to be adequate in predicting flow pattern and turbulence development but not the turbulence length scale. It was also noted that the CFD under predicted the turbulent mixing out of the flow.

4.4 Design of turbulence grid

The second inlet tested conventional grid turbulence. The key challenge was to design a grid which generated turbulence with a lower intensity level but the same length scale as the combustor turbulence.

The traditional correlation after Roach (1989) was used to determine the grid geometry. Turbulence and integral length scale were calculated with Equations 2.1 and 4.3, respectively.

$$\frac{\Lambda}{d} = C_2 \left(\frac{x}{d}\right)^{1/2} \tag{4.3}$$

Equations 2.1 and 4.3 are plotted in Figure 4.8. The uncertainty range represents the scatter of the coefficients C_1 and C_2 reported in literature (Roach, 1989, and Van Fossen et al.,1994).

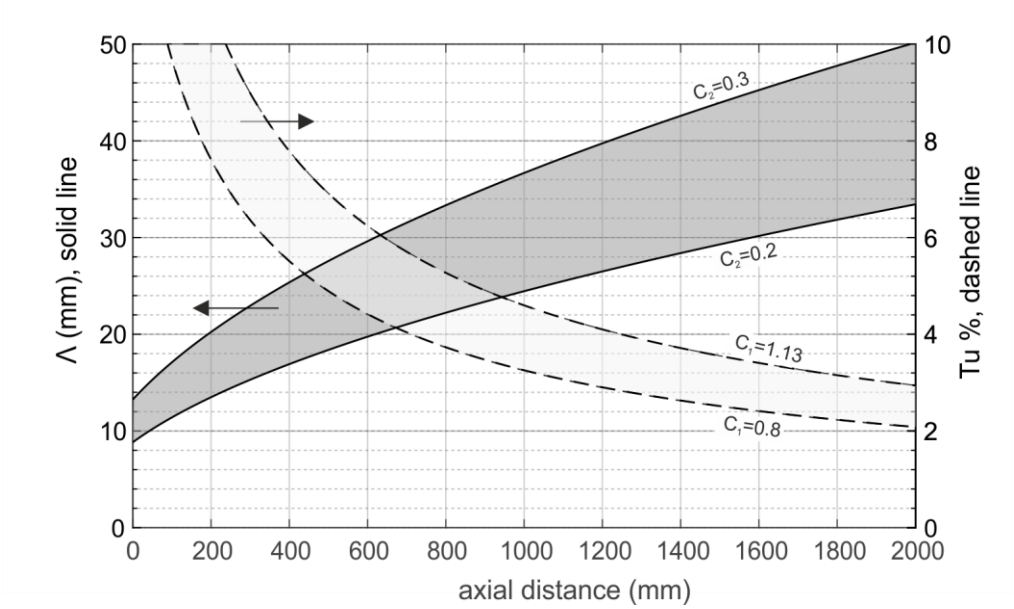

Figure 4.10: Correlations for grid turbulence intensity and length scale after Roach, 1989, and Van Fossen et al.,1994

The integral length scale of turbulence increases downstream of the grid because smaller eddies dissipate faster than larger ones. An empty duct of constant cross sectional area and 1.3 metre length was therefore installed between the grid and the test section to develop larger length scales to better match the combustor simulator.

The measured turbulence intensity at the inlet of the test section was 2.3%, which was slightly lower than the predicted intensity (2.7%-3.8%). The measured integral length scale was approximately 40 mm, in line with the range of predicted integral length scale (27.5mm-41.3mm).

In summary, the correlations for grid turbulence were found to be accurate when designing a turbulence grid with large integral length scales. The manufactured grid was found to produce low turbulence (2.3%) and similar length scale to the combustor simulator (40 mm).

4.5 Nature of inlet turbulence

Combustor turbulence is quite clearly different in nature from grid turbulence. As previously discussed, turbulence is generated when opposing jets in crossflow collide in the middle of the combustor. Such jet interaction may cause turbulent structures of different sizes to form than in grid turbulence. It is therefore important to quantify the structure and scale of combustor turbulence. To identify structures, the isotropy of turbulence is measured. To identify scales, the most energetic length scale is identified. The scale is found to be very large relative to the downstream boundary layer. This raises the question whether such large scale turbulence is truly turbulence or rather a periodic unsteadiness. That is, is the response of the downstream boundary layer quasi-steady or unsteady?

4.5.1 Anisotropy of turbulence

The level of anisotropy was determined by measuring simultaneously the streamwise and the lateral components of turbulence with a cross wire. Figure 4.11 shows the components of turbulence measured at the inlet plane of the turbine control volume. The x-axis zero is the center of the test section where the flat plate was located.

The top two subplots in Figure 4.11 show the ratio of spanwise and pitchwise fluctuations, $\overline{vv}$ and $\overline{ww}$, to streamwise fluctuations, $\overline{uu}$. The ratio in each plot is close to one in both grid and combustor turbulence. This indicates that by the exit of the combustor, the turbulence is remarkably isotropic in nature.

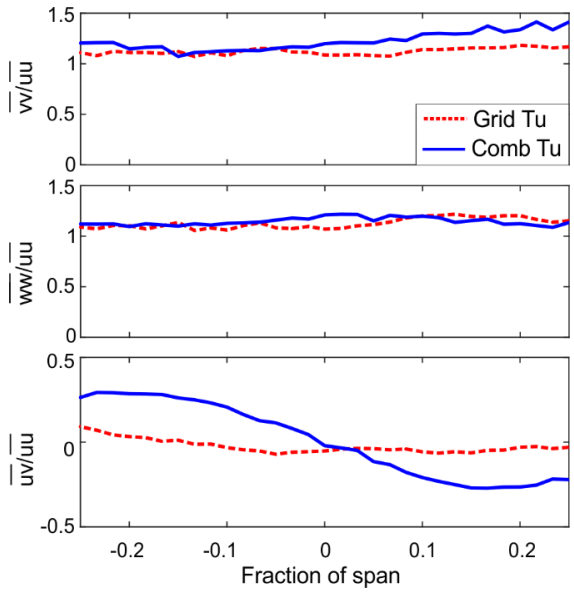

Figure 4.11: Measurements of lateral velocity fluctuations at combustor exit.

The bottom subplot in Figure 4.11 shows the variation in Reynolds stress, $\overline{uv}$. The grid turbulence has a near zero value. The combustor turbulence Reynolds stress is not zero, and it exhibits an antisymmetric shape. This is caused by the opposing direction of the impinging jets in the combustor simulator. The magnitude of this term is small, but it indicates that small coherent structures are still present in the combustor turbulence.

4.5.2 Is boundary layer response quasi-steady?

The integral length scale of combustor turbulence (22% of turbine chord) is larger than typical laboratory grid turbulence (~2% of turbine chord). This means that the characteristic time scale, imposed by the combustor turbulence on the boundary layer, is 10 times larger than typical laboratory grid turbulence. This raises the question of whether the boundary layer response to this larger time scale is in fact 'quasi-steady'.

The non-dimensional frequency of importance is the reduced frequency given in Equation 4.4. It is the ratio of the time taken for momentum or vorticity to diffuse through the boundary layer, order δ^2/ν, to the time taken for the flow in the freestream to change, order $1/\omega$. Typically, if $\omega_r < 0.1$, a 'quasi-steady' approximation of the boundary layer is considered acceptable.

$$\omega_r = \delta^2\omega/\nu. \tag{4.4}$$

Figure 4.12 shows energy spectra of the grid and combustor turbulence. The turbulence measurements were taken in the freestream above a boundary layer developing on a flat plate. The uncertainty bands represent the range of turbulent viscosity in a boundary layer. The peak in the spectrum is observed to occur at $\delta^2\omega/\nu \sim 10$. This shows that the diffusion time scale is 10 times the characteristic time scale associated with the large turbulent eddies in the freestream. Figure 4.12 also shows that the two methods of turbulence generation in this investigation achieve the same level of turbulence length scales.

In conclusion, the response of the boundary layer to combustor turbulence is far from 'quasi-steady'. In a review paper on unsteady boundary layers, Telionis (1979) laments that even the most advanced models "do not seem to predict even the physical tendencies correctly." In this research, the response of the boundary layer to combustor turbulence is measured experimentally.

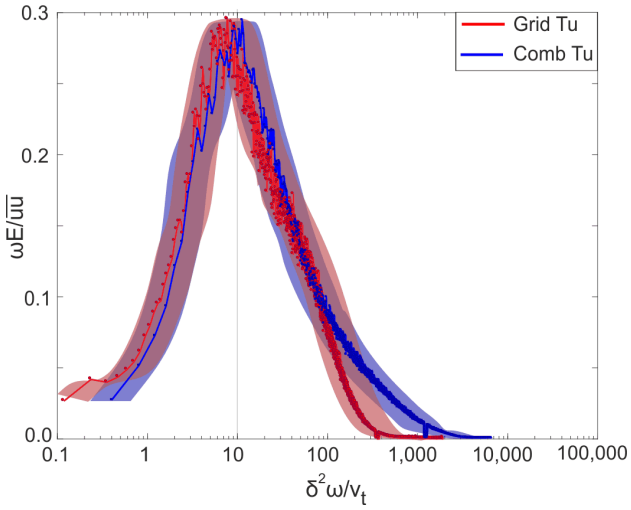

Figure 4.12: Energy spectra of turbulent kinetic energy measured in combustor and large-scale grid turbulence.

4.6 Summary

Two turbulence generators have been created to study the difference between combustor and grid turbulence. The first was a turbulence grid which produced low turbulence intensity and the second a combustor simulator which produced high turbulence intensity. The two turbulence generators were designed to produce the same length scale of turbulence.

The aim was to produce a combustor turbulence generator which achieved high levels of turbulence but a flowfield which was uniform. The final design produced 17.5% turbulence intensity at the exit plane and was uniform to within 7%. This turbulence intensity is representative of real gas turbine combustor turbulence (9-20%, see Chapter 2). The nature of combustor turbulence was studied. It was found that by the turbine inlet plane, combustor turbulence is relatively isotropic. A non-zero Reynolds stress, caused by the jet orientation, was measured in the combustor turbulence.

Chapter 5
Loss Accounting

The aim of this chapter is to present two methods of loss accounting and to demonstrate that one is preferable in cases where the freestream turbulence is high. The first method defines loss as having occurred when mechanical energy is dissipated in the flow and converted into internal energy. The second method defines loss as having occurred when mechanical energy has left the mean field. This can occur either through dissipation of the kinetic energy of the mean field or by the conversion of the kinetic energy in the mean field into turbulent kinetic energy.

This chapter will first introduce the two methods of loss accounting and discuss the underlying physical mechanisms. Results from direct numeric simulation (DNS) of a flat plate from Schlatter and Örlu (2010) are used to illustrate the magnitude and distribution of loss in a turbulent boundary layer using both methods. It will be shown that in the presence of freestream turbulence, the second method of loss accounting is the most useful for a turbine designer. The loss analysis is extended for a control volume and finally the mechanisms responsible for loss generation in the freestream are examined.

5.1 Method 1 – loss as dissipation of kinetic energy

The first method defines loss as having occurred when viscous dissipation of mechanical energy occurs on any scale. This process can be demonstrated using the kinetic energy balance (Hinze, 1975, pg. 71), shown in Equation 5.1.

$$\frac{D}{Dt}\left(\frac{U_i U_i}{2}\right) = -\frac{1}{\rho} U_j \frac{\partial P}{\partial x_j} + \nu \frac{\partial}{\partial x_j} U_i \left(\frac{\partial U_i}{\partial x_j} - \frac{\partial U_j}{\partial x_i}\right) - \nu \left(\frac{\partial U_i}{\partial x_j} - \frac{\partial U_j}{\partial x_i}\right) \frac{\partial U_i}{\partial x_j} \tag{5.1}$$

The first term on the right hand side of Equation 5.1 is the work done per unit mass and time by pressure. The sum of the kinetic energy term on the left hand side and the pressure work term on the right hand side represent the mechanical energy in a fluid available to a turbine.

The second term on the right hand side of Equation 5.1 represents the rate at which viscous stresses do work on the boundary. The third term on the right hand side of Equation 5.1 represents the dissipation of kinetic energy, per unit volume, into internal energy. This is analogous to removing the kinetic energy from the flow and replacing it with a local heat addition. The viscous dissipation term is conventionally denoted as Φ and referred to as the dissipation function.

$$\Phi = \mu \left(\frac{\partial U_i}{\partial x_j} - \frac{\partial U_j}{\partial x_i}\right) \frac{\partial U_i}{\partial x_j} \tag{5.2}$$

In adiabatic flow with uniform temperature, the rate of change of entropy per unit mass is given by Equation 5.3 (Greitzer, Tan, and Graf, 2004, pg. 27).

$$T \frac{Ds}{Dt} = \frac{1}{\rho} \Phi \tag{5.3}$$

For incompressible, adiabatic flow, Equations 5.2 and 5.3 show that entropy generation rate can be used as a measure of dissipation in the flow. A rise in entropy implies a drop in the mechanical energy of the flow and thus a reduction in the flow's ability to do work.

Viscous dissipation is always positive, raising the internal energy (higher temperature) of the fluid at the expense of mechanical energy. Denton (1993) draws an analogy between entropy (and in this case dissipation) and 'smoke,' which once created cannot be destroyed and is convected downstream through the machine.

This section first considers the physical mechanisms for entropy generation in a turbulent flow. The entropy generation in a boundary layer with and without freestream turbulence is

then calculated to illustrate why this method is not appropriate for bookkeeping loss in high freestream turbulence.

5.1.1 Mechanisms for dissipation in a turbulent flow

We now want to divide the dissipation in Equation 5.2 into two terms (Appendix A). This allows us to see that dissipation has two sources: the destruction of mean field kinetic energy and the destruction of turbulent kinetic energy.

For a turbulent flow the kinetic energy balance is:

$$\frac{D}{Dt}\left(\frac{\overline{U}_i\overline{U}_i}{2}\right)+\frac{D}{Dt}\left(\frac{\overline{u_iu_i}}{2}\right)=$$

$$-\frac{1}{\rho}\overline{U_j}\frac{\partial\bar{P}}{\partial x_j}-\frac{\partial}{\partial x_i}\overline{u_i\left(\frac{p}{\rho}+\frac{q^2}{2}\right)}$$

$$+\nu\frac{\partial}{\partial x_i}\overline{U_i}\left(\frac{\partial\overline{U_i}}{\partial x_j}+\frac{\partial\overline{U_j}}{\partial x_i}\right)-\nu\overline{\frac{\partial}{\partial x_i}u_i\left(\frac{\partial u_i}{\partial x_j}+\frac{\partial u_j}{\partial x_i}\right)}-\frac{\partial}{\partial x_i}\overline{U_i}\overline{u_i\,u_j} \tag{5.4}$$

$$-\frac{1}{\rho}\bar{\Phi}-\varepsilon$$

The first and second term on the right hand side of Equation 5.4 represent the work done per unit mass and time by pressure of mean and turbulent flow. The third, fourth, and fifth terms on the right hand side of Equation 5.4 represent the rate at which viscous and turbulent stresses do work on the boundary.

The sixth term on the right hand side is the viscous dissipation of mean kinetic energy, per unit mass and time. It represents the kinetic energy in the mean field which is dissipated and becomes internal energy.

$$\bar{\Phi}=\mu\frac{\partial\overline{U}_j}{\partial x_i}\left(\frac{\partial\overline{U}_i}{\partial x_j}+\frac{\partial\overline{U}_j}{\partial x_i}\right) \tag{5.5}$$

The seventh term is the viscous dissipation of turbulent kinetic energy, per unit mass and time. It represents the turbulent kinetic energy which is dissipated and becomes internal energy.

$$\varepsilon = \nu \overline{\left(\frac{\partial u_i}{\partial x_j} + \frac{\partial u_j}{\partial x_i}\right)\frac{\partial u_j}{\partial x_i}} \tag{5.6}$$

For a turbulent flow, the time-averaged rate of change of specific entropy is given by Equation 5.7 (Appendix A).

$$T\frac{Ds}{Dt} = \frac{1}{\rho}\bar{\Phi} + \varepsilon \tag{5.7}$$

For incompressible, adiabatic flow, Equation 5.7 shows that entropy generation rate can be used as a measure of dissipation in a turbulent flow. A rise in entropy is caused by a drop in kinetic energy, either from the mean field, the turbulent field, or both.

In summary, Method 1 defines loss as the dissipation of kinetic energy. In the absence of heat transfer and temperature gradients, entropy generation rate can be used as a measure of dissipation in the flow. In a turbulent flow, this dissipation has two sources: the destruction of mean kinetic energy, $\bar{\Phi}$, and dissipation of turbulent kinetic energy, ε. The magnitude and behaviour of these two terms in a turbulent boundary layer is discussed in the next section.

5.1.2 Entropy generation in boundary layers

The entropy generated in a zero pressure gradient boundary layer of thickness δ is determined from a DNS simulation. The turbulent boundary layer is at a Reynolds number of Re_θ=1,000, is isothermal, and has low freestream turbulence (Tu=0.1% at $y = 2\delta$). The DNS calculation of the flat plate was performed by Schlatter and Örlu (2010).

Locally, within the boundary layer, the loss generation is given by Equation 5.7. The entropy generation rate per unit volume, $\dot{S}_{vol} = \rho(Ds/Dt)$, is plotted from the DNS calculation in Figure 5.2 against the non-dimensional distance from the wall. The entropy generation rate has been non-dimensionalised on inner units:

$$\dot{S}_{vol}^{+} = \frac{\rho\nu}{u_\tau^4} T\dot{S}_v \tag{5.8}$$

$$\bar{\Phi}^{+} = \frac{\nu}{u_\tau^4}\bar{\Phi} \tag{5.9}$$

$$\varepsilon^{+} = \frac{\nu\rho\varepsilon}{u_\tau^4} \tag{5.10}$$

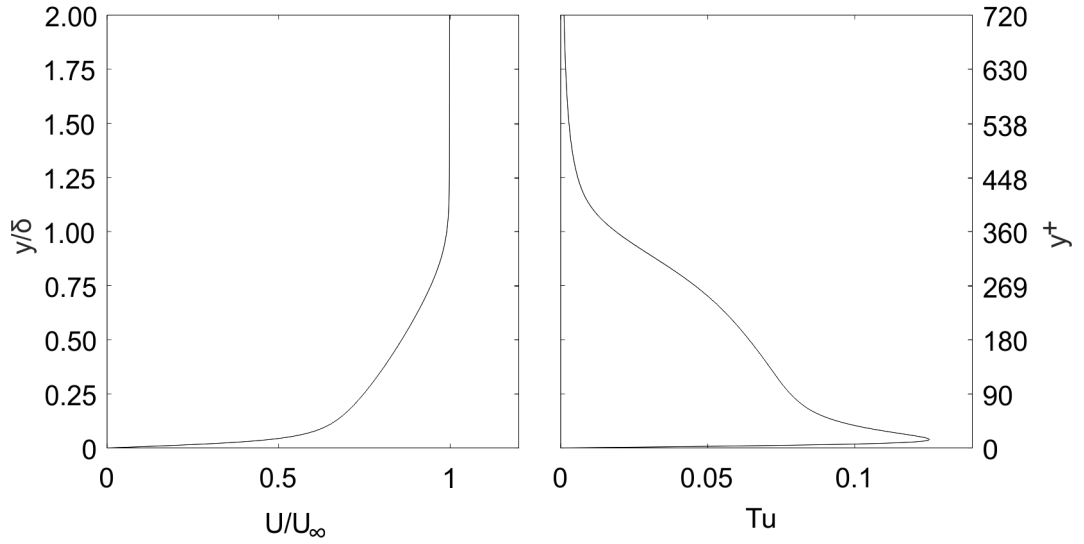

Figure 5.1: Distribution of velocity and turbulence in a turbulent boundary layer calculated with DNS (Schlatter and Örlu, 2010).

Close to the wall ($y/\delta < 1\%$), most of the local loss generation is due to the sharp mean velocity gradient imposed by the no-slip condition ($\overline{\Phi}^+/(\dot{S}^+_{vol}) = 83\%$). This component of loss rapidly decreases with increasing distance away from the wall. By $y/\delta = 4\%$, the contribution to the local loss generation is equally split between mean viscous dissipation ($\overline{\Phi}^+/(\dot{S}^+_{vol}) = 48\%$) and the turbulent dissipation ($\varepsilon^+/\dot{S}^+_{vol}) = 52\%$). Between $y/\delta = 7\%$ and $y/\delta = 80\%$, loss generation is largely dominated by turbulent kinetic energy dissipation, although the total value of loss generation is small: $\dot{S}^+_{vol}(y^+ = 100)$ is less than 10% of $\dot{S}^+_{vol}$ $(y^+ = 1)$. Well away from the wall, near the edge of the boundary layer, the entropy generation rate is zero.

The integral under the solid curve represents the total entropy generation inside the boundary layer. It is denoted as $\dot{S}_a$ and can be thought of as entropy generation per unit surface area. The non-dimensional entropy generation rate per unit surface area is known as the dissipation coefficient, C_D, defined in Equation 5.11a and on inner units in 5.11b.

$$C_D = \frac{T_\infty \dot{S}_a}{\rho U_\infty^3} = \frac{\int_0^\infty \overline{\Phi} dy}{\rho U_\infty^3} + \frac{\int_0^\infty \rho \varepsilon dy}{\rho U_\infty^3} \tag{5.11a}$$

$$C_D = \frac{\dot{S}_a^+}{U_\infty^{+3}} = \frac{\int_0^\infty \overline{\Phi}^+ dy^+}{U_\infty^{+3}} + \frac{\int_0^\infty \varepsilon^+ dy^+}{U_\infty^{+3}} \tag{5.11b}$$

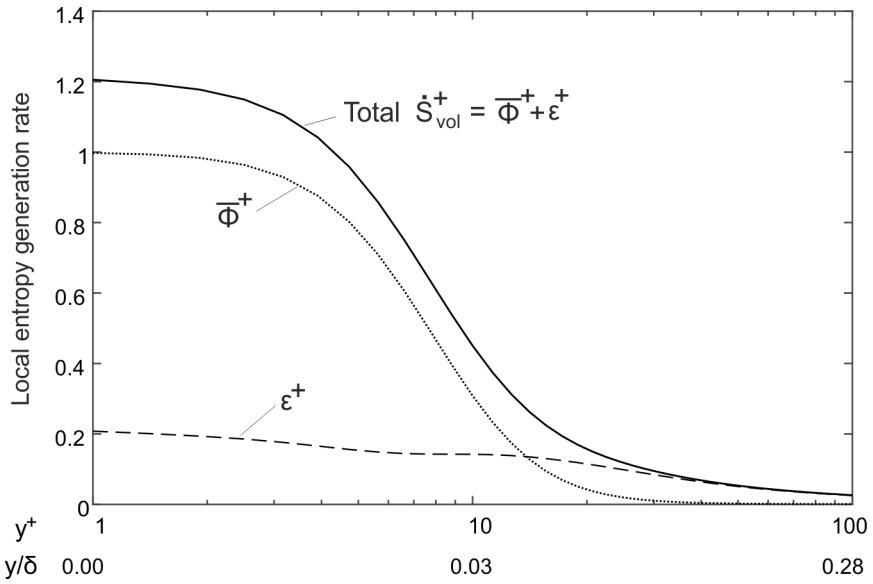

Figure 5.2: Distribution of entropy generation rate in a turbulent boundary layer calculated with DNS (Schlatter and Örlu, 2010). Entropy generation rate is presented on inner units.

Approximately 85% of the loss is generated within the first 30% of the boundary layer nearest to the wall. The non-dimensional boundary layer dissipation rate, defined in Equation 5.11, is shown for a developing boundary layer in Figure 5.3. Total entropy generation inside the boundary layer is almost equally split between the mean viscous dissipation, $\int_0^\infty \overline{\Phi}^+ dy^+$, and dissipation of turbulent kinetic energy, $\int_0^\infty \varepsilon^+ dy^+$.

Figure 5.3 shows that at a boundary layer Reynolds number of $Re_\theta = 1{,}000$, which is typical in turbomachines, the value of the overall dissipation coefficient is C_D =0.0018. The contribution of viscous dissipation and turbulent kinetic energy dissipation is equal. At higher boundary layer Reynolds numbers, where inertial terms are larger than viscous terms, the viscous dissipation in the boundary layer becomes less significant. The dissipation of turbulent kinetic energy in the boundary layer remains relatively constant and therefore contributes a larger portion of the overall entropy generation at higher Reynolds number.

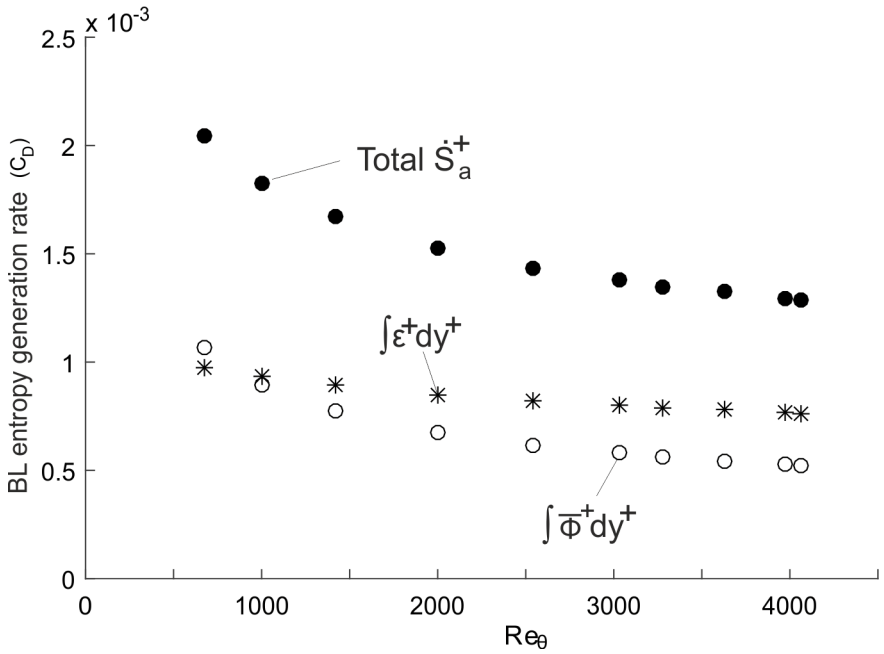

Figure 5.3: Integrated entropy generation rate in a turbulent boundary layer calculated with DNS (Schlatter and Örlu, 2010).

5.1.3 Application to a turbulent boundary layer with FST

A fundamental question of this thesis is how does combustor turbulence impact boundary layer loss? The approach to answer this question, with the loss framework of Method 1, is to measure the entropy generated inside the boundary layer. This section will show why this approach is incorrect for a boundary layer with high freestream turbulence.

The boundary layer in the previous example had zero freestream turbulence and zero freestream loss. In the presence of freestream turbulence, entropy will be generated in the freestream as the freestream turbulence decays. Any freestream turbulence that penetrates into the boundary layer and subsequently decays will also contribute to a rise in entropy generation. It will be shown in this section that the amount of entropy generated due to the decay of freestream turbulence is large, on the same order of magnitude as the amount of entropy generated inside the boundary layer with no freestream turbulence.

Entropy generation in a boundary layer with freestream turbulence is illustrated in Figure 5.4. The total loss is a superposition of boundary layer loss, caused by the presence of the wall, and 'background loss,' caused by the decay of freestream turbulence.

The magnitude of the background loss can only be estimated from scaling arguments since relevant measurements and computations, in high freestream turbulence, do not exist. To first order, the background loss can be can be approximated as the decay of freestream turbulence, $(\varepsilon)_{FS}$. The entropy generation rate, per unit volume, is then Equation 5.7 with an extra term:

$$T\dot{S}_{vol} = \frac{1}{\rho}\bar{\Phi} + \varepsilon + \varepsilon_{FS} \tag{5.12}$$

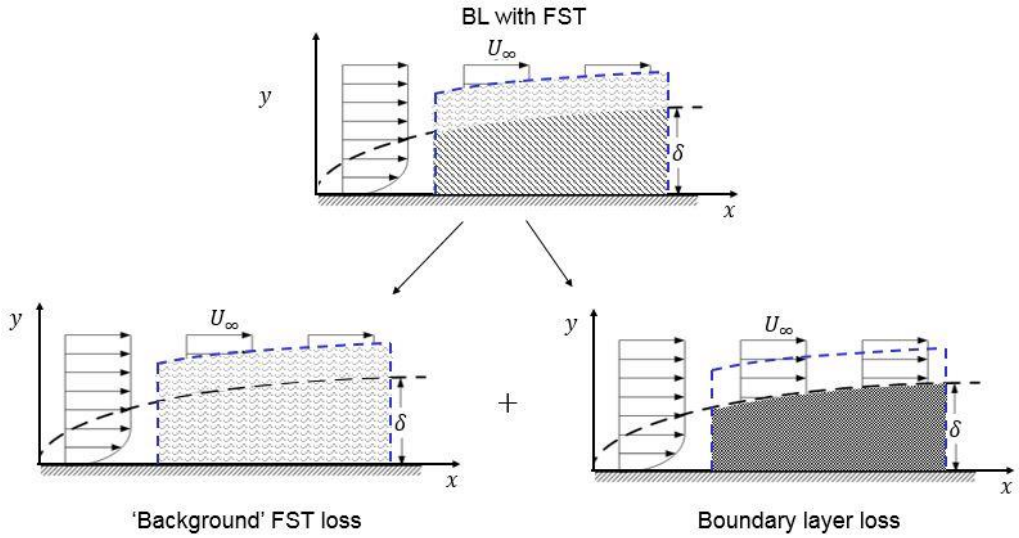

Figure 5.4: Schematic of entropy generation rate in a boundary layer with freestream turbulence.

A plausible scaling for the freestream dissipation, ε_{FS}, is to take the rate at which large eddies supply energy to the small eddies. The amount of turbulent kinetic energy of the large scales is proportional to $\overline{u^2}$ and the rate of transfer of energy is assumed to be proportional to u/Λ, where Λ represents the size of the largest eddies in the flow (Tennekes and Lumley, 1994, p. 20).

$$\varepsilon_{FS} \sim \overline{u^3}/\Lambda \tag{5.13}$$

Integrating the entropy generation rate, an extra term appears which scales with the cube of freestream turbulence and the ratio of boundary layer thickness to turbulent length scales.

$$C_D = \frac{\int_0^\infty \bar{\Phi} dy}{\rho U_\infty^3} + \frac{\int_0^\infty \rho\varepsilon dy}{\rho U_\infty^3} + Tu_{FS}^3\left(\frac{\delta}{\Lambda}\right) \tag{5.14}$$

Let us assume that the magnitudes of the first two terms on the right hand side do not change, i.e. freestream turbulence does not impact boundary layer loss. The magnitude of the third term on the right hand side can be estimated for a range of turbulence intensities and length scales using Equation 5.13.

For a freestream turbulence intensity of 20% and integral length scale of $\Lambda/\delta = 5$, the rise in C_D is 100%. This means that the extra entropy generated as the background turbulence dissipates is roughly equal to the entropy generated by the boundary layer in low freestream turbulence. In this method, the loss of a boundary layer has doubled due to the presence of freestream turbulence.

This reveals the downside of bookkeeping loss at the point of entropy generation in the presence of high freestream turbulence. We have attributed the decay of turbulence, which would have occurred with or without the presence of the wall, to the entropy generation of a boundary layer. In doing so we found that the loss coefficient of the boundary layer has doubled. Because the magnitude of 'boundary layer loss' and 'background loss' are comparable, determining the effect of combustor turbulence on boundary layer loss by measuring entropy generation becomes very difficult. The better approach is to decouple boundary layer loss from the background loss in the loss framework. This is done in Method 2 which is discussed next.

5.2 Method 2 – loss as having occurred when kinetic energy leaves the mean field

The second method defines loss as having occurred when mechanical energy has left the mean field. In the second method, loss is assumed to have occurred either when mean field kinetic energy has dissipated into internal energy or when mean field kinetic energy has been transformed into turbulent kinetic energy.

5.2.1 Mechanisms for mechanical energy dissipation

For a turbulent flow, the rate of change of kinetic energy in the mean field is given by Equation 5.15 (Hinze, 1975, p. 71):

$$\frac{D}{Dt}\frac{\overline{U}_i\overline{U}_i}{2} = -\frac{1}{\rho}\frac{\partial}{\partial x_j}(\overline{U}_j\bar{P}) + \frac{\partial}{\partial x_i}\left(-\overline{u_i u_j}\overline{U}_j\right) + \nu\frac{\partial}{\partial x_j}\overline{U}_i\left(\frac{\partial \overline{U}_i}{\partial x_j} + \frac{\partial \overline{U}_j}{\partial x_i}\right) - \frac{1}{\rho}\bar{\Phi} - \Pi \qquad (5.15)$$

The first term on the right hand side of Equation 5.15 is work done per unit mass and time by pressure. The sum of the kinetic energy term on the left hand side and the pressure work term on the right hand side represent the mechanical energy in a fluid available to a turbine.

The second and third terms on the right hand side of Equation 5.15 represent the rate at which turbulent and viscous stresses do work on the boundary. The fourth term, $\overline{\Phi}$, is given in Equation 5.2 and represents the mean viscous dissipation per unit mass. The fifth term on the right hand side of Equation 5.15, Π, represents the production of turbulent kinetic energy (Hinze, 1975, p72).

$$\Pi = -\overline{u_i u_j}\frac{\partial \overline{U}_j}{\partial x_i} \tag{5.16}$$

This term represents the transfer of energy from the mechanical energy into turbulent kinetic energy (or vice versa). When $i \neq j$, so that $-\overline{u_i u_j}$ is a shear stress, usually this stress has the same sign as $\partial \overline{U}_i / \partial x_j$. Hence for $i \neq j$, this term gives a negative contribution to the kinetic energy of the mean motion and a positive contribution to the turbulent kinetic energy (Hinze, 1975, p. 72).

Fundamentally, the term Π represents the work done by the mean shear on the turbulence through 'stretching' of turbulence vortex tubes. This is illustrated in Figure 5.5. As the vortex tube is stretched, the turbulent kinetic energy rises, drawing energy away from the mean flow.

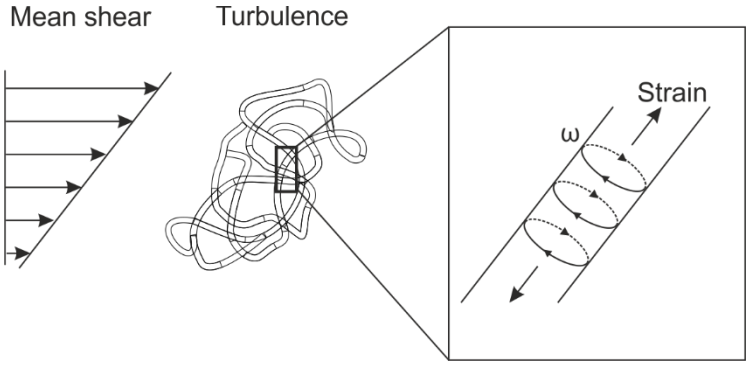

Figure 5.5: Schematic of mean shear acting on vortex tubes.

This section showed that there are two mechanisms by which kinetic energy of the mean flow can be changed. The first is the viscous dissipation of mean kinetic energy, $\overline{\Phi}$, which is always positive, raising the thermal energy of the fluid (higher temperature) at the expense of mechanical energy (lower mean kinetic energy). The second is the production of turbulent

kinetic energy, Π, which can be positive or negative, raising (or lowering) the turbulent kinetic energy of the fluid at the expense of mean kinetic energy. The production of turbulent kinetic energy does not raise the thermal energy of the fluid.

5.2.2 Dissipation of mechanical energy in boundary layers

The difference between Method 1 and Method 2 is the difference between production, Π, and dissipation, ε, of turbulent kinetic energy. In most flows, the production of turbulent kinetic energy is equal to the dissipation of turbulent kinetic energy (i.e. the flow is said to be in equilibrium). Figure 5.6 shows the calculation from DNS of production and dissipation of turbulent kinetic energy in a boundary layer.

Figure 5.6 shows that except for very near the wall ($y^+ < 20$), the production and dissipation of turbulent kinetic energy is similar. Integrated through the boundary layer, the difference between $\int \varepsilon^+ dy^+$ and $\int \Pi^+ dy^+$ is less than 5%.

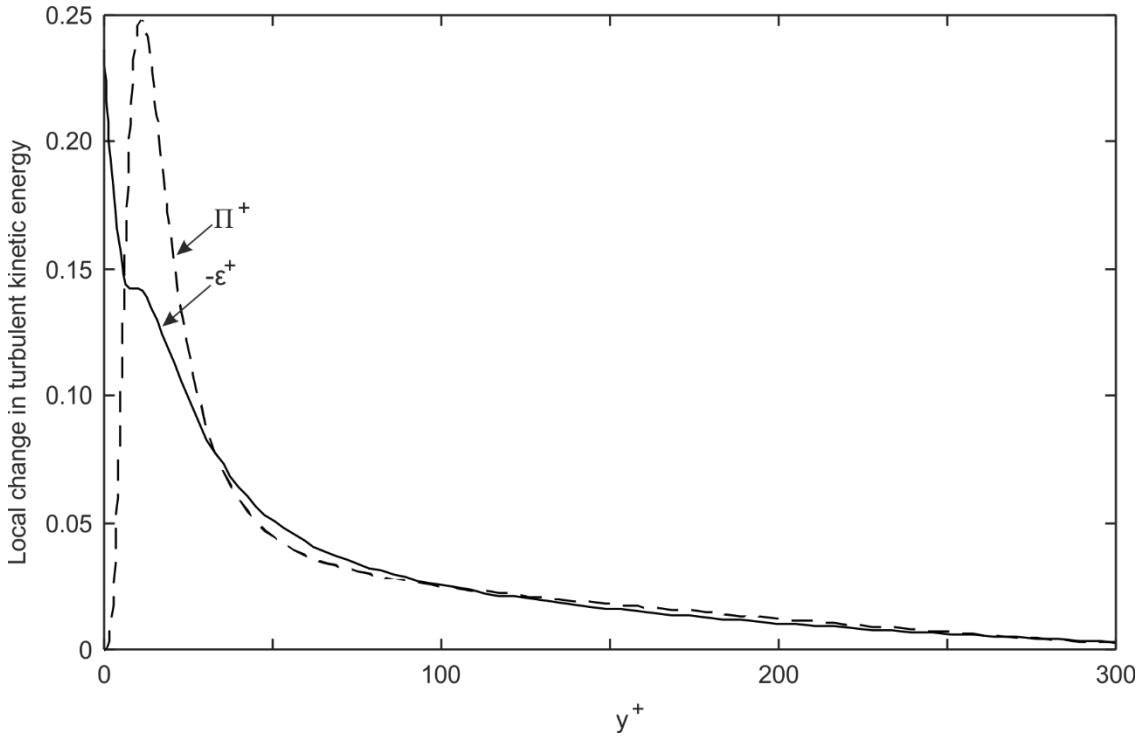

Figure 5.6: Production and dissipation of turbulent kinetic energy in a turbulent boundary layer calculated with DNS (Schlatter and Örlu, 2010).

For a closed domain with no work on the boundaries, the rate of change of mean kinetic energy is equal to the total viscous dissipation, $\bar{\Phi}$, and the production of turbulent kinetic

energy, Π, inside the control volume. Using this definition of loss, the dissipation coefficient, is defined in Equation 5.17

$$C_D = \frac{\int_0^\infty \bar{\Phi} dy}{\rho U_\infty^3} + \frac{\int_0^\infty \rho \Pi dy}{\rho U_\infty^3} \tag{5.17a}$$

$$C_D = \frac{\int_0^\infty \bar{\Phi}^+ dy^+}{U_\infty^{+3}} + \frac{\int_0^\infty \Pi^+ dy^+}{U_\infty^{+3}} \tag{5.17b}$$

Equation 5.17 should be compared with Equation 5.11. In Equation 5.17, the dissipation coefficient represents the non-dimensional rate of loss of kinetic energy from the mean flow, per unit surface area. In Equation 5.11, the dissipation coefficient represents the non-dimensional entropy generation rate per unit surface area, or the non-dimensional rate of loss of total kinetic energy. The difference between the two methods for a boundary layer in low freestream turbulence is small (Figure 5.6).

5.2.3 Application to a turbulent boundary layer with high FST

In the example above, the freestream turbulence is low. In cases where the freestream turbulence is high, the two loss analysis methods diverge. Both methods include the viscous dissipation of kinetic energy from the mean field, $\bar{\Phi}$. In the freestream, the velocity gradients in the mean field are low and so this term is effectively zero. Method 1 includes the viscous dissipation of turbulent kinetic energy term, ε. In the freestream this term is non-zero. Method 2 instead includes the production of turbulent kinetic energy term, Π. In the freestream this term is zero, because the term is proportional to the velocity gradient of the mean field which is zero. This makes Method 2 much easier to calculate and measure than Method 1.

5.3 Discussion of the methods

In this thesis, the second method of loss accounting is chosen. There are two reasons for this choice. First, 'book keeping' loss at the point where kinetic energy leaves the mean field is easier to deploy in a practical design system. Second, a real turbine cannot physically extract useful work from turbulent kinetic energy.

Up to this point in this chapter we have applied the methods only to a differential control volume. It is instructive to therefore show its application to a finite control volume. For an

adiabatic control volume with zero work and a single inlet and exit, where the inlet and exit are assumed to have a uniform mean field and a uniform turbulent kinetic energy, Equation 5.15 can be integrated over the control volume to give

$$\dot{m}\Delta\left(\frac{\bar{P}}{\rho}+\frac{1}{2}\overline{U_jU_j}\right)=-\rho\mathrm{D}-\dot{m}\Delta\left(\overline{u_iu_j}\right) \tag{5.18}$$

where

$$D=\int_{\mathcal{V}}\left(\frac{\overline{\Phi}}{\rho}+\Pi\right)d\mathcal{V} \tag{5.19}$$

For an incompressible flow, the left hand side of Equation 5.18 represents the change in the power which a turbine could extract from the mean flow. The first term on the right hand side represents the dissipation of mechanical energy from the mean field and production of turbulent kinetic energy. The second term on the right hand side represents the difference in the work done by Reynolds stresses on the inlet and exit of the control volume.

In a combustor the production of turbulent kinetic energy is high. This turbulent kinetic energy may not dissipate into entropy until several blade rows downstream of the combustor. The first method of loss accounting 'book keeps' this loss to partially occurring in the combustor and partially occurring in a number of downstream turbine stages. The second method of loss accounting 'book keeps' this loss as entirely occurring in the combustor. That is, if a control volume was placed around all of the turbine stages, downstream of the combustor, then the second term on the right hand side of Equation 5.18 is of fixed magnitude. This is because the inlet turbulence to the control volume is fixed by the upstream combustor, and at the exit to the control volume the combustor turbulence has dissipated. The aim of the designer should therefore be to minimize the dissipation function, D, within the downstream turbine.

The second reason for using the second method of loss accounting is that once turbulent kinetic energy has been created, it is practically difficult to extract useful work from it due to the small length scale of the turbulence relative to the blade chord.

Finally, measuring local dissipation of turbulent kinetic energy is very difficult using standard measurement techniques, because dissipation occurs at the smallest length scales of turbulence, which are often difficult to resolve. To adequately resolve the full dissipation spectrum requires either a very large scale of experiment or very small instrumentation.

Measuring the local production of turbulent kinetic energy, on the other hand, is much more achievable with standard measuring techniques. Stieger and Hodson (2003), for example, were able to measure turbulent production in a transitional boundary layer using Laser Doppler anemometry (LDA).

5.4 Loss in the freestream

Equation 5.18 shows that in an inviscid flow, the stagnation pressure of the mean field ($\bar{P} + \frac{1}{2}\rho\overline{U_j U_j}$) can be changed by two mechanisms. The first is the production of turbulent kinetic energy, Π, and the second is work done by Reynolds stresses on the inlet and exit of the control volume. Both of these mechanisms can occur in the freestream of a bladerow downstream of a combustor where the incoming high turbulence is rapidly accelerated. This section will discuss freestream loss in a turbine cascade.

For an inviscid flow, an area contraction will cause a rise in turbulent kinetic energy and thus a reduction of the stagnation pressure of the mean field. This is not intuitive, because a contraction is often used as a means of reducing turbulence intensity, e.g. in a low speed wind tunnel. Turbulence intensity, $Tu = \sqrt{\overline{uu}}/\sqrt{\bar{U}^2}$, is the ratio of the square root of turbulent kinetic energy in the streamwise direction relative to square root of the mean kinetic energy in the steamwise direction. In a one dimensional contraction, the numerator drops and the denominator rises.

However the turbulent kinetic energy in the lateral directions rises through a contraction. The change in the lateral energy dominates the total energy of the turbulence, which is always increased by the contraction of the stream (Batchelor, 1953, p.74). This effect is associated with a decrease in stagnation pressure in this inviscid contraction example.

The magnitude of this term can be calculated using rapid distortion theory (Batchelor, 1953). Assuming that the acceleration of turbulence occurs quickly enough to ignore turbulent inertia and viscous forces, the development of streamwise turbulence can be related to the contraction ratio, $c = A_{inlet}/A(x)$:

$$\frac{\overline{uu}(x)}{(\overline{uu})_{inlet}} = \frac{3}{4c^2}\left(\frac{1+a^2}{2a^3}\log\frac{1+a}{1-a} - a^2\right) \tag{5.20}$$

where $a^2 = 1 - c^3$. The ratio of the turbulent kinetic energy in the lateral components before and after the contraction is given by:

$$\frac{\overline{ww}(x) + \overline{vv}(x)}{(\overline{ww})_{inlet} + (\overline{vv})_{inlet}} = \frac{3c}{4} + \frac{3}{4c^2}\left(\frac{1}{2a^2} - \frac{1-a^2}{4a^3}\log\frac{1+a}{1-a}\right) \tag{5.21}$$

The sign of the production term in Equation 5.18 is negative; an increase in turbulent kinetic energy is associated with a reduction in stagnation pressure of the mean field. An increase in turbulent kinetic energy, and a corresponding decrease in freestream stagnation pressure, has previously been measured in a cascade with combustor inlet turbulence by Ames and Plesniak (1997).

Equation 5.18 shows that in an inviscid flow, the stagnation pressure of the mean field can also be changed by the imbalance of Reynolds stresses at the control volume inlet and exit. This represents a difference in the 'flow work' on the inlet and exit planes by the turbulent pressure (the isotropic Reynolds stress terms). These Reynolds stress terms are analogous to an additional pressure term acting on the inlet and exit of the control volume. The magnitude of the 'flow work' done by these terms can be estimated using the measured turbulent kinetic energy at the inlet and exit of the turbine cascade control volume. This term is usually negative, because the 'flow work' into the control volume is higher than out of the control volume.

5.5 Conclusions

This chapter has shown that in flow with high freestream turbulence, loss should be defined as having occurred when kinetic energy has left the mean field. This can occur either through dissipation of the kinetic energy of the mean field or by the conversion of the kinetic energy in the mean field into turbulent kinetic energy. In the following chapters, the magnitude of these two terms will be determined experimentally and used to determine both the magnitude of the boundary layer loss and the source of that loss. Outside the boundary layer, a rapid acceleration of turbulence may cause additional freestream loss.

Chapter 6
Boundary Layer Integral Equations

A complete determination of loss in a boundary layer requires the precise measurement of both viscous dissipation and turbulent production. This task can only be carried out with very specialised measurement techniques. It is, therefore, desirable to have a simpler relationship between boundary layer properties which are easier to measure and loss generation. Such methods are called boundary layer integral relations and have been widely used by the turbomachinery community since their development in the 1950's (Schlichting, 1968).

For cases where the freestream turbulence is high, the boundary layer momentum and kinetic energy integral equations contain a number of extra terms, compared to the form of the equations for low freestream turbulence. This chapter will show the form, physical meaning, and magnitude of these extra terms. The discussion in sections 6.1-6.3 follows the mathematical derivation presented in Hinze's classic textbook on turbulence (Hinze, 1975, pp. 588-597) but differs in that freestream turbulence terms are not neglected.

The development of boundary layer integral equations for high freestream turbulence has been considered by Ames (1990). Ames was motivated by inconsistencies in his measurements of skin friction using two different techniques. The present work builds on that analysis but includes additional terms which were suspected but never derived by Ames. In addition, the analysis is extended to the energy integral equation which has not yet been considered in high freestream turbulence.

The last section of this chapter demonstrates the rigor required when applying boundary layer integral relations in measurements with high freestream turbulence. The methods

described in this chapter are used in the following chapter to determine the effect of combustor turbulence on boundary layer dissipation experimentally.

6.1 Boundary layer approximation to equations of motion

It is useful to consider approximations to the equations of motion in a thin region of viscous flow, such as the flat plate boundary layer. This simplifies the equations significantly so the index notation which has been used in the previous chapter will be dropped in this chapter. In the case of a boundary layer, the 2-D Cartesian coordinate system has the origin at the wall with the x-axis in the direction of flow and the y-axis perpendicular to the surface. The corresponding components of mean velocity are $\overline{U}$ and $\overline{V}$ and the corresponding components of fluctuating velocity are u and v. Flow is assumed to be steady and incompressible and to have constant properties. Over a distance $\Delta x = L$, the boundary layer thickness grows to a thickness of δ and it is assumed that $\frac{\delta}{L} \ll 1$. Retaining only the highest order terms (order of magnitude assumptions are further discussed in Hinze, 1975, Chapter 7), the boundary layer approximations to continuity, momentum, and energy equations are given below.

Conservation of mass:

$$\frac{\partial \overline{U}}{\partial x} + \frac{\partial \overline{V}}{\partial y} = 0 \tag{6.1}$$

The x-component of the momentum equation:

$$\overline{U}\frac{\partial \overline{U}}{\partial x} + \overline{V}\frac{\partial \overline{U}}{\partial y} = -\frac{1}{\rho}\frac{\partial \overline{P}}{\partial x} - \frac{\partial}{\partial x}\overline{uu} - \frac{\partial}{\partial y}\overline{uv} + \nu\frac{\partial^2 \overline{U}}{\partial y^2} \tag{6.2}$$

It is typical to also neglect the second term on the right hand side of Equation 6.2 by order of magnitude analysis. This is because relative to the inertial terms on the left hand side, the magnitude of $\frac{\partial}{\partial x}\overline{uu}$ is small, of order 10^{-2}, for turbulence intensity of 20%. At larger values of turbulence, the order of this term increases, so it will be retained in the current analysis and its contribution will be discussed later in this chapter.

Next, the y-component of the momentum equation is considered. Using boundary layer assumptions, the gradients in the x-direction are taken to be negligible and the equation reduces to Equation 6.3 (Hinze, 1975, Equation 7.2).

$$\frac{1}{\rho}\frac{\partial \bar{P}}{\partial y} = -\frac{\partial}{\partial y}\overline{vv} \tag{6.3}$$

Integrating this equation in the wall normal direction yields:

$$\bar{P} + \rho\overline{vv} = P_{const} \tag{6.4}$$

Note the contrast between this and the corresponding laminar case where the static pressure is constant through the boundary layer. In a turbulent boundary layer, it is the sum of $\bar{P} + \rho\overline{vv}$ that is constant through the boundary layer. At the wall, the second term on the left hand side is zero. Therefore P_{const} also represents the static pressure measured by a wall static pressure tapping.

The streamwise derivative of pressure can be written as:

$$\frac{\partial \bar{P}}{\partial x} = \frac{dP_{const}}{dx} - \rho\frac{\partial \overline{vv}}{\partial x} \tag{6.5}$$

It is typical to neglect the second term on the right hand side of Equation 6.5 by order of magnitude analysis since $\frac{\partial}{\partial x}\overline{vv}$ is of the same order magnitude as $\frac{\partial}{\partial x}\overline{uu}$, and hence small (Hinze, 1975). Since this analysis extends boundary layer approximations to high freestream turbulence, this term will be retained and its magnitude discussed later in the chapter.

The x-momentum equation reduces to:

$$\bar{U}\frac{\partial \bar{U}}{\partial x} + \bar{V}\frac{\partial \bar{U}}{\partial y} = -\frac{1}{\rho}\frac{dP_{const}}{dx} + \frac{\partial}{\partial x}\overline{vv} - \frac{\partial}{\partial x}\overline{uu} - \frac{\partial}{\partial y}\overline{uv} + \nu\frac{\partial^2 \bar{U}}{\partial y^2} \tag{6.6}$$

Equation 6.6 differs from the classic boundary layer momentum equation (Hinze, 1975, Equation 7.3) in retaining the terms $\frac{\partial}{\partial x}\overline{uu}$ and $\frac{\partial}{\partial x}\overline{vv}$. This was done to extend the analysis framework for high freestream turbulence.

Similar approximations may be applied to the energy equation for the mean motion.

$$\frac{\partial}{\partial x}\bar{U}\left(\frac{\bar{P}}{\rho}+\frac{\bar{U}^2}{2}\right)+\frac{\partial}{\partial y}\bar{V}\left(\frac{\bar{P}}{\rho}+\frac{\bar{U}^2}{2}\right)$$
$$= -\bar{U}\left(\frac{\partial}{\partial x}\overline{uu}+\frac{\partial}{\partial y}\overline{uv}\right)-\bar{V}\left(\frac{\partial}{\partial x}\overline{uv}+\frac{\partial}{\partial y}\overline{vv}\right)+\nu\left(\bar{U}\frac{\partial^2\bar{U}}{\partial y^2}\right) \quad (6.7)$$

The static pressure can be replaced using y-momentum equation, Equation 6.4.

$$\frac{\partial}{\partial x}\bar{U}\left(\frac{\bar{P}_{const}}{\rho}-\overline{vv}+\frac{\bar{U}^2}{2}\right)+\frac{\partial}{\partial y}\bar{V}\left(\frac{\bar{P}_{const}}{\rho}-\overline{vv}+\frac{\bar{U}^2}{2}\right)$$
$$= -\bar{U}\left(\frac{\partial}{\partial x}\overline{uu}+\frac{\partial}{\partial y}\overline{uv}\right)-\bar{V}\left(\frac{\partial}{\partial x}\overline{uv}+\frac{\partial}{\partial y}\overline{vv}\right)+\nu\left(\bar{U}\frac{\partial^2\bar{U}}{\partial y^2}\right) \quad (6.8)$$

In the classic boundary layer energy equation (Hinze, 1975, Equation 7.4), the terms $\overline{vv}$, $\frac{\partial}{\partial x}\overline{uu}$, $\frac{\partial}{\partial y}\overline{vv}$ and $\frac{\partial}{\partial x}\overline{uv}$ are neglected by order of magnitude analysis. Again these terms will be retained in the current analysis for high freestream turbulence.

Interesting relations can be obtained by integrating equations 6.6 and 6.8 with respect to wall normal distance across the whole boundary layer. The momentum and kinetic energy integral equations are presented next.

6.2 Momentum integral equation

The momentum integral equation establishes the relationship between rate of development of the boundary layer momentum thickness and the viscous shear at the wall. The following derivation extends the traditional analysis to high freestream turbulence.

We begin by integrating the momentum equation with respect to y, from $y = 0$ (wall) to $y = y_\infty$, where $y_\infty > \delta$ is everywhere outside the boundary layer.

$$\int_0^{y_\infty}\left[\bar{U}\frac{\partial\bar{U}}{\partial x}-\bar{V}\frac{\partial\bar{U}}{\partial y}+\frac{1}{\rho}\frac{dP_{const}}{dx}-\frac{\partial}{\partial x}\overline{vv}+\frac{\partial}{\partial x}\overline{uu}+\frac{\partial}{\partial y}\overline{uv}\right]dy = \int_0^{y_\infty}\nu\frac{\partial^2\bar{U}}{\partial y^2}dy \quad (6.9)$$

If there is no mean shear in the freestream, the right hand side of Equation 6.9 is equivalent to the shear stress at the wall, τ_w/ρ. The normal velocity component, $\bar{V}$, can be replaced by the continuity equation:

$$\bar{V} = -\int_0^{y_\infty} \frac{\partial \bar{U}}{\partial x} \partial y \tag{6.10}$$

Consequently, the momentum equation becomes:

$$\int_0^{y_\infty} \left[\bar{U}\frac{\partial \bar{U}}{\partial x} - \left(\int_0^{y_\infty} \frac{\partial \bar{U}}{\partial x} \partial y \right) \frac{\partial \bar{U}}{\partial y} + \frac{1}{\rho}\frac{dP_{const}}{dx} - \frac{\partial}{\partial x}\overline{vv} + \frac{\partial}{\partial x}\overline{uu} + \frac{\partial}{\partial y}\overline{uv} \right] dy = \frac{\tau_w}{\rho} \tag{6.11}$$

The second term on the left hand side can be re-written using integration by parts.

$$\int_0^{y_\infty} \left[\frac{\partial \bar{U}}{\partial y} \left(\int_0^{y_\infty} \frac{\partial \bar{U}}{\partial x} dy \right) \right] dy = U_\infty \int_0^{y_\infty} \frac{\partial \bar{U}}{\partial x} dy - \int_0^{y_\infty} \bar{U}\frac{\partial \bar{U}}{\partial x} dy \tag{6.12}$$

Before carrying out the integration of the momentum-balance equation, the pressure term is expressed in terms of velocity. Outside of the boundary layer there is an inviscid region where the mean flow is one-dimensional in the streamwise direction. In this region, the x-momentum equation is given by:

$$\bar{U}_\infty \frac{d\bar{U}_\infty}{dx} = -\frac{1}{\rho}\frac{d\bar{P}_\infty}{dx} - \frac{d}{dx}(\overline{uu})_\infty \tag{6.13}$$

The previous section showed that in a turbulent boundary layer, the local static pressure is balanced by the local value of $\rho\overline{vv}$ so that the value $\bar{P} + \rho\overline{vv}$ is constant through the boundary layer. This applies in the freestream as well where $(\overline{vv})_\infty$ is non-zero for high freestream turbulence. The y-momentum equation in the freestream is given by:

$$\bar{P}_\infty + \rho(\overline{vv})_\infty = P_{const} \tag{6.14}$$

The x-momentum equation in the freestream, Equation 6.13, can therefore be re-written as:

$$\bar{U}_\infty \frac{d\bar{U}_\infty}{dx} = -\frac{1}{\rho}\frac{dP_{const}}{dx} + \frac{d}{dx}(\overline{vv})_\infty - \frac{d}{dx}(\overline{uu})_\infty \tag{6.15}$$

Replacing the pressure term in Equation 6.11, the momentum equation is:

$$\int_0^{y_\infty} \left[2\bar{U}\frac{\partial \bar{U}}{\partial x} - U_\infty \frac{\partial \bar{U}}{\partial x} - \bar{U}_\infty \frac{d\bar{U}_\infty}{dx} + \frac{d}{dx}(\overline{vv})_\infty - \frac{d}{dx}(\overline{uu})_\infty - \frac{\partial}{\partial x}\overline{vv} + \frac{\partial}{\partial x}\overline{uu} + \frac{\partial}{\partial y}\overline{uv} \right] dy = \frac{\tau_w}{\rho} \tag{6.16}$$

Which can be contracted to:

$$\int_0^{y_\infty} \frac{\partial}{\partial x}\left[\overline{U}\,(\overline{U}_\infty - \overline{U})\right]dy + \frac{d\overline{U}}{dx}\int_0^{y_\infty}(\overline{U}_\infty - \overline{U})\,dy + \int_0^{y_\infty}\left[\frac{d}{dx}(\overline{vv})_\infty - \frac{d}{dx}(\overline{uu})_\infty - \frac{\partial}{\partial x}\overline{vv} + \frac{\partial}{\partial x}\overline{uu} + \frac{\partial}{\partial y}\overline{uv}\right]dy = \frac{\tau_w}{\rho} \tag{6.17}$$

The first two terms can be rewritten with the definition of displacement thickness (δ^*) and momentum thickness (θ).

$$\delta^*\overline{U}_\infty = \int_0^{y_\infty}(\overline{U}_\infty - \overline{U})dy \tag{6.18}$$

$$\theta\overline{U}_\infty^2 = \int_0^{y_\infty}\overline{U}\,(\overline{U}_\infty - \overline{U})dy \tag{6.19}$$

Taking the integral and dividing all terms by $\overline{U}_\infty^2$:

$$\frac{\partial\theta}{\partial x} + \left(\frac{2\theta + \delta^*}{\overline{U}_\infty}\right)\frac{\partial\overline{U}_\infty}{\partial x} + \frac{\delta}{\overline{U}_\infty^2}\left(\frac{d}{dx}(\overline{uu})_\infty - \frac{d}{dx}(\overline{vv})_\infty\right) - \frac{d}{dx}\int_0^{y_\infty}\left(\frac{\overline{uu}}{\overline{U}_\infty^2} - \frac{\overline{vv}}{\overline{U}_\infty^2}\right)dy - \frac{(\overline{uv})_\infty}{\overline{U}_\infty^2} = \frac{\tau_w}{\rho\overline{U}_\infty^2} \tag{6.20}$$

The traditional momentum integral equation for the case of low freestream turbulence (Hinze, 1975, Equation 7.9) is given by: Equation 6.21:

$$\frac{\partial\theta}{\partial x} + \left(\frac{2\theta + \delta^*}{\overline{U}_\infty}\right)\frac{\partial\overline{U}_\infty}{\partial x} = \frac{C_f}{2} \tag{6.21}$$

Equation 6.20 differs from the classic momentum integral equation, Equation 6.21, because it contains three extra terms. First, the third and fourth terms on the left hand of Equation 6.20 do not exist in the traditional momentum integral equation. This is because the order of magnitude of $\frac{\partial}{\partial x}\overline{uu}$ and $\frac{\partial}{\partial x}\overline{vv}$ is small relative to the rest of the terms and they are traditionally considered negligible from the start. Since they have been kept in the current analysis, we can now comment on their contribution to the boundary layer integral equations.

Subsequent measurements in this thesis (Chapter 7), and work from other researchers (e.g. Dogan, 2014) have shown that high freestream turbulence penetrates deep into the boundary layer, superimposing freestream turbulence on top of traditional boundary layer turbulence.

These measurements show that the dominating length scale of freestream turbulence persists all the way from the freestream down to very near the wall. It is therefore a reasonable assumption that in such a case, the axial decay rate of turbulence in the boundary layer will behave in the same way as in the freestream. That is, the third and fourth terms will cancel each other out and have no contribution to the boundary layer development. Therefore these terms do not affect the momentum integral equation, even in high freestream turbulence.

The second difference between Equation 6.20 and 6.21 is the term $(\overline{uv})_\infty$. This term represents the work on the outer boundary of the control volume by Reynolds stresses. It is not negligible by order of magnitude analysis and is retained in the boundary layer equations. The term can be thought of as analogous to the work down by a shear force acting on a moving surface. However, when taking the integral of the x-momentum, classic analysis assumes that the freestream is does not contain turbulent shear. This is why $(\overline{uv})_\infty$ is traditionally set to zero (Hinze, 1975). It was shown in Chapter 4 that for the case of combustor turbulence, $(\overline{uv})_\infty$ is non-zero, and this term is, in fact, significant.

Making these assumptions, the momentum boundary layer integral equation simplifies to:

$$\frac{\partial\theta}{\partial x}+\left(\frac{2\theta+\delta^*}{\bar{U}_\infty}\right)\frac{\partial\bar{U}_\infty}{\partial x}-\frac{(\overline{uv})_\infty}{\bar{U}_\infty^2}=\frac{\tau_w}{\rho\bar{U}_\infty^2} \tag{6.22}$$

For a flat plate boundary layer with zero pressure gradient, the equation further simplifies to:

$$\frac{\partial\theta}{\partial x}-\frac{(\overline{uv})_\infty}{\bar{U}_\infty^2}=\frac{1}{2}C_f \tag{6.23}$$

In low freestream turbulence, the equation is the familiar:

$$\frac{\partial\theta}{\partial x}=\frac{1}{2}C_f \tag{6.24}$$

In his research in combustor turbulence in the 1990's, Ames predicted the effect of a non-zero Reynolds stress on the momentum integral equation. He summarises one particular experiment:

> "None of the momentum balances along the channel match the average skin friction with any degree of precision. This suggests that some factor(s) not

accounted for by either equations (3.12) or (3.14) are affecting the momentum balance. One possible explanation is a significant turbulent shear stress acting along the top of the control volume."

However, since he did not take Reynolds stress measurements in the freestream, Ames did not account for this effect further.

6.3 Energy integral equation

The energy integral equation establishes the relationship between rate of development of the boundary layer energy thickness and the dissipation of mean kinetic energy inside the boundary layer. The following derivation extends the traditional analysis to high freestream turbulence.

Integrating Equation 6.8 in the wall normal direction:

$$\int_0^{y_\infty} \frac{\partial}{\partial x}\left[\bar{U}\left(\frac{P_{const}}{\rho} - \overline{vv} + \frac{\bar{U}^2}{2}\right)\right] dy \; + \int_0^{y_\infty} \left[\bar{V}\left(\frac{P_{const}}{\rho} - \overline{vv} + \frac{\bar{U}^2}{2}\right)\right] dy$$
$$= -\int_0^{y_\infty} \frac{\partial}{\partial x}(\bar{U}\,\overline{uu} + \bar{V}\,\overline{uv})\, dy \; - \int_0^{y_\infty} (\,\bar{U}\overline{uv} + \bar{V}\,\overline{vv}\,)\, dy \qquad (6.25)$$
$$+ \int_0^{y_\infty} \Pi\, dy + \int_0^{y_\infty} \nu\bar{U}\frac{\partial^2 \bar{U}}{\partial y^2} dy$$

where production of turbulent kinetic energy in the boundary layer is given by:

$$\Pi = \overline{uu}\frac{\partial \bar{U}}{\partial x} + \overline{uv}\frac{\partial \bar{U}}{\partial y} + \overline{uv}\frac{\partial \bar{V}}{\partial x} + \overline{vv}\frac{\partial \bar{V}}{\partial y} \qquad (6.26)$$

Evaluating the second term on the left hand side and second term on the right hand side at the limits of integration, the equation can be re-written:

$$\int_0^{y_\infty} \frac{\partial}{\partial x}\left[\bar{U}\left(\frac{P_{const}}{\rho} - \overline{vv} + \frac{\bar{U}^2}{2}\right)\right] dy \; + \bar{V}_\infty \frac{P_{const}}{\rho} + \bar{V}_\infty \frac{\bar{U}_\infty^2}{2}$$
$$= -\int_0^{y_\infty} \frac{\partial}{\partial x}(\bar{U}\,\overline{uu} + \bar{V}\,\overline{uv})\, dy \; - \bar{U}_\infty(\overline{uv})_\infty + \int_0^{y_\infty} \Pi\, dy \qquad (6.27)$$
$$+ \int_0^{y_\infty} \nu\bar{U}\frac{\partial^2 \bar{U}}{\partial y^2} dy$$

The term V_∞ can be replaced by using continuity:

$$\bar{V}_\infty = -\int_0^{y_\infty} \frac{\partial \bar{U}}{\partial x}\, dy \tag{6.28}$$

The term P_{const} is constant and can be pulled out of the integral. After substituting Equation 6.28 into Equation 6.27, the two terms containing P_{const} on the left hand side cancel. Combining all of the $\partial/\partial x$ terms and moving the fluctuating terms to the right hand side:

$$\begin{aligned} &\frac{\partial}{\partial x}\int_0^{y_\infty}\left[\frac{\bar{U}^3}{2} - \frac{\bar{U}_\infty^2}{2}\bar{U}\right]dy \\ &\qquad = -\frac{\partial}{\partial x}\int_0^{y_\infty}(\bar{U}\overline{vv} + \bar{U}\,\overline{uu} + \bar{V}\,\overline{vv})\,dy - \bar{U}_\infty(\overline{uv})_\infty + \int_0^{y_\infty}\Pi\,dy \\ &\qquad + \int_0^{y_\infty} \nu\bar{U}\frac{\partial^2 \bar{U}}{\partial y^2}\,dy \end{aligned} \tag{6.29}$$

Simplifying and multiplying by -1:

$$\begin{aligned} &-\int_0^{y_\infty}\left[\frac{\partial}{\partial x}\left(\frac{\bar{U}^3}{2}\right)\right]dy + \int_0^{y_\infty}\left[\frac{\partial}{\partial x}\left(\frac{\bar{U}_\infty^2}{2}\bar{U}\right)\right]dy \\ &\qquad = \frac{\partial}{\partial x}\int_0^{y_\infty}(\bar{U}\overline{vv} + \bar{U}\,\overline{uu} + \bar{V}\,\overline{vv})\,dy + \bar{U}_\infty(\overline{uv})_\infty - \int_0^{y_\infty}\Pi\,dy \\ &\qquad - \int_0^{y_\infty} \nu\bar{U}\frac{\partial^2 \bar{U}}{\partial y^2}\,dy \end{aligned} \tag{6.30}$$

It is helpful to employ the definition of energy thickness (δ_e) at this point.

$$\delta_e \bar{U}_\infty^3 = \int_0^{y_\infty} \bar{U}\,(\bar{U}_\infty^2 - \bar{U}^2)dy \tag{6.31}$$

The left hand side of Equation 6.30 simplifies to:

$$\frac{d}{dx}\int_0^{y_\infty}\frac{1}{2}\bar{U}(\bar{U}_\infty^2 - \bar{U}^2)dy = \frac{d}{dx}\left(\frac{1}{2}\bar{U}_\infty^3\delta_e\right) \tag{6.32}$$

The last term on the right hand of Equation 6.30 side can be re-written using integration by parts:

$$\int_0^{y_\infty} \nu\bar{U}\frac{\partial^2\bar{U}}{\partial y^2}dy = \nu\left[\bar{U}\frac{\partial\bar{U}}{\partial y}\Big|_0^{y_\infty} - \int_0^{y_\infty}\left(\frac{\partial\bar{U}}{\partial y}\right)^2 dy\right]$$
$$= -\int_0^{y_\infty}\nu\left(\frac{\partial\bar{U}}{\partial y}\right)^2 dy = -\int_0^{y_\infty}\frac{\tau}{\rho}\frac{\partial\bar{U}}{\partial y}dy \tag{6.33}$$

Taking the integral and normalising the entire equation by $\bar{U}_\infty^3$:

$$\frac{1}{2}\frac{d\delta_e}{dx} + \frac{3}{2}\frac{1}{\bar{U}_\infty}\frac{d\bar{U}_\infty}{dx}\delta_e$$
$$= \frac{d}{dx}\int_0^{y_\infty}\left(\frac{\bar{U}}{\bar{U}_\infty^3}\overline{vv} + \frac{\overline{U}}{\bar{U}_\infty^3}\overline{uu} + \frac{\bar{V}}{\bar{U}_\infty^3}\overline{uv}\right)\partial y + \frac{(\overline{uv})_\infty}{\bar{U}_\infty^2} \tag{6.34}$$
$$+ \frac{1}{U_\infty^3}\int_0^{y_\infty}\frac{\tau}{\rho}\frac{\partial U}{\partial y}dy + \frac{1}{U_\infty^3}\int_0^{y_\infty} -\Pi\, dy$$

The traditional energy integral equation for the case of low freestream turbulence (Hinze, 1975, Equation 7.12) is given by Equation 6.35:

$$\frac{1}{2}\frac{d\delta_e}{dx} + \frac{3}{2}\frac{1}{\bar{U}_\infty}\frac{d\bar{U}_\infty}{dx}\delta_e = \frac{1}{U_\infty^3}\int_0^{y_\infty}\frac{\tau}{\rho}\frac{\partial U}{\partial y}dy + \frac{1}{U_\infty^3}\int_0^{y_\infty} -\overline{uv}\,\frac{\partial\bar{\mathrm{U}}}{\partial \mathrm{y}}dy \tag{6.35}$$

Equation 6.34 differs from the traditional energy integral equation, 6.35, in because it contains three extra terms. First, the first term on the right hand side of Equation 6.34 does not exist in the traditional momentum integral equation. This term represents the work on the inlet and exit boundary of the control volume by Reynolds stresses. This terms can be thought of analogous to an extra pressure acting on the inlet and exit of the control volume. This term is typically neglected because the order of magnitude of the terms $\overline{vv}$, $\frac{\partial}{\partial x}\overline{uu}$, $\frac{\partial}{\partial y}\overline{vv}$ and $\frac{\partial}{\partial x}\overline{uv}$ is small relative to the rest of the terms in the energy integral equation and they are traditionally considered negligible from the start. In cases where high freestream turbulence is non-negligible and changes in the streamwise direction, this term is non-zero. For example, Chapter 8, Section 2 of this thesis will show the magnitude of this term when the control volume is taken to be between the inlet and exit of a turbine cascade in high freestream turbulence. However, when the control volume is small, as was the case on the flat plate boundary layer at constant Re_θ, the magnitude of this term was found to be small.

The second difference between Equation 6.34 and 6.35 is the term $(\overline{uv})_\infty$. As discussed in the previous section, it is not negligible by order of magnitude analysis but is usually set to zero under the assumption that the freestream does not contain turbulent shear. For the case of combustor turbulence, $(\overline{uv})_\infty$ is non-zero, and this term is significant.

The third and final difference between Equation 6.34 and 6.35 is in the last term on the right hand side. In the current formulation, the production term in Equation 6.34, $(\Pi = \overline{uu}\frac{\partial \bar{U}}{\partial x} + \overline{uv}\frac{\partial \bar{U}}{\partial y} + \overline{uv}\frac{\partial \bar{V}}{\partial x} + \overline{vv}\frac{\partial \bar{V}}{\partial y})$, contains more terms than the production term in Equation 6.35 $(-\overline{uv}\ \frac{\partial \bar{U}}{\partial y})$. These terms have been neglected in the traditional energy integral equation by order of magnitude analysis. In this thesis, the production term is not measured, so the difference between these two formulations is not determined. Instead, the effect of turbulent production and viscous dissipation in the boundary layer is wrapped up into a single dissipation coefficient.

$$C_D = \frac{1}{U_\infty^3}\int_0^{y_\infty} \frac{\tau}{\rho}\frac{\partial U}{\partial y}dy + \frac{1}{U_\infty^3}\int_0^{y_\infty} -\Pi\, dy \tag{6.36}$$

Making the assumptions stated above, the kinetic energy boundary layer integral equation becomes:

$$\frac{1}{2}\frac{d\delta_e}{dx} + \frac{3}{2}\frac{1}{\bar{U}_\infty}\frac{d\bar{U}_\infty}{dx}\delta_e - \frac{(\overline{uv})_\infty}{\bar{U}_\infty^2} = C_D \tag{6.37}$$

For a zero pressure gradient flow, the kinetic energy integral equation is:

$$\frac{1}{2}\frac{d\delta_e}{dx} - \frac{(\overline{uv})_\infty}{\bar{U}_\infty^2} = C_D \tag{6.38}$$

In low freestream turbulence and for zero pressure gradient flow, the kinetic energy integral equation is:

$$\frac{1}{2}\frac{d\delta_e}{dx} = C_D \tag{6.39}$$

Again, the difference between Equations 6.38 and 6.39 is a Reynolds stress on the edge of the boundary layer.

6.4 Balancing the integral equations in high FST

The major difference between boundary layer integral analysis in grid and combustor freestream turbulence is the sensitivity of the analysis to the control volume which is chosen. When freestream turbulence is low (e.g. grid turbulence), the analysis of boundary layer measurements are insensitive to the location of the outer edge of the control volume, as long as it is located outside the boundary layer. When freestream turbulence is high (e.g. combustor turbulence), the analysis of the boundary layer measurement can become highly sensitive to the control volume that is chosen.

The reason for this sensitivity can be seen by comparing the momentum and kinetic energy integral equations in high and low freestream turbulence. The difference between Equations 6.13 and 6.14 and also between 6.26 and 6.27 is a Reynolds stress on the edge of the boundary layer. For combustor turbulence, $\overline{uv}$ is non-zero in the freestream, so momentum is transferred between streamlines in the freestream. It is therefore important, for whatever shape of control volume is chosen, that the value of $\overline{uv}$ is known on the outer edge of the control volume.

Figure 6.1 shows the measured Reynolds stress above the surface of the flat plate in combustor turbulence.

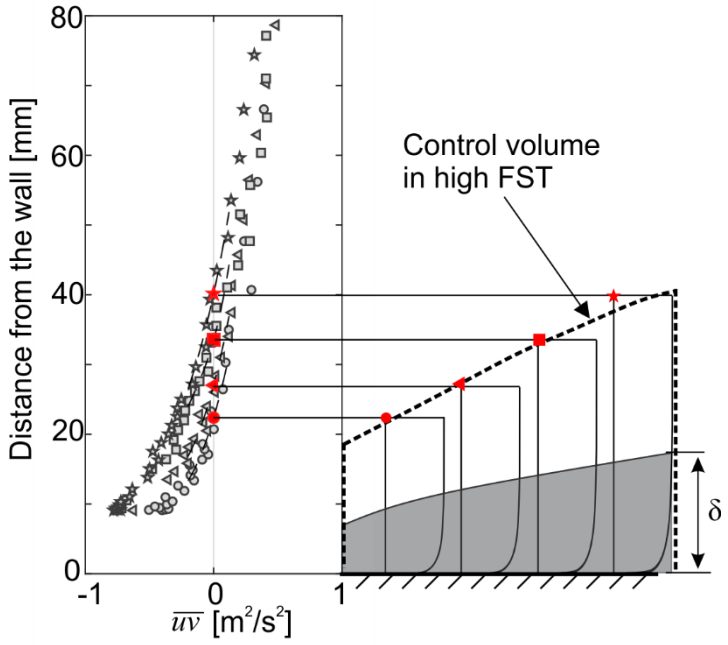

Figure 6.1: Measurements of Reynolds stress in combustor turbulence (left) and schematic of a control volume which has no freestream shear (right).

In the freestream (y > 70 mm), $\overline{uv}$ is non-zero and has a positive value and reduces near the wall. This is an inviscid effect that is caused by the distance from the wall reducing below the length scale of the largest turbulent eddies in the combustor turbulence. The effect is due to the 'image' vorticies created by the wall. In the boundary layer (y < ~40 mm), $\overline{uv}$ is negative as expected within a turbulent boundary layer.

6.4.1 Balancing the momentum integral equation

An example of the momentum integral equation balance is shown in Figure 6.2. It shows measurements of skin friction coefficient for the case of grid turbulence. The red circles show the direct method of determining C_f from the experimental measurements. This direct method involves fitting a canonical velocity profile to the measured velocity and using the resulting u_τ to calculate skin friction. The indirect method is determined from the rate of growth of momentum thickness. The two methods agree to within 4%. Figure 6.2 also includes the C_f calculated from DNS by Schlatter and Örlu, 2010. The DNS is for a flat plate with no freestream turbulence. The experiments and DNS are in close agreement.

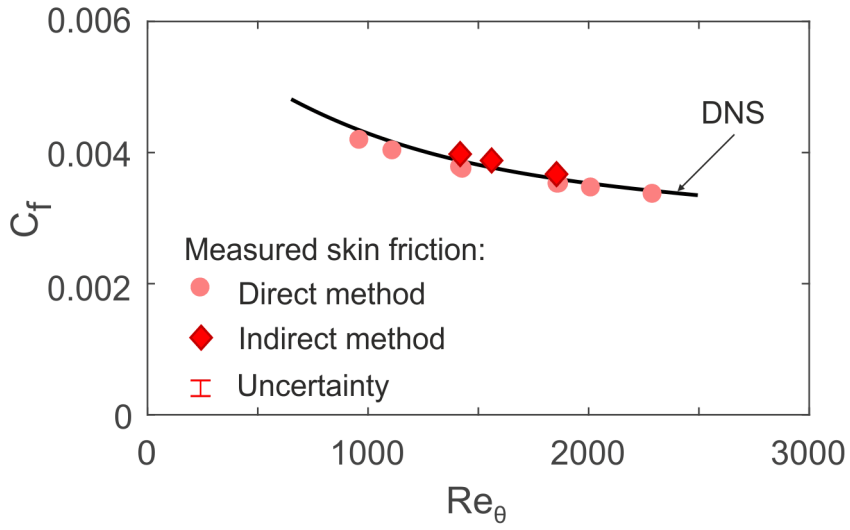

Figure 6.2: Skin friction variation on a flat plate. Measurements in grid turbulence and DNS with no freestream turbulence (Schlatter and Örlu, 2010).

For the case of grid turbulence with zero freestream Reynolds stress, the momentum integral is balanced. For the case of combustor turbulence, if the Reynolds stress in the freestream is not correctly accounted, the momentum integral equation will not balance. This is demonstrated with measurements in combustor turbulence in Table 6.1.

Table 6.1: Balancing the momentum integral equation

		Grid Tu	Combustor Tu
Measured	$\frac{1}{2}C_f$	0.002140	0.00270
	$\frac{d\theta}{dx}$	0.002098	0.003591
	Difference	1.94%	-33%
Inferred	$\frac{(\overline{uv})_\infty}{U_\infty^2}$	0	0.000891

The momentum balance of the boundary layer in grid turbulence is straightforward. The difference between $\frac{1}{2}C_f$ and $\frac{d\theta}{dx}$ is 2%, which is within the uncertainty. The momentum balance of the boundary layer in combustor turbulence is more complicated. There is a 33% imbalance between $\frac{1}{2}C_f$ and $\frac{d\theta}{dx}$. The imbalance is due to the turbulence shear term on the freestream boundary, $(\overline{uv})_\infty$. The magnitude of this term can be calculated from Equation 6.13 and is shown in Table 6.1.

6.4.2 Balancing the kinetic energy integral equation

The same balance cannot be performed for the kinetic energy integral equation (Equation 6.38) because the measurement of dissipation coefficient is less straightforward than the measurement of skin friction. It requires the local measurement of production of turbulent kinetic energy, $\left(\overline{uv}\frac{d\bar{U}}{dy}\right)$. In the present work, the cross wire spatial resolution was not adequate to accurately resolve the local $\overline{uv}$ throughout the boundary layer.

To close the balance of Equation 6.38, one of two approaches are available. Either the control volume is drawn such that the edge of the boundary layer is defined where the shear stress is zero (e.g. Figure 6.1) or the freestream Reynolds stress is calculated from the balance of the momentum integral equation (e.g. Table 6.1).

Control volume defined by zero freestream shear

A convenient definition of the control volume outer edge is to define it along the line of $\overline{uv}$=0. This is shown on the right hand side of Figure 6.1. This definition of control volume was found to result in an extremely accurate balance of the momentum integral equation in cases with combustor turbulence and will be used in all cases of combustor turbulence. Far away from

the wall, the Reynolds stress, normalized by the square of freestream velocity, is positive and varies between 0.0004 to 0.0009. This is equivalent to 22%-50% of the boundary layer dissipation coefficient at $Re_\theta = 1{,}000$ (shown to be $C_D = 0.0018$ in low freestream turbulence, Chapter 5).

Freestream shear determined from momentum integral equation

The value of the Reynolds stress in the freestream can be deduced from the momentum integral equation. An example is shown in Table 6.1. In this example, the upper limit of integration was a distance equal to several boundary layer thicknesses away from the wall. The balance of the momentum integral equation determines that the Reynolds stress in the freestream, normalized by the square of freestream velocity, is positive and equal to 0.0009. This can be compared with the value of the Reynolds stress measured in the freestream (Figure 6.1). Far away from the wall, the Reynolds stress, normalized by the square of freestream velocity, is positive and equal to 0.0006 ±0.0003. The uncertainty is high because the measurements of $(\overline{uv})_\infty$ were not taken at the same location as the boundary layer in Table 6.1. However, the sign and approximate magnitude of the freestream Reynolds stress which was measured and analytically determined match.

6.5 Conclusions

This chapter has shown that the boundary layer integral equations contain extra terms in the presence of combustor turbulence. It was shown that when the freestream turbulence is high the relationship between the rise in energy thickness and dissipation coefficient is sensitive to the shape of the boundary layer control volume. This is because momentum transfer is significant in the freestream. By specifying the correct boundary layer control volume, it was shown that the rise in energy thickness and dissipation coefficient can be balanced. This is important because it means that energy thickness can still be used as a measure of loss in flows of high freestream turbulence. This methodology is applied to a flat plate and the results are presented in the following chapter.

Chapter 7
Flat Plate Boundary Layer Loss

Boundary layer loss is a major source of the total loss in the turbine. The previous chapters have illustrated that this loss can occur through two mechanisms: the viscous dissipation of kinetic energy from the mean field and the production of turbulent kinetic energy. This chapter will investigate the effect of combustor turbulence on a boundary layer loss and determine which of the two mechanisms is responsible for the change. Experiments were undertaken on a flat plate to ensure that acceleration and curvature was removed from the problem. The measurements discussed here are summarized in Table 7.2 at the end of this chapter.

7.1 Boundary layer profile

The aim of this section is to determine the change in loss in a turbulent boundary layer due to the presence of combustor turbulence. The presence of high freestream turbulence changes the formulation of the integral boundary layer equations, which was discussed in Chapter 6. It is important to understand how the boundary layer loss presented in this section should be interpreted. The freestream has a non-zero loss. The boundary layer loss should be interpreted as the loss relative to this freestream loss.

Figure 7.1 shows the impact of combustor turbulence on the flat plate boundary layer (Re_θ =2,000). The presence of combustor turbulence can be seen to reduce the shape factor of the boundary layer from H_{12} = 1.43 to 1.30. It will be shown that this results from a deep penetration of the combustor turbulence into the boundary layer.

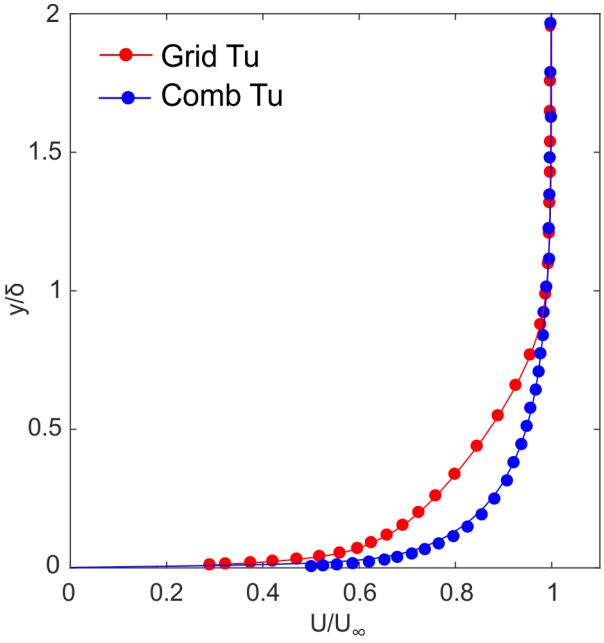

Figure 7.1: Boundary layer measured in grid and combustor turbulence.

The velocity profiles shown in Figure 7.1 are presented on inner units in Figure 7.2. The region closest to the wall (first 20-40% of the boundary layer) is called the inner region and accounts for 85% of the loss due to viscous dissipation. When scaled by the respective skin friction, the velocity profiles in combustor and grid turbulence collapse onto a single curve.

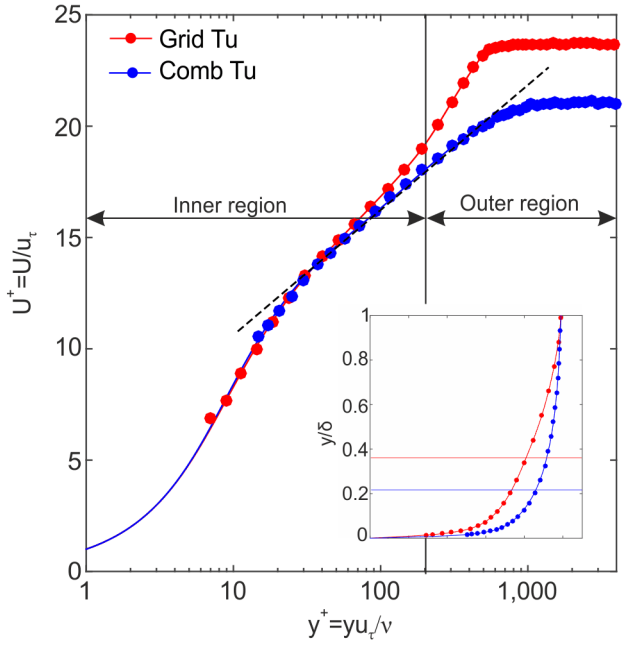

Figure 7.2: Boundary layer measured in grid and combustor turbulence, presented on inner units. The insert shows the demarcation of inner and outer regions at $y^+ = 200$.

The velocity profile in the outer region, which takes up the outer 60-80% of the boundary layer, depends on Reynolds stresses. The velocity profile in grid turbulence rises above the logarithmic law, which is indicated with the black dashed line. This indicates a positive wake and is typical of turbulent boundary layers in a quiet freestream. The velocity profile in combustor turbulence falls below the logarithmic law. This indicates a supressed wake, and is typical of pipe flows where the freestream has turbulence.

7.2 Skin friction

The skin friction coefficient for the case of grid turbulence and combustor turbulence is shown in Figure 7.3. The solid circles show the direct method of determining C_f from the experimental measurements. This direct method involves fitting a canonical velocity profile to the measured velocity and using the resulting u_τ to calculate skin friction. The solid diamonds show the indirect method of determining C_f from the rate of growth of momentum thickness (C_f=$2d\theta/dx$). For both cases of freestream turbulence, the two methods agree to within 4%. Figure 7.3 shows that the presence of combustor turbulence causes a 20% rise in skin friction.

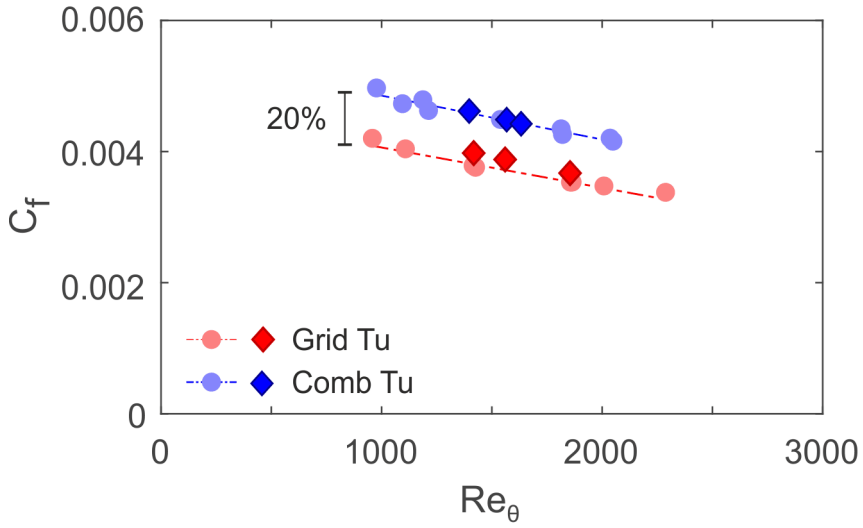

Figure 7.3: Skin friction variation on a flat plate measured in grid and combustor turbulence.

The effect of combustor turbulence on the shape of the boundary layer across a range of boundary layer Reynolds numbers is shown in Figure 7.4. It can be seen that the presence of combustor turbulence causes, on average, a 9% reduction in the shape factor, H_{12}, and a 4% reduction in the shape factor, H_{23}.

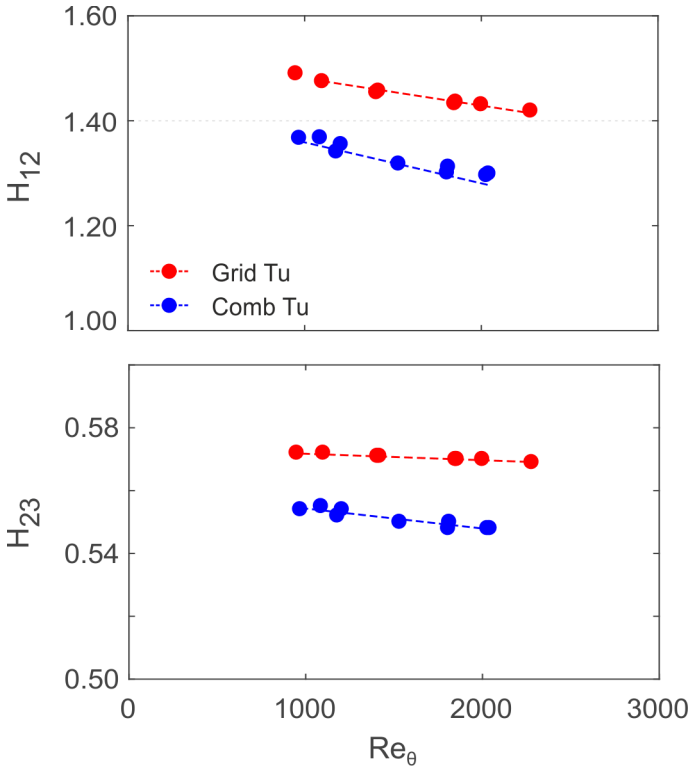

Figure 7.4: Shape factor variation on a flat plate measured in grid and combustor turbulence

In summary, the presence of combustor turbulence causes a fuller boundary layer profile with a corresponding rise in skin friction.

7.3 Boundary layer dissipation

The dissipation coefficient for the case of grid turbulence is shown in Figure 7.5. The red points show C_D calculated from the experimental measurements, and the black line shows C_D calculated from DNS (Schlatter and Örlu, 2010). The experiment and DNS are in close agreement. In Figure 7.5, the black dashed line shows the correlation for C_D given by Schlichting (1968). The trend of the correlation can be seen to disagree with the present experiment and DNS.

The dissipation coefficient for the case of combustor turbulence is included in Figure 7.6. The blue points show C_D calculated from the experimental methods. The blue solid line in Figure 7.6 shows the best fit to DNS scaled by an empirical factor of 1.22. This shows that the presence of combustor turbulence causes a 22% rise in C_D.

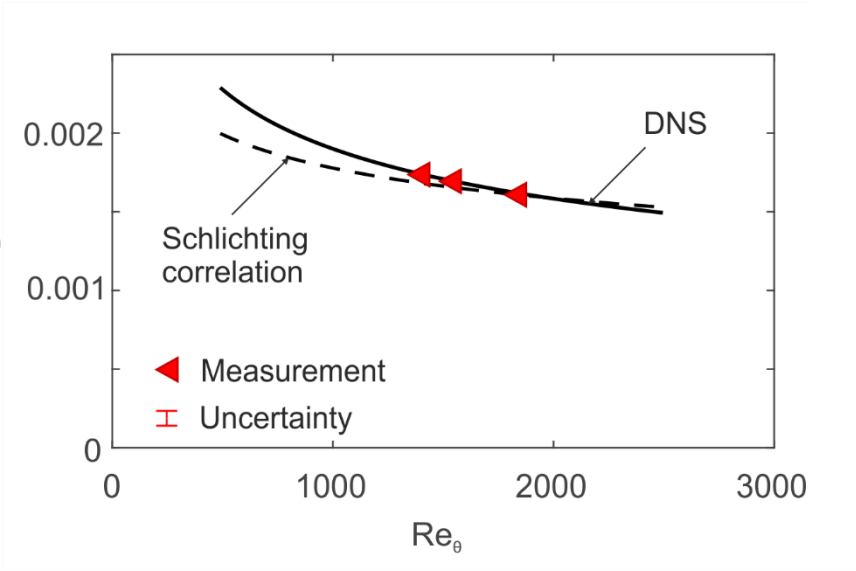

Figure 7.5: Dissipation coefficient on a flat plate (measured, calculated, and correlation).

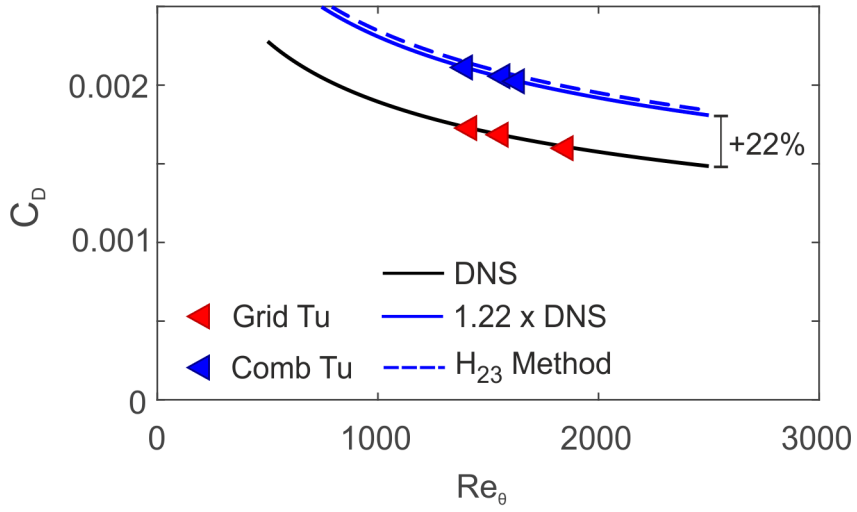

Figure 7.6: Dissipation coefficient on a flat plate in grid and combustor turbulence.

A second method of calculating the rise in C_D due to the presence of combustor turbulence is through the measured change in H_{23} and the measured change in C_f.

$$C_D = \frac{C_f}{4H_{23}} - \frac{1}{2}\frac{\theta}{H_{23}^2}\frac{dH_{23}}{dx} \tag{7.1}$$

For an equilibrium boundary layer, H_{23} changes slowly, so the second term is much smaller than the first term. The change in dissipation coefficient due to combustor turbulence can therefore be determined if the change in C_f (Figure 7.3) and the change in H_{23} (Figure

7.4) are known. The dissipation coefficient for the case of combustor turbulence, calculated using this second method, is shown as the dashed blue line in Figure 7.6. This method predicts that C_D increased by 24%, which is similar to the first method.

To summarize, Figure 7.6 shows two independent methods of calculating the increase in C_D caused by combustor turbulence. The two methods both show that the presence of combustor turbulence causes C_D to rise by between 22% and 24%.

7.4 Physical mechanism

The power spectrum of the flat plate boundary layers shown in Figure 7.1 (Re_θ=2000), for the cases of grid and combustor turbulence, are shown in Figure 7.7 (on outer units) and Figure 7.8 (on inner units). The left hand side of Figures 7.7 and 7.8 shows the spectrum for the grid turbulence case. The right hand side of Figures 7.7 and 7.8 shows the spectrum for the combustor turbulence case.

Figures 7.7 and 7.8 (left hand side) show the expected behaviour for a turbulent boundary layer with a peak in turbulent kinetic energy emanating from the wall. Figure 7.8 shows that in grid turbulence, the spectrum is dominated by one peak very near the wall at y^+ =15 and λ^+=1,650. This is called the inner peak. It is associated with turbulence production near the wall. The inner peak occurs at roughly the same location and length scale (scaled on inner units) for any flat plate boundary layer in low freestream turbulence (Hutchins and Marusic, 2007).

Figures 7.7 and 7.8 (right hand side) show a very different behaviour. The combustor turbulence can be observed to penetrate deep into the boundary layer. Figure 7.8 shows that in combustor turbulence, the spectrum has a high band of turbulent kinetic energy, at λ^+=10,000, stretching from the freestream down to into the freestream to y^+~50. The inner peak can clearly be seen at around y^+=15.

In addition, at around y^+=500 (or y/δ = 0.4), combustor turbulence can be seen to be amplified by the boundary layer. This mechanism is the result of mean shear in the boundary layer stretching the eddies imposed into the boundary layer by the combustor turbulence.

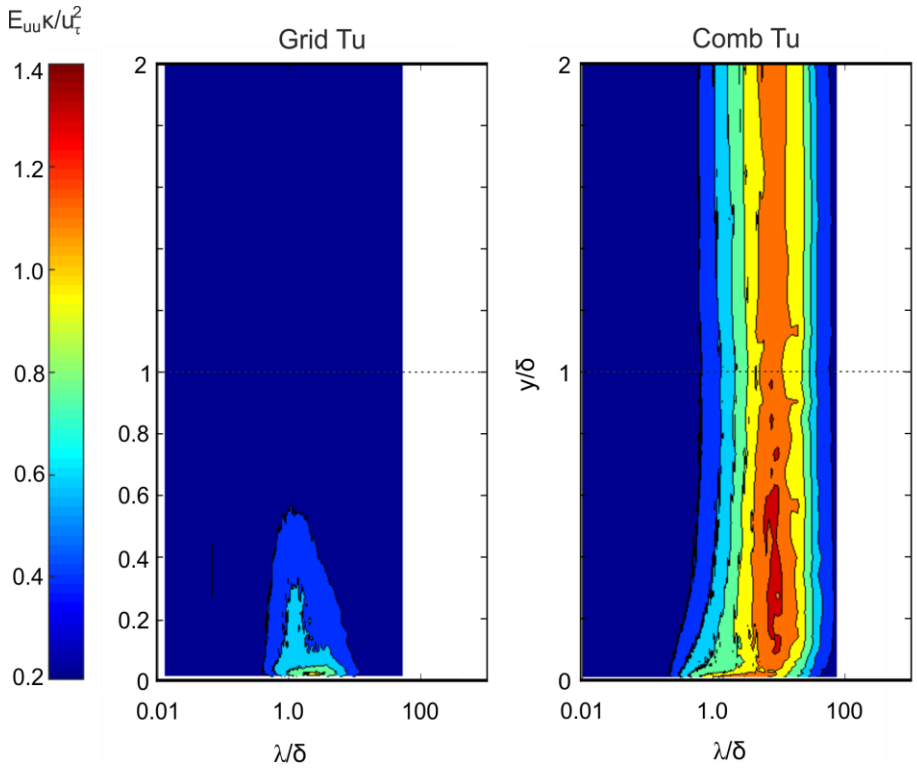

Figure 7.7: Contour maps of pre-multiplied energy spectra of streamwise fluctuating velocity in grid (left) and combustor (right) turbulence on outer units.

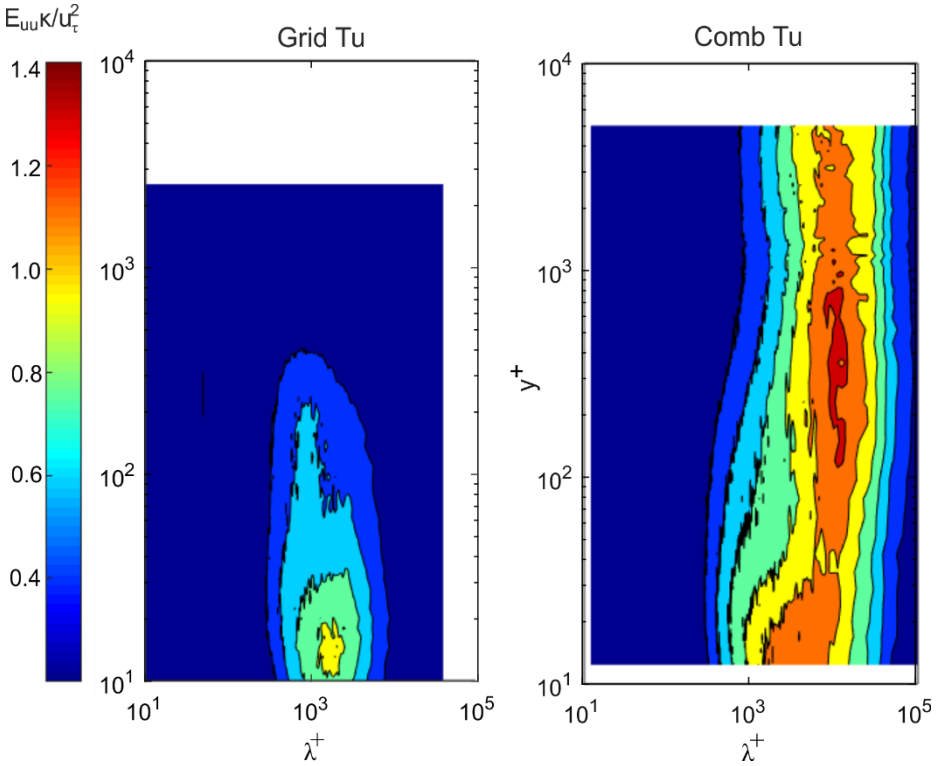

Figure 7.8: Contour maps of pre-multiplied energy spectra of streamwise fluctuating velocity in grid (left) and combustor (right) turbulence on inner units.

Figure 7.9 shows the variation of skewness and kurtosis through the boundary layer. Skewness (Equation 7.2) is a measure of the symmetry of the velocity fluctuations. The normal distribution has a skew factor of zero (Tennekes and Lumley, pg. 200).

$$SF = \frac{\overline{u^3}}{\left(\overline{u^2}\right)^{3/2}} \tag{7.2}$$

Kurtosis (Equation 7.3) is a measure of the width of the probability distribution of the velocity fluctuations and describes how outlier-prone a distribution is. A normal distribution has a kurtosis factor of three (Tennekes and Lumley, pg. 200).

$$KF = \frac{\overline{u^4}}{\left(\overline{u^2}\right)^2} \tag{7.3}$$

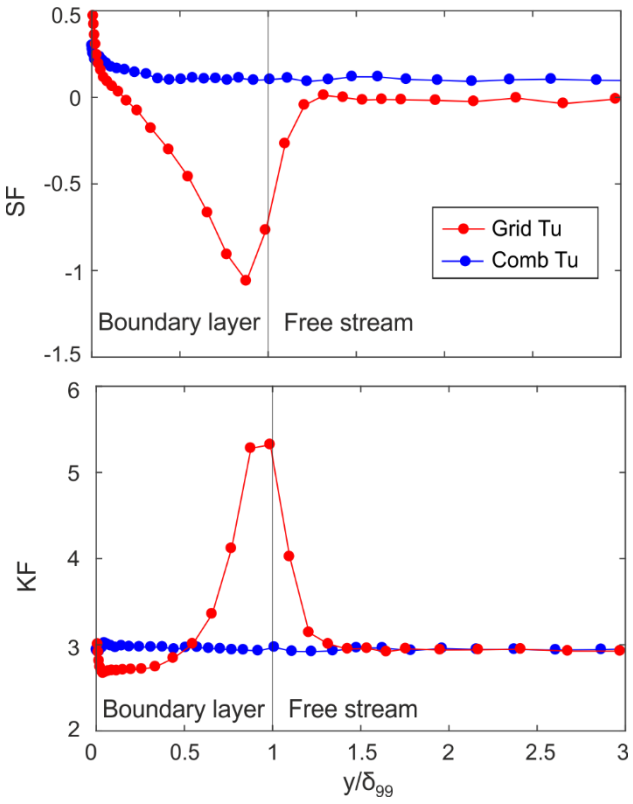

Figure 7.9: Variation of skew factor (top) and kurtosis factor (bottom) through the boundary layer in grid and combustor turbulence.

Figure 7.9 shows that combustor turbulence dominates the velocity fluctuations through the boundary layer, down to very close to the wall. The trough in skew and peak in kurtosis,

expected at the edge of the boundary layer in a normal turbulent boundary layer, have been completely removed by combustor turbulence. In conclusion, the combustor turbulence penetrates down to very close to the wall, dominating the turbulent structure of the boundary layer.

7.4.1 Cause of increase in dissipation

Chapter 5 showed that viscous dissipation in a boundary layer is the result of one of two mechanisms:

$$C_D = \frac{\int_0^\infty \bar{\Phi} dy}{\rho U_\infty^3} + \frac{\int_0^\infty \rho \Pi dy}{\rho U_\infty^3} \tag{7.4}$$

The first term is the viscous dissipation of kinetic energy from the mean field. The second term is the conversion of kinetic energy from the mean field to turbulent kinetic energy (production of turbulent kinetic energy). The first term was measured, and the second term was deduced from the overall rise in C_D. The results at $Re_\theta = 2{,}000$ are shown in Table 7.1. At this Re_θ the exact rise in C_D due to the presence of combustor turbulence is 20.4%. The cause of the rise can now be identified with Equation 7.4.

Table 7.1: Measured components of $\boldsymbol{C_D}$ for a flat plate boundary layer

	Grid Tu	**Comb Tu**	**Relative Change**
C_D	1.576×10^{-3}	1.897×10^{-3}	+20.4%
C_D^{mean}	0.627×10^{-3}	0.846×10^{-3}	+35% (68% of the rise)
C_D^{turb}	0.949×10^{-3}	1.051×10^{-3}	+11% (32% of the rise)

Of the total rise, 68% is due to a rise in the viscous dissipation of kinetic energy from the mean field. This is due to the shape of the boundary layer changing, as shown in Figure 7.1.

The remaining 32% of the rise is due to an increase in the production of turbulent kinetic in the boundary layer. As the freestream turbulence enters the boundary layer, it is distorted by the mean shear in the boundary layer raising the production of turbulent kinetic energy. This can be seen from the peak in turbulent kinetic energy in the lower part of Figure 7.7.

7.5. Conclusions

It has been shown that the major effect of combustor turbulence is to make the boundary layer profile fuller (H_{12} changes from ~1.4 to ~1.3). The presence of freestream turbulence was found to raise the dissipation coefficient by 20%. This was found to be caused by two mechanisms: ~50% of the rise is due to an increase in the dissipation of kinetic energy from the mean field. This is due to the fuller boundary layer profile. The ~50% remaining rise is due to an increase in the production of turbulent kinetic energy caused by penetration of freestream turbulence into the boundary layer.

Table 7.2: Measurements on a flat plate in grid and combustor turbulence

	x [m]	Re_θ	u_τ [m/s]	$\bar{U}_\infty$ [m/s]	δ [mm]	δ^* [mm]	θ [mm]	δ_e [mm]	H_{12}	H_{23}	C_f (Direct method)	C_f (Indirect method)	C_D
Grid Turbulence	0.3	1,101	1.0350	23.2	6.2	1.06	0.72	1.25	1.475	0.572	0.003984		
	0.6	**1,999**	**0.9664**	**23.4**	**10.7**	**1.85**	**1.29**	**2.26**	**1.431**	**0.570**	**0.003418**	0.003828	0.001685
	0.25	950	1.0627	23.3	5.3	0.91	0.61	1.07	1.490	0.572	0.004145		
	0.4	1,418	0.9996	23.2	7.7	1.34	0.92	1.60	1.457	0.571	0.003703		
	0.55	1,856	0.9703	23.3	10.0	1.72	1.20	2.10	1.436	0.570	0.003478	0.003926	0.001727
	0.4	1,407	1.0300	23.9	7.6	1.32	0.91	1.59	1.454	0.571	0.003729		
	0.55	1,849	0.9975	23.9	10.1	1.70	1.19	2.08	1.433	0.570	0.003476		
	0.7	2,279	0.9858	24.2	12.2	2.06	1.45	2.55	1.419	0.569	0.003321	0.00362	0.001599
Combustor Turbulence	0.2	970	1.035	20.9	8.7	1.0	0.7	1.3	1.37	0.554	0.00492		
	0.25	1,180	1.063	21.8	10.5	1.1	0.8	1.5	1.34	0.552	0.00474		
	0.35	1,532	1.026	21.8	14.5	1.4	1.1	1.9	1.32	0.550	0.00444		
	0.45	1,807	0.996	21.5	18.5	1.7	1.3	2.3	1.30	0.548	0.00430	0.00458	0.00212
	0.2	1,093	1.035	21.4	9.5	1.1	0.8	1.4	1.37	0.555	0.00468		
	0.3	1,813	0.982	21.4	17.6	1.7	1.3	2.4	1.31	0.550	0.00421		
	0.5	**2,029**	**0.982**	**21.6**	**21.1**	**1.9**	**1.5**	**2.6**	**1.30**	**0.548**	**0.004156**	0.00444	0.0021
	0.25	1,205	1.0083	21	11	1.2	0.88	1.6	1.36	0.55	0.004578		
	0.55	2,042	0.930641	21	23	2	1.54	2.8	1.3	0.55	0.004109	0.004382	0.002027

Chapter 8
Cascade Loss

The aim of this chapter is to determine the effect of combustor turbulence on loss mechanisms in a cascade. The cascade chosen and the loss analysis applied are described in Chapter 3. The total loss coefficient of the turbine cascade, with both grid and combustor turbulence, is shown in Figure 8.1 and tabulated in Table 8.1. The loss is calculated from the difference in the mass-averaged total pressure from the inlet to the exit of the turbine control volume. The figure shows that the presence of combustor turbulence causes the loss of the turbine cascade to rise by 47%.

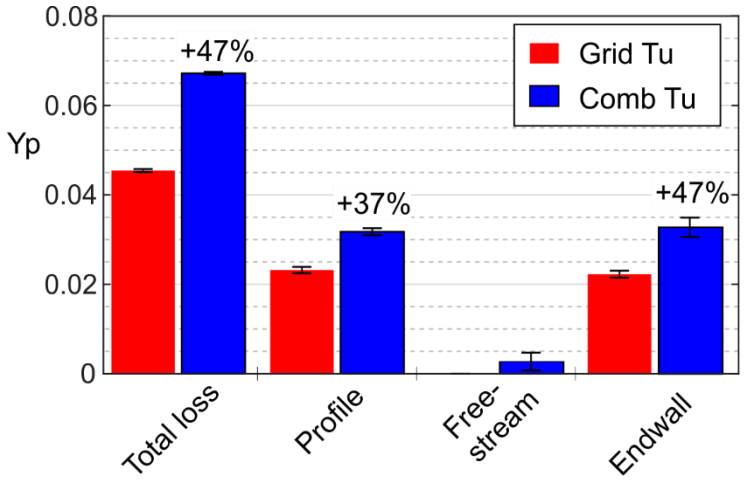

Figure 8.1: Measured loss on a turbine cascade in grid and combustor turbulence.

This rise in loss was measured at a Reynolds number of 800,000. This is similar to the 50% rise in loss measured on a very different design of vane at a Reynolds number of 1,000,000 by Chowdhury et al. (2011). This implies that this large increase in loss is not specific to the blade studied.

Table 8.1: Measured stagnation pressure loss coefficient in grid and combustor turbulence.

	Grid Tu	**Comb Tu**
Profile Loss	0.0232	0.0318
Freestream Loss	0.0000	0.0047
Endwall Loss	0.0223	0.0307
Total Loss	**0.0454**	**0.0672**

Figure 8.1 and Table 8.1 include a breakdown of the total loss into profile loss, freestream loss and endwall loss. The method by which the loss is decomposed is discussed in the following section. It is, however, interesting to observe that the presence of combustor turbulence raises the profile loss and endwall loss by 37% and 47%, respectively. In addition, the presence of combustor turbulence is found to cause a non-zero freestream loss. The physical cause of this will be discussed in the following sections. The rest of this chapter will focus on the individual loss mechanisms and will identify the impact of combustor turbulence on them.

8.1 Profile Loss

Figure 8.1 shows that combustor turbulence causes a 37% rise in profiles loss. The aim of this section is to show the development and physical cause of this increase.

8.1.1 Suction Surface Loss

A hot wire was used to measure the aft portion of the suction surface boundary layer to examine the suction surface loss. Figure 8.2 shows the development of loss along the rear of the suction surface measured using a hot-wire boundary layer probe. The measurements at the trailing edge are presented in Table 8.2.

In Figure 8.2 and Table 8.2, the mass averaged loss coefficient was calculated from measurements of the blade energy thickness and static pressure coefficient, Equation 8.1.

$$Y_p = \frac{\delta_e}{\sigma \cos\alpha_2} C_p^{3/2} \tag{8.1}$$

Table 8.2: Boundary layer measurements at the trailing edge of the airfoil.

		Y_p^{MA}	Y_p^{MIX}	H_{12}	H_{23}	θ_{te}/t	Re_θ
Grid Tu		0.0161	0.0200	1.560	0.589	0.479	2,785
Comb Tu	Measurement 1	0.0234	0.0282	1.507	0.581	0.636	4,111
	Measurement 2	0.0231	0.0277	1.521	0.582	0.636	4,108
	Measurement 3	0.0225	0.0269	1.522	0.586	0.590	3,898
	Average	0.0230	0.0276	1.517	0.583	0.621	4,039
Difference		**+42.9%**	**+38%**	**-3%**	**-1%**	**+30%**	**+45%**

A comparison of the blue and red points in Figure 8.2 shows the impact of combustor turbulence on the development of loss. At the trailing edge, the presence of combustor turbulence raises the suction surface loss by 43%.

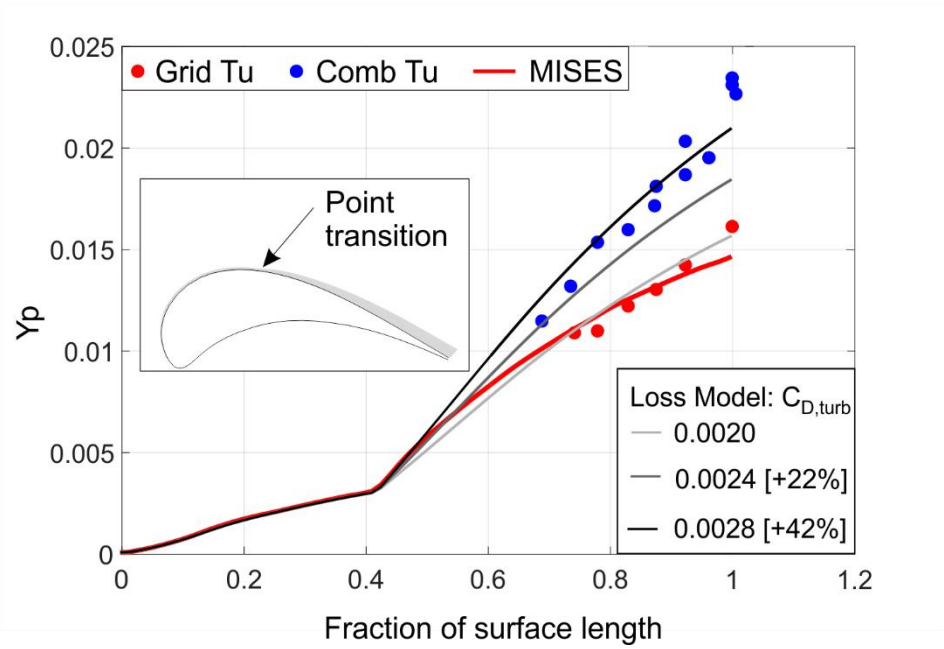

Figure 8.2: Measured and calculated loss on the airfoil suction surface.

To determine the shape of the development of loss for the grid turbulence case, MISES was used (Drela and Youngren, 1998). The code is a coupled Euler-boundary layer solver. The MISES prediction is shown in Figure 8.2 as a red line. A comparison of the red points and red line shows that the two are in good agreement. This indicates that for the grid turbulence case the transition point is at 42% surface length.

To help interpret the effect of changing dissipation coefficient on profile loss, a simple loss model was developed. The loss at each point on the surface was calculated using Equation 8.2.

$$Y_p = \frac{2}{\sigma \cos\alpha_2} \int_0^{L_{ss}} C_D (C_p)^{3/2} d(s) \tag{8.2}$$

In the laminar region of the model, C_D was determined using the laminar correlation given by Denton (1993), Equation 8.3. This correlation stems from the analytical solution for C_D obtained by integrating the laminar Pohlhausen velocity profiles.

$$C_{D,laminar} = \frac{0.173}{Re_\theta} \tag{8.3}$$

The boundary layer momentum thickness in the laminar region was determined from Thwaites' approximate calculation of the laminar boundary layer (White, 2006).

$$\theta^2(x) = \frac{0.45\nu}{U^6} \int_0^x U^5(x) dx \tag{8.4}$$

For the case of combustor turbulence, it proved difficult to determine the exact location of transition. However, as discussed the next section, transition did not seem to move significantly and was therefore fixed in the loss model. Point transition was fixed at 42% surface length (x=0.54Cx). In the turbulent region, C_D was fixed at a number of values. The specific values chosen will be discussed below.

In Figure 8.2, the loss model which most closely fits the red points is a turbulent $C_D = 0.0020$. The agreement between the experimental measurements, MISES, and the loss model is surprisingly good.

In Figure 8.2, the loss model which most closely fits the blue points is a turbulent $C_D = 0.00284$. This value of C_D is 42% higher than the value which matched the grid turbulence data ($C_D = 0.002$). This is surprising, because in the flat plate tests, the presence of grid turbulence was found to raise C_D by only 22%. The loss model with a turbulent $C_D = 0.00244$ represents the case where the C_D is raised by 22%.

In conclusion, the combustor turbulence causes a much larger increase in C_D on the suction surface of the blade than on the flat plate (42% compared to 22%). The cause of this rise will be discussed in a following section.

8.1.2 Boundary layer transition

It is well known that freestream turbulence causes early onset of boundary layer transition (e.g. Abu Ghannam and Shaw, 1980). Therefore it was surprising that the measured suction surface loss, discussed in the previous section, suggested that the transition point was unaffected by combustor turbulence. Additional measurements were taken to investigate the transition location.

The MISES predicted boundary layer transition occurred at an axial location x=0.54Cx (42% of the surface distance). This location, marked on Figure 8.3, coincides with a slight adverse pressure gradient. To determine how much of the suction surface was laminar, the state of the boundary layer at a few points was established by 'listening' with a hot wire ahead of the nominal transition location.

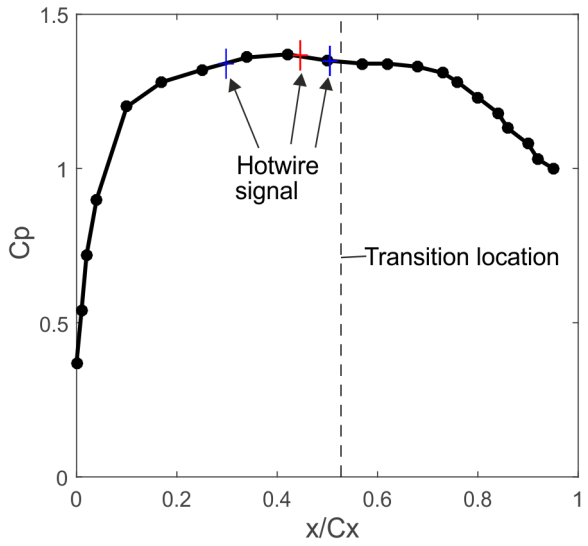

Figure 8.3: Airfoil loading distribution with marks indicating additional hot wire measurements in combustor turbulence (blue) and grid turbulence (red).

Velocity spectra upstream and downstream of the transition location were compared both in grid and combustor turbulence. The turbulence spectra were used to quantify the amount of noise in the boundary layer (hence 'listening' to the state of the boundary layer). Figure 8.4 compares the velocity spectra in the boundary layer at the trailing edge and further upstream. The left hand side of the figure shows measurements in grid turbulence, where the upstream point was measured at x=0.45Cx. The right hand side of the figure shows measurements in combustor turbulence, where the upstream points were measured at x=0.3Cx and x=0.5Cx.

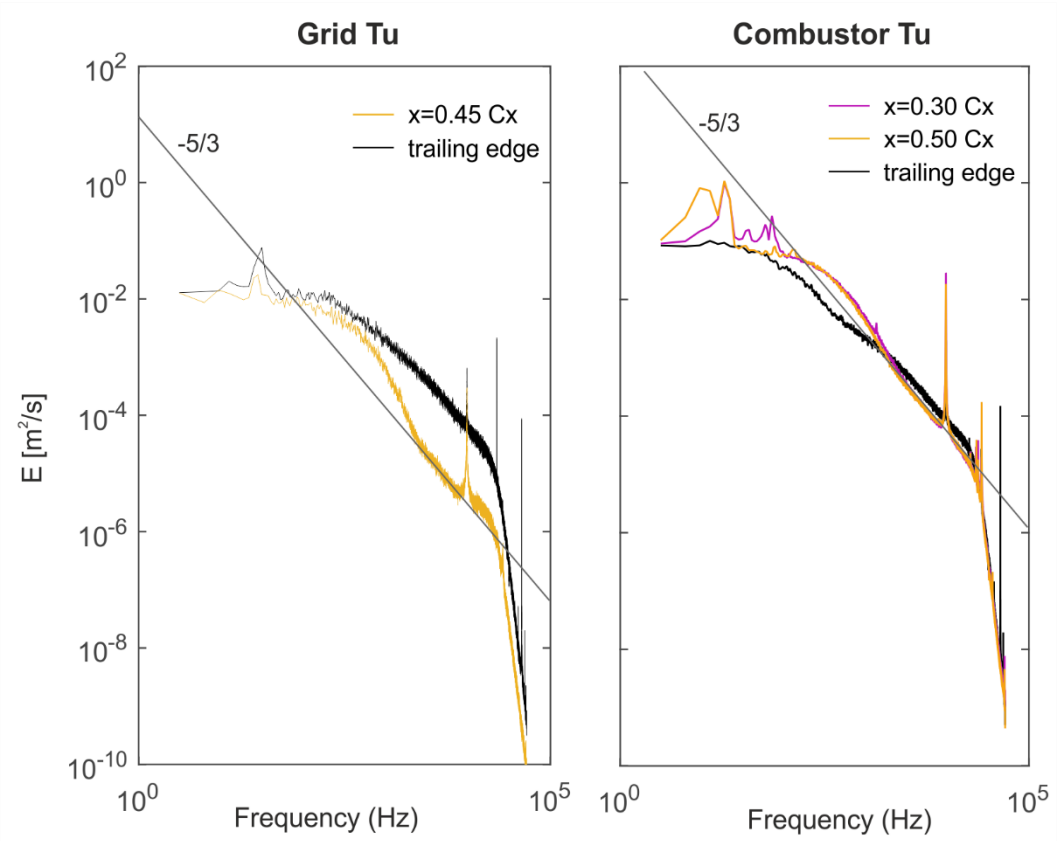

Figure 8.4: Measured velocity spectra on the blade suction surface.

The spectra at the trailing edge is shown in black in both grid and combustor turbulence. In grid turbulence, the spectrum at x=0.45Cx, where the boundary layer is believed to be laminar, clearly has a different shape than at the trailing edge, where the boundary layer is fully turbulent. At low frequencies, the x=0.45Cx spectrum deviates above the $-5/3$ slope, while the trailing edge spectrum deviates below this slope. A similar behavior was observed in a fully laminar and a fully turbulent boundary layer on a flat plate in low turbulence. In combustor turbulence, the spectra at x=0.3Cx and x=0.5Cx are almost identical in shape and different than the spectrum at the trailing edge. As in the laminar case, the upstream spectra deviate above the $-5/3$ slope at higher frequencies.

The shape of the velocity spectra and the behavior of the boundary layer growth indicated that the early suction surface boundary layer was laminar in combustor turbulence. This is not surprising given the strong acceleration over the front of the blade. It was concluded that the transition location was most likely set by the pressure gradient, and freestream turbulence did not affect the transition location.

8.1.3 Trailing edge loss

Figure 8.5 shows total pressure loss coefficient, measured with a five hole probe, at the midspan exit of the turbine cascade control volume. The mass averaged and mixed out values are tabulated in Table 8.3.

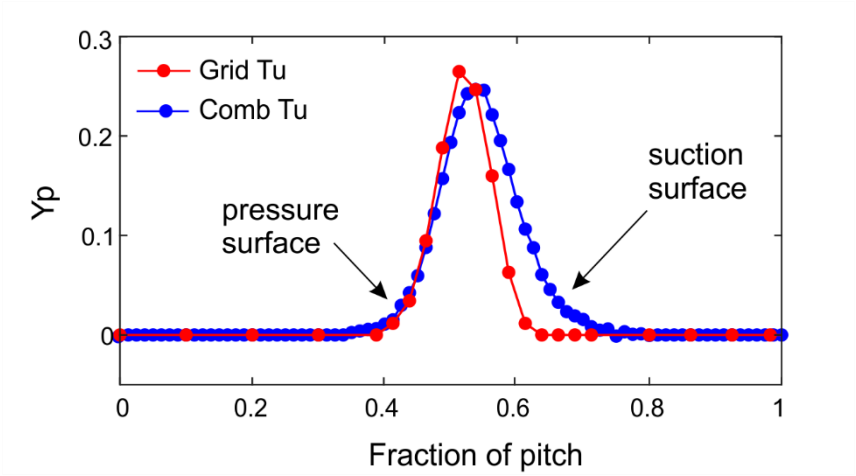

Figure 8.5: Measured loss coefficient at midspan exit of turbine cascade.

The wake shown in Figure 8.5 is similar between the two turbulence cases on the pressure side of the airfoil but is significantly wider on the suction side. This indicates that the suction surface was most affected by combustor turbulence.

Table 8.3: Measured loss coefficient at midspan exit of turbine cascade.

	Y_p^{MA}	Y_p^{MIX}
Grid Tu	0.0232	0.0249
Comb Tu	0.0318	0.0348
Difference	**+37%**	**+39.7%**

Figure 8.6 shows the development of loss downstream of the cascade trailing edge. Just downstream of the trailing edge (x=1.03Cx), the presence of combustor turbulence raises the loss by 40%. This is close to the increase in suction surface loss of 43% shown in the previous section. At the exit of the turbine cascade control volume (solid triangles, x=1.21Cx), the presence of combustor turbulence raises the mass-averaged loss by 37% and the mixed out loss by 40%.

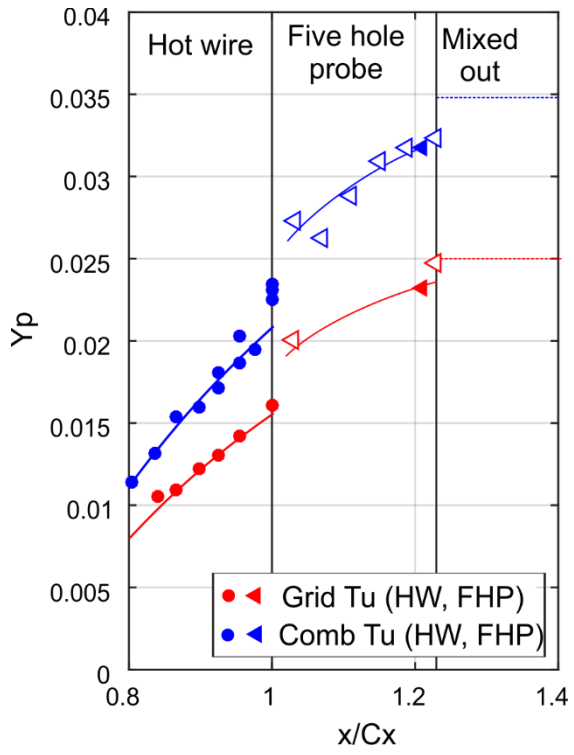

Figure 8.6: Development of midspan loss coefficient just upstream and downstream of the blade trailing edge.

8.1.4 Physical mechanism

This section will discuss the physical mechanism which causes an increase in the dissipation coefficient of the boundary layer on the blade surface. The power spectra of turbulent kinetic energy, measured at the trailing edge, are shown in Figure 8.7. The figure should be compared with Figure 7.7 from Chapter 7.

First, compare the freestream for the case of combustor turbulence in Figure 7.7 (right hand side) and Figure 8.8 (right hand side). In the cascade case, the freestream power spectrum is much lower than in the flat plate case. This is due to acceleration of the freestream in the cascade, which decreases the streamwise fluctuations and reduces the turbulence intensity to 4% at the trailing edge.

Second, compare the boundary layers for the case of combustor turbulence in Figure 7.7 (right hand side) and Figure 8.8 (right hand side). In the cascade case, the maximum magnitude of the power spectrum is more than twice that on the flat plate case. This shows that in the cascade case, the boundary layers have much higher levels of turbulent kinetic energy production than in the flat plate case. The rise in kinetic energy production is responsible for

the larger than expected increase in the C_D (42% for the cascade compared to 22% for the flat plate). The rise in turbulent kinetic energy production is caused by diffusion of the boundary layer. A similar behavior can be observed in the case of grid turbulence by comparing the boundary layer for the case of grid turbulence in Figure 7.7 (left hand side) and Figure 8.8 (left hand side).

It might seem surprising that the impact on the boundary layer is large in the combustor turbulence case despite the freestream turbulence intensity dropping close to the trailing edge. The reason is that the combustor turbulence penetrates the boundary layer earlier on the blade surface and remains in the boundary layer. This turbulent kinetic energy then convects downstream towards the trailing edge. Boundary layer diffusion then results in the sharp rise in the turbulent production.

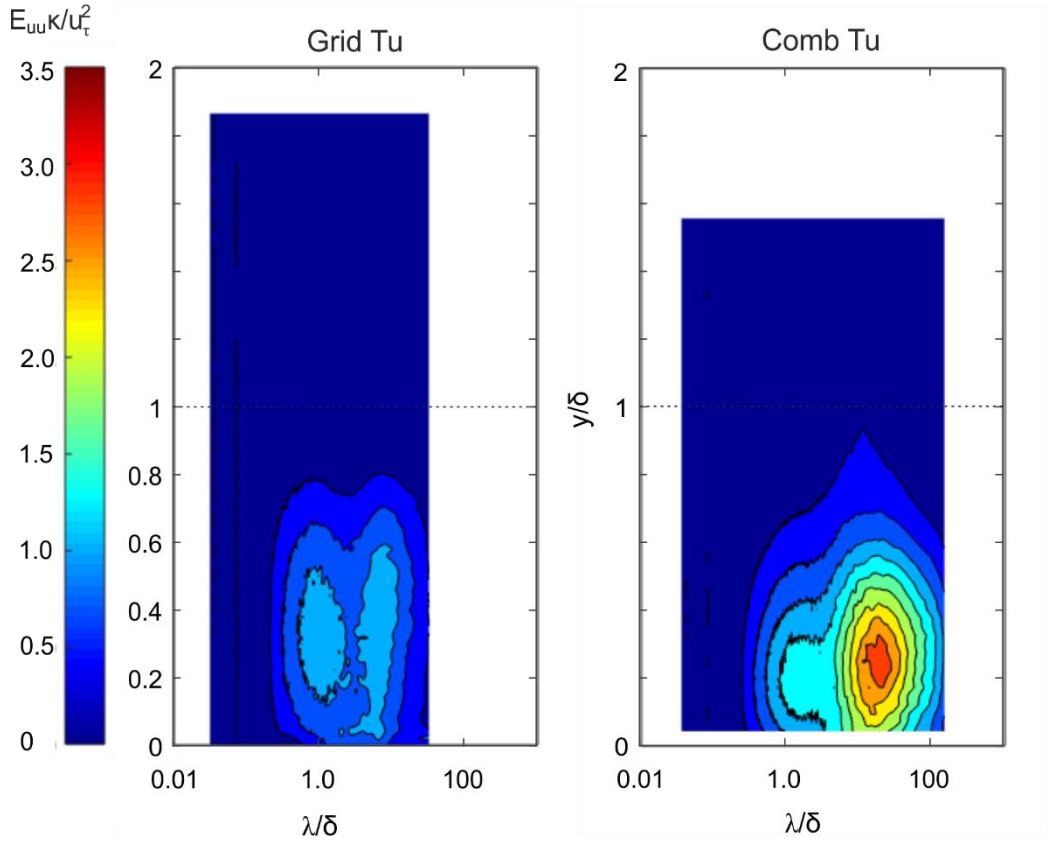

Figure 8.7: Contour maps of inner normalised, pre-multiplied energy spectra of streamwise fluctuating velocity in grid (left) and combustor (right) turbulence measured on airfoil.

In conclusion, the 42% rise in C_D in the turbulent boundary on the suction surface is caused by the combined effects of combustor turbulence penetrating deep into the boundary layer and the subsequent diffusion of that boundary layer. This area of research requires further study,

but this finding implies that the presence of combustor turbulence will more severely penalize high lift designs of turbine blade.

8.2 Freestream loss

Freestream loss is defined as the change in the total pressure, in the midspan freestream region, between the inlet and exit of the turbine cascade control volume. The measured total pressure at each plane was mass-averaged only over the freestream region. For the grid turbulence and combustor turbulence cases, the freestream loss coefficients are 0% and 0.27%, respectively. The uncertainty in this loss measurement is high, ±0.2%. This is because demarcating the freestream is difficult in the case of combustor turbulence.

Chapter 5 showed that there are three possible causes of freestream loss: mixing out of mean velocity gradients, converting the mean kinetic energy into turbulent kinetic energy, and a difference in flow work. The rest of this section will estimate the magnitude of each source and comment on the overall loss.

$$\dot{m}\Delta\left[\frac{P_0}{\rho}\right] = -\int_{\mathcal{V}}\left[\nu\left(\frac{\partial U_i}{\partial x_j}+\frac{\partial U_j}{\partial x_i}\right)\frac{\partial U_i}{\partial x_j}\right]d\mathcal{V} - \int_{\mathcal{V}}\left[\left(-\overline{u_i u_j}\right)\frac{\partial U_i}{\partial x_j}\right]d\mathcal{V} - \dot{m}\Delta\left[\overline{u^2}\right] \qquad (8.5)$$

The three terms on the right hand side of the equation show possible sources of freestream loss. The first term on the right hand side represents the dissipation of mean field kinetic energy caused by the mixing out of velocity gradients. When combustor turbulence is generated, it is impossible to create a flow which does not have a velocity variation in the mean flow field. An upper bound on the magnitude of this term can be estimated by mixing out the mean field velocity variation at the inlet to the turbine cascade control volume. This gives a negligible change in loss coefficient of 0.01%.

Next, consider the conversion of mean field kinetic energy into turbulent kinetic energy. The incoming turbulent vorticity is stretched by the mean strain. This transfers energy from the streamwise to the lateral components of turbulent kinetic energy. Overall, as the flow is accelerated through the cascade, this causes a rise in turbulence production. Rapid distortion theory (Batchelor, 1953, p.74) predicts a 10% increase in turbulent kinetic energy due to the acceleration, shown in Figure 8.8. The rise in turbulent kinetic energy is accompanied by a loss of mean kinetic energy. This term gives a change in loss coefficient of +0.12%.

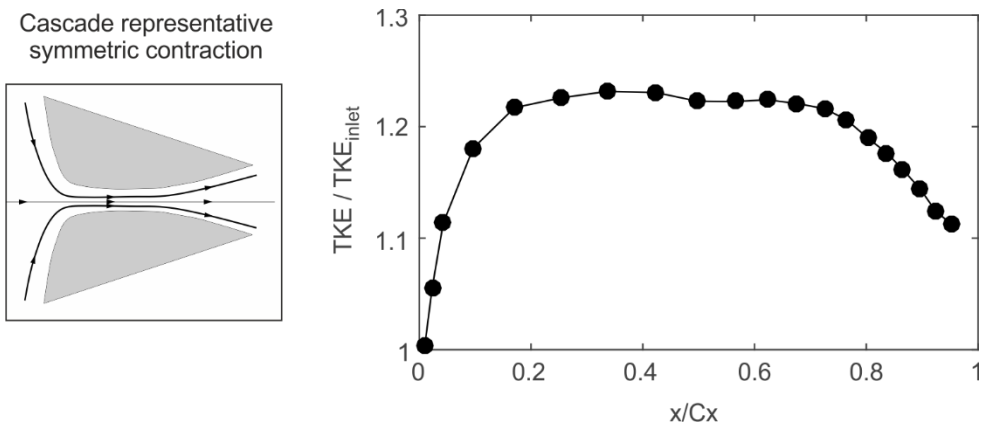

Figure 8.8: Inviscid development of turbulent kinetic energy through the cascase.

Finally, consider the difference in the 'flow work' on the inlet and exit planes by the turbulent pressure (the isotropic Reynolds stress terms). These Reynolds stress terms are analogous to an additional pressure term acting on the inlet and exit of the control volume. The magnitude of the 'flow work' done by these terms can be estimated using the measured turbulent kinetic energy at the inlet and exit of the turbine cascade control volume. This gives a change in loss coefficient of -0.32%. The negative sign is due to the 'flow work' into the control volume being higher than out of the control volume.

The sum of these three terms gives a total freestream loss coefficient of -0.2%. This contrasts to the measured freestream loss coefficient of +0.27% shown. The cause of this difference is not understood and requires further study. However, the next section will show that a likely cause of this is due to combustor turbulence mixing boundary layer loss far into the freestream. This causes a difficulty in precisely defining the freestream.

Though the cause of the positive freestream loss coefficient is not understood, it is important for this study to note that the size of the freestream loss is small compared to the changes in profile and endwall losses which are being measured.

8.3 Endwall loss

The endwall loss is calculated by subtracting the profile and freestream losses from the total loss. Figure 8.1 shows that the presence of combustion turbulence causes the endwall loss to rise by 47%. The rise in endwall loss due to the presence of combustor turbulence could have two possible causes: a rise in the strength of the endwall secondary flow, or a rise in the

dissipation associated with the endwall secondary flow (but with the strength of the flow unchanged).

8.3.1 Secondary flows

Coull (2019) found that for a wide range of turbine designs, with the same inlet boundary layer, the magnitude of the endwall loss could be correlated with the strength of the secondary flow. In the two cases considered in this thesis, the inlet boundary layers are relatively similar. The inlet boundary layer thicknesses are 6.3% and 8% of span for the grid and combustor case. The shape factors (H_{12} and H_{13}) are 1.35 and 1.27, respectively. Any significant change in strength of the endwall secondary flow must therefore be due to the presence of combustor turbulence.

To investigate the influence of combustor turbulence on the strength of the secondary flow, traverses were measured at four axial locations within the blade passage. Figure 8.9 shows contours of loss coefficient and secondary velocity vectors for both the case with grid turbulence and the case with combustor turbulence. The horizontal axis begins at the blade suction surface and is normalized by the blade to blade pitch (230mm). The area of the passage is shown explicitly in the first subplot, where a solid line marks the pressure surface of the adjacent blade.

The relative strength of the secondary flow can be gauged by comparing the penetration depth of the suction surface separation line at each axial location. It can be seen that the penetration depths in the two cases are very similar. By 87% of axial chord (x=0.87 Cx), the penetration depth of the suction surface separation line, for the case with combustor turbulence, is 2% of the span further from the endwall.

The strength of the secondary flow can be determined by integrating the secondary kinetic energy on each traverse plane. A comparison of the two cases is shown in Figure 8.10. Once again, the presence of combustor turbulence can be seen to have only a small effect on the strength of the secondary flow. The cause of the rise in endwall loss must therefore be due to a rise in dissipation in the endwall region.

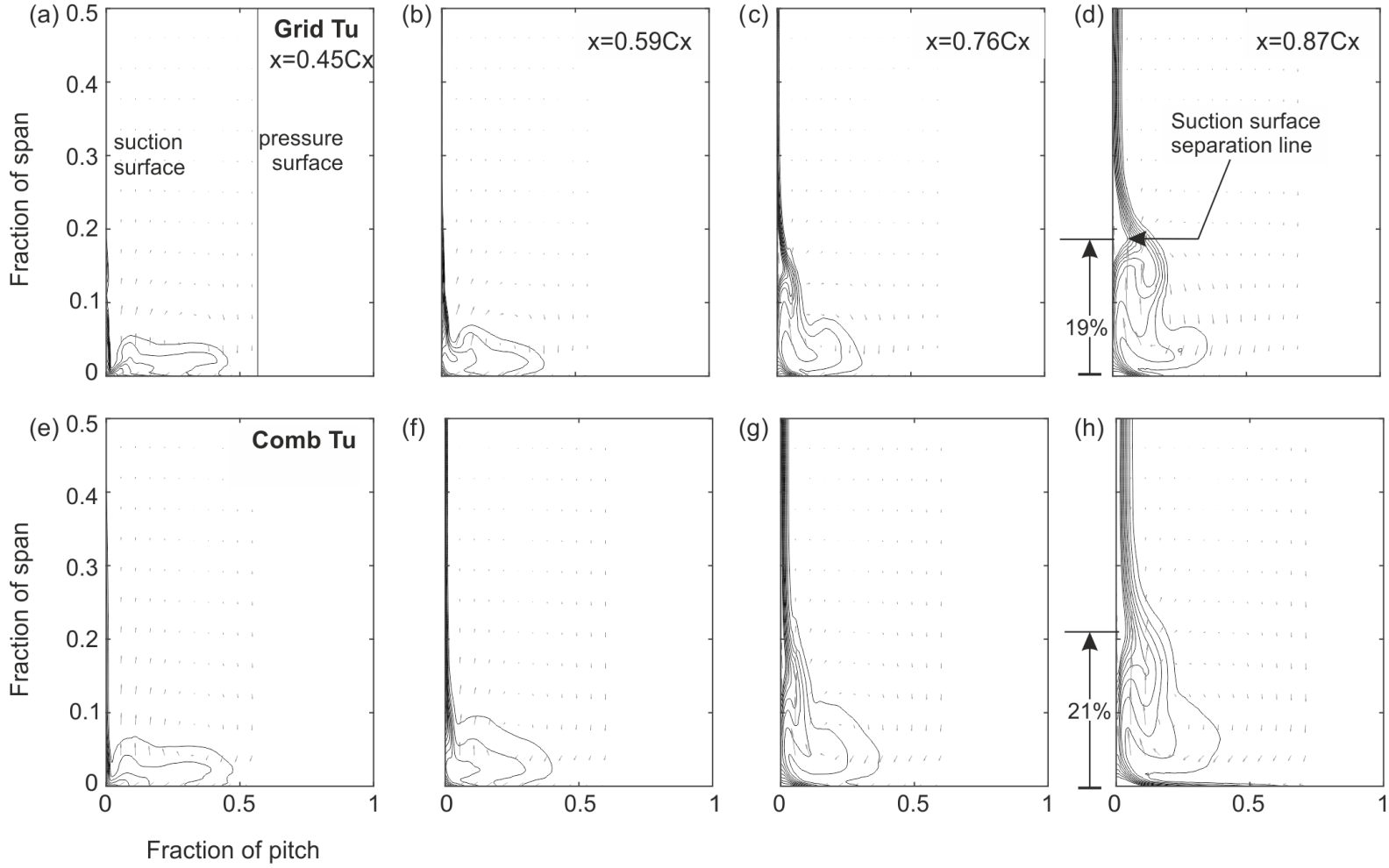

Figure 8.9: Contours of loss coefficient at four axial locations within the turbine cascade. First row is grid turbulence and second row is combustor turbulence. Contour intervals are 5% of exit dynamic head.

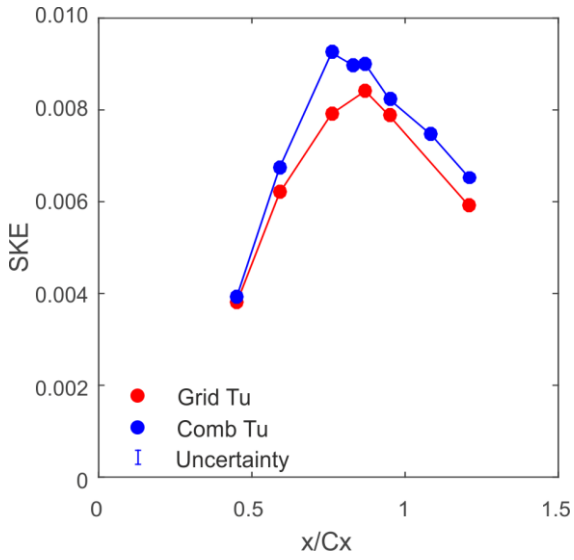

Figure 8.10: Mass averaged non-dimensional secondary kinetic energy in the cascade.

8.3.2 Endwall dissipation

To determine the region of endwall in which this rise in dissipation occurs, the difference in the loss coefficient between the combustor turbulence case and grid turbulence case at 0.87Cx is plotted in Figure 8.11. Red regions show where the combustor turbulence case has higher loss, while blue denotes regions where the grid turbulence case has higher loss.

Figure 8.11 shows that combustor turbulence has higher loss in three regions of the endwall flow. The first region is a thicker endwall boundary layer. This region shows a large rise in loss coefficient, but the mass flow associated with the region is small; therefore, the contribution of this region to the rise in endwall loss is small. The second region is a rise in loss coefficient associated with the endwall loss core. In this region, both the rise in loss coefficient and the mass flow are large, resulting in a significant contribution to the rise in endwall loss. The third region is the rise in loss in the freestream. The rise in loss coefficient in this region is relatively small, but the mass flow associated with it is very large. The contribution of this region to the rise in endwall loss is correspondingly significant.

This last region, the rise in loss in the freestream, is interesting. It implies that combustor turbulence mixes boundary layer fluid far into the freestream. This explains the difficulty in extracting the freestream loss discussed previously.

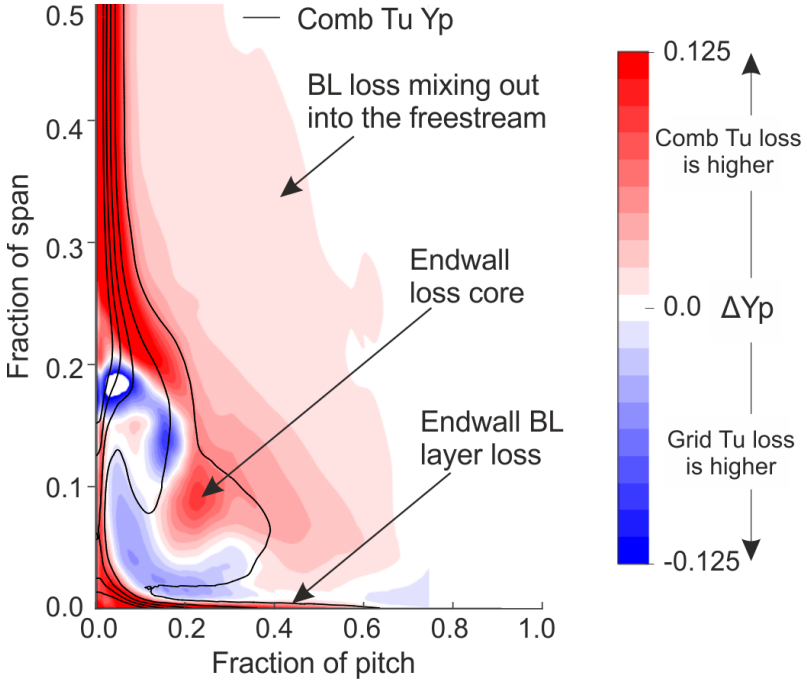

Figure 8.11: Change in loss coefficient due to combustor turbulence at 0.87Cx.

We are now in a position to give a probable cause of the rise in endwall loss. Conventionally, endwall loss is considered to correlate with the strength of the secondary flow. In the case of combustor turbulence, the secondary flow strength is unchanged but endwall loss rises. To understand why, the loss mechanism responsible for endwall loss must be understood. The secondary flow itself is an inviscid phenomenon, resulting from the turning and stretching of vorticity in the inlet boundary layer. Very little of the endwall loss is a direct result of the dissipation of this secondary kinetic energy. Instead endwall loss is largely the result of the secondary flow sweeping the boundary layer off of the blade and endwall surfaces and being replaced by a new boundary layer.

Therefore, a possible explanation of the rise in endwall loss is that, for a fixed strength of secondary flow, the endwall loss scales with the dissipation coefficient of the boundary layer which is being swept off the blade and endwall surfaces. This would explain why the percentage rise in the endwall loss (+47%) is of a similar magnitude to the rise in profile loss (+37%). It should, however, be noted that without measuring the local dissipation coefficient throughout the endwall boundary layer and the freestream, this conclusion cannot be verified.

8.4 Conclusions

The presence of combustor turbulence increases the total pressure loss downstream of a blade row by 47%. The increase in profile loss is 37%, the increase in endwall loss is 47%, and there is an additional freestream loss which is not present in grid turbulence.

The rise in boundary layer dissipation coefficient was measured to be significantly larger in a cascade (+42%) than the rise measured on a flat plate (+22%). This is thought to be due to larger turbulent kinetic energy production in a diffusing boundary layer, but this hypothesis requires more investigation.

The strength of the secondary flow in combustor turbulence is unchanged. Instead, endwall loss is largely the result of the secondary flow sweeping the boundary layer off of the blade and endwall surfaces and being replaced by a new boundary layer. Endwall loss was found to scale with blade boundary layer loss.

The freestream loss was very small compared to the profile loss and endwall loss and is therefore difficult to measure accurately. Theory says that there should be a slight rise in stagnation pressure in the freestream due to the higher ‘flow work’ into the control volume. Measured stagnation pressure in the freestream, on the other hand, was found to slightly decrease. However, because the combustion turbulence is very effective at mixing loss from the blade surface deeply into the freestream and across most of the passage span, it is difficult to measure freestream loss accurately. Ultimately, its small size means that freestream loss is of secondary importance compared to the other sources of loss.

Chapter 9
Industrial Implications

The measurements presented in Chapters 7 and 8 clearly demonstrate that combustor turbulence fundamentally changes the aerodynamic loss mechanisms in a turbine. This chapter will apply those findings to real gas turbine engines.

9.1 Stage efficiency in high turbulence

It is important to understand the impact of the loss mechanisms discussed in this thesis on the efficiency of a turbine stage mounted downstream of a combustor. Two cases will be considered: a low speed stage, based on the current cascade, and a high speed stage representative of a modern engine.

9.1.1 Harrison repeating stage

For the case of a low speed stage, a 50% reaction stage with identical stator and rotor profiles was assumed. This is similar to the computational study of Denton and Pullan (2012). It was assumed that combustor turbulence affects only the stator row of the turbine stage. Therefore, the increase in loss measured in the cascade blade was applied to the stator row, with the rotor loss left unchanged. The presence of combustor turbulence was found to reduce the stage efficiency by 1.1%.

9.1.2 Engine representative stage

For the case of the engine representative stage, the profile loss of the vane was determined using MISES. Under the presence of combustor turbulence, the transition location was assumed to be unchanged, but the dissipation coefficient in the turbulent region of the boundary layer

was increased by 42%. The baseline endwall loss was deduced from an engine correlation. It was then increased by 38% based on the findings from this research.

It was assumed that the fractional rise in endwall loss was the same as for the low speed blade used in this study. The freestream loss shown in Figure 8.1 was added. The engine cooling losses were assumed unchanged by the presence of combustor turbulence. The presence of combustor turbulence on the vane alone was found to reduce the stage efficiency by 1.3%. The larger reduction in stage efficiency on the engine representative stage, relative to the low speed stage, was due to differences in velocity profile of the blade and the transition location.

The magnitude of this drop in stage efficiency is very large. Some may ask, if the size of this efficiency drop is so large, why has it not been identified in real engines? The reason is twofold. First, the high speed turbine test facilities that are used to measure loss trades do not include combustors turbulence generators and therefore would not exhibit this effect. Second, the hostile environments in real engines make accurate measurement of the efficiency of the high pressure stage impossible. This means that the uncertainty of the efficiency measurement of the real high pressure stage is very high.

9.2 Conclusions

The effect of combustor turbulence on engine performance has been quantified for the first time in literature. The presence of combustor turbulence was found to cause a 1.1% to 1.3% reduction of a turbine stage efficiency. This knowledge can enable better uncertainty predictions in performance modelling.

Chapter 10
Conclusions and Future Work

This thesis has shown that the presence of combustor turbulence is very different in nature to the presence of grid turbulence. By the vane inlet, the combustor turbulence is close to isotropic in nature. The turbulence penetrates deep into the boundary layer. This reduced the shape factor of the boundary layer. The mean shear in the boundary layer acts to stretch the turbulence resulting in a rise in the production of turbulent kinetic energy within the boundary layer. The combined result is that, in a zero pressure gradient, the presence of combustor turbulence causes a rise in dissipation coefficient of 22%.

In a turbine cascade, the presence of combustor turbulence was measured to cause a 47% rise in total loss. This resulted from a 37% rise in profile loss and a 38% rise in endwall loss. When these loss mechanisms were applied to the vane from an engine representative high pressure stage, it was found to result in a 1.3% reduction in stage efficiency. This is an incredibly large number, and it is important that this new mechanism is included in turbine design systems.

Combustor turbulence is an incredibly difficult environment in which to make accurate loss measurements. The aim of this thesis has therefore been to bring certainty to this difficult area of research and to provide a methodology on which future researchers can build. The research also acted to frame a number of important future research questions. How do adverse pressure gradients alter the dissipation coefficient of a turbulent boundary layer? If a turbulence intensity of 4% has no effect on the dissipation coefficient of a turbulent boundary layer, and a turbulence intensity of 10% increases the dissipation coefficient of a turbulent boundary layer by 22%, what is the relationship between dissipation coefficient and turbulence intensity?

Finally, the research has significant implications for design. The type of combustor (lean burn or conventional) is likely to change the nature and intensity of the turbulence entering the high pressure turbine. In addition, it is likely that the loading distribution of the vane will change the impact of combustor turbulence on loss, because the impact of combustor turbulence is highly dependent on the location of transition and the magnitude of the adverse pressure gradient to which the boundary layer is subjected.

References

Abu Ghannam, B.J. and Shaw, R. (1980). Natural Transition of Boundary layers - The Effects of Turbulence, Pressure Gradient and Flow History, *Journal of Mechanical Engineering Science,* 22(5).

Ames, F.E. (1990). *Heat Transfer with High Intensity, Large Scale Turbulence: The Flat Plate Turbulent Boundary Layer and the Cylindrical Stagnation Point.* PhD thesis, Stanford University, Department of Mechanical Engineering, Stanford, CA.

Ames, F.E. (1998). Aspects of vane film cooling with high turbulence, part ii, adiabatic effectiveness. *ASME Journal of Turbomachinery*, 120:768–776.

Ames, F.E. and Plesniak M.W. (1997). The influence of large-scale, high-intensity turbulence on vane aerodynamic losses, wake growth, and the exit turbulence parameters. *ASME Journal of Turbomachinery*, 119(2):182-192.

Barringer, M.D., Richard, O.T., Walter, J.P., Stitzel, S.M., and Thole, K.A. (2002). Flow Field Simulation of a Gas Turbine Combustor. *ASME Journal of Turbomachinery*, 124.

Barringer, M.D., Thole, K.A., and Polanka, M.D. (2004). Developing a Combustor Simulator for Investigating High Pressure Turbine Aerodynamics and Heat Transfer. ASME Paper GT-2004-53613.

Barringer, M.D., Thole, K.A., and Polanka, M.D. (2007). Experimental Evaluation of an Inlet Profile Generator for High-Pressure Turbine Tests. *ASME Journal of Turbomachinery,* 129.

Batchelor, G.K. (1953). *The Theory of Homogenous Turbulence.* Cambridge University Press: Cambridge, UK.

Bendat, J. S. and Piersol, A.G. (1968). *Measurement and Analysis of Random Data*. John Wiley & Sons Inc., New York, NY.

Bicen, A. F., Tse, D., and Whitelaw, J. H. (1988). Flow and Combustion Characteristic of an Annular Combustor. *Combustion and Flame,* 72:175-192.

Bons, J. P. (2002). St and cf augmentation for real turbine roughness with elevated freestream turbulence. *ASME Journal of Turbomachinery*, 124:623–644.

Boyle, R.J., Lucci, B.L., Verhoff, V.G., Camperchioli, W.P., La, H. (1998). Aerodynamics of a Transitioning Turbine Stator over a Range of Reynolds Numbers. *ASME Paper No. 98-GT-285.*

Brunn, H.H. (1995). *Hot-Wire Anemometry – Principles and Signal Analysis*. Oxford University Press: Oxford, UK.

Castro, I.P. (1984). Effects of Freestream Turbulence on Low Reynolds Number Boundary Layers. *Journal of Fluids Engineering,* 106(3): 298-306.

Cebici, T., and Bradshaw, P. (1984). *Physical and Computational Aspects of Convective Heat Transfer*. Springer-Verlag: New York, NY.

Cha, C.M., Hong, S., Ireland, P.T., Denman, P., and Savarianandam, V. (2012a). Turbulence levels are high at the combustor-turbine interface. ASME Paper No. GT2012-69130.

Cha, C.M., Hong, S., Ireland, P.T., Denman, P., Savarianandam, V. (2012b). Experiments and Numerical Investigations of Combustor-Turbine Interaction Using an Isothermal, Nonreacting Tracer. *Journal of Engineering for Gas Turbines and Power,* 134.

Chowdhury, N.H.K., Dey, P.K., and Ames, F.E. (2011). The influence of inlet contraction on vane aerodynamic losses and secondary flows with variable turbulence and Reynolds number. ASME Paper No. GT2011-45737.

Coull, J.D. (2018). Private communication.

Coull, J.D. and Hodson, H. (2012). H.P., Blade Loading and its Application in the Mean-Line Design of the Low Pressure Turbine. *ASME Journal of Turbomachinery,* 135(2).

Cox, R.N. (1957). Wall Neighborhood Measurements in Turbulent boundary Layers using a Hot Wire Anemometer, Aeronautics Research Council Report ARC 19101, FM 2511.

Cresci, I., Ireland, P. T., Bacic, M., Tibbott, I., and Rawlinson, A., (2015). Realistic Velocity and Turbulence Intensity Profiles at the Combustor-Turbine Interface (CTI) Plane in a Nozzle Guide Vane Test Facility. Proceedings of at the 11th European Conference on Turbomachinery Fluid Dynamics and Thermodynamics, Madrid, Spain.

Davidson, P.A. (2015). *Turbulence – An Introduction for Scientists and Engineers*. Oxford, UK: Oxford University Press.

Denman, P. (2016). Email message to author, January 29, 2016, Loughborough, UK.

Denton, J. D. (1993). The 1993 IGTI scholar lecture: Loss Mechanisms in Turbomachines. *ASME Journal of Turbomachinery*, 115(4):621–656.

Dogan, E. (2017). *Effects of Large-Scale Free-Stream Turbulence on a Zero-Pressure-Gradient Turbulent Boundary Layer.* PhD thesis, University of Southampton Faculty of Engineering and the Environment, Southampton, UK.

Dogan, E., Hanson, R.E., Ganapathisubramani, B. (2016). Interactions of Large-Scale Free-Stream Turbulence with Turbulent Boundary Layers. *Journal of Fluid Mechanics*, 802:79-107.

Drela, M. and Youngren, H. (1998). *A User's Guide to MISES 2.53.*

Esteban, L.B., Dogan, E., Rodríguez-López, E., Ganapathisubramani, B. (2017). Skin Friction Measurements in a Turbulent Boundary Layer under the Influence of Freestream Turbulence." *Experiments in Fluids*, 58:115.

Flegel, A.B., Giel, P.W., and Welch, G.E. (2014). Aerodynamic Effects of High Turbulence Intensity on a Variable-Speed-Power-Turbine Blade with Large Incidence and Reynolds Number Variation. NASA TM-2014,218137.

Gregory-Smith, D. G., Graves, C. P., and Walsh, J. A. (1988). Growth of secondary losses and vorticity in an axial turbine cascade. *ASME Journal of Turbomachinery*, 110(1):1-8.

Greitzer, E.M., Tan, C.S., and Graf, M.B. (2004). *Internal Flow - Concepts and Applications.* Cambridge, UK: Cambridge University Press.

Grewe, R.P. (2013). *The Effect of Endwall Manufacturing Variations on Turbine Performance.* PhD thesis. Cambridge University, Department of Engineering Cambridge, UK.

Haldeman, C.W. et al. (2008). Aerodynamic and Heat Flux Measurements in a Single-Stage Fully Cooled Turbine – Part I: Experimental Approach. *ASME Journal of Turbomachinery,* (130).

Hancock, P.E. and Bradshaw, P. (1983). The Effect of Free-Stream Turbulence on Turbulent Boundary Layers. *Journal of Fluids Engineering,* 105(3):284-289.

Harrison, S. (1989). *The Influence of Blade Stacking on Turbine Loss*. PhD thesis, Cambridge University, Department of Engineering, Cambridge, UK.

Hearst, R.J. (2015). *Fractal, Classic, and Active Grid Turbulence: From Production to Decay*. PhD thesis, University of Toronto, Department of the Institute for Aerospace Studies, Toronto, Canada.

Hearst, R.J. and Lavoie, P. (2012). A Parametric Study of High Reynolds Number Grid Generated Turbulence. In *42nd AIAA Fluid Dynamics Conference and Exhibit*, page 2852. American Institute of Aeronautics and Astronautics.

Hinze, J.O. (1975). *Turbulence.* New York, NY: McGraw Hill.

Holdeman, J.D. (1991). Mixing of Multiple Jets with a Confined Subsonic Crossflow. NASA TM 104412.

Hutchings, N. and Marusic, I. (2007). Large-scale Influences in Near Wall Turbulence. *Philosophical Transactions of the Royal Society*, 365:647-644.

Kays, W.M. and Crawford, M.E. (1980). *Convective Heat and Mass Transfer.* New York, NY: McGraw-Hill

Kingery, J.A., and Ames, F.E. (2016). Stagnation Region Heat Transfer Augmentation at Very High Turbulence Levels. *ASME Journal of Turbomachinery,* 138(8).

Koutmos, P. and McGuirk, J. J. (1989). Isothermal Flow in a Gas Turbine Combustor – A Benchmark Experimental Study. *Experiments in Fluids*, 7:344-354.

Lefebvre, A.H. (1999). *Gas Turbine Combustion*. New York, NY: Taylor and Francis Group.

Marek, C.J. (1984). Combustor Turbulence. *Transition in Turbines*. NASA Conference Publication 2386.

Mehendale, A.B., and Han, J.C. (1990). Influence of High Mainstream Turbulence on Leading Edge Film Cooling Heat Transfer. *ASME Journal of Turbomachinery*, 114(4).

McEligot, D.M., Walsh, E. J., Laurien, E. and Wolf, J.R. (2006). Entropy Generation In the Viscous Layer of a Turbulent Channel Flow. 5th International Symposium on Turbulence, Heat and Mass Transfer, Idaho Falls, Idaho, USA.

Moss, R. W., and Oldfield, M.L.G. (1991). Measurements of Hot Combustor Turbulence Spectra. ASME paper 91-GT-351.

Österlund, J. M. (1999). *Experimental studies of zero pressure-gradient turbulent boundary layer flow.* PhD thesis, Royal Institute of Technology, Department of Mechanics, Stockholm,Sweden.

Roach, P. E. (1987). The Generation of Nearly Isotropic Turbulence by Means of Grids. *International Journal of Heat and Fluid Flow*, 8(2):82-92.

Roberts, Q.D., and Denton, J.D. (1996). Loss Production in the Wake of a Simulated Subsonic Turbine Blade. ASME paper 96-GT-421.

Rodríguez-López, E., Bruce, P.J.K., Buxton, O.R.H. (2015). A Robust Post-Processing Method to Determine Skin Friction in Turbulent Boundary Layers from the Velocity Profile. *Experiments in Fluids*, 56(4):68.

Rolls-Royce, (2005). *The Jet Engine*. Chichester, UK: John Wiley & Sons.

Sagrado, A.G. (2007). *Boundary Layer and Trailing Edge Noise Sources*. PhD Thesis. Cambridge University, Department of Engineering, Cambridge, UK.

Schlatter, P. and Örlu, R. (2010). Assessment of Direct Numerical Simulation Data of Turbulent Boundary Layers. *Journal of Fluid Mechanics*, 659:116-126.

Schlichting, H. and Kestin, J. (1968). *Boundary Layer Theory.* New York, NY: McGraw-Hill.

Schroll, M. et al. (2017). Flow Field Characterization at the Outlet of a Lean Burn Single-Sector Combustor by Laser-Optical Methods. *Journal of Engineering for Gas Turbines Power,* 131(1).

Sharp, N., Neuscamman, S., and Warhaft, Z. (2009). Effects of Large-Scale Freestream Turbulence on a Turbulent Boundary Layer. *Physics of Fluids*, 21(9).

Stefes, B. and Fernholz, H.-H. (2004). Skin Friction and Turbulence Measurements in a Boundary Layer with Zero-Pressure-Gradient under the Influence of High Intensity Free-Stream Turbulence. *European Journal of Mechanics - B/Fluids*, 23(2):303-318.

Stieger, R.D., and Hodson, H.P. (2003). Unsteady Dissipation Measurements on a Flat Plate Subject to Wake Passing. *Proceedings of the Institution of Mechanical Engineers Part A Journal of Power and Energy* 217(4):413-419.

Telionis, D. P. (1979). Review – Unsteady Boundary Layers, Separated and Attached." *Journal of Fluids Engineering,* 101(1).

Tennekes, H., and Lumley, J.L. (1994). *A First Course in Turbulence*. Cambridge, MA: MIT Press.

Thole, K.A. (1992). *High Freestream Turbulence Effects on Turbulent Boundary* Layers, PhD Thesis, University of Texas, Turbulence and Turbine Cooling Research Laboratory, Austin, TX.

Thole K. A., Bogard D. G., and Whan-Tong, J. L. (1994). Generating High Freestream Turbulence Levels, *Experiments in Fluids*, Vol. 17:375-380.

Thole, K. A. and Bogard, D. G. (1996). High Freestream Turbulence Effects on Turbulent Boundary Layers. *Journal of Fluids Engineering*, 118:276-284.

Van Fossen, G.J., Simoneau, R.J., and Ching, C.Y. (1994). Influence of Turbulence Parameters, Reynolds Numbers, and Body Shape on Stagnation Region Heat Transfer. NASA Technical Paper 3487.

White, F.M. (2006). *Viscous Fluid Flow.* New York, NY: McGraw Hill.

Zimmerman, D.R. (1979). Laser Anemometer Measurements at the Exit of a T63-C20 Combustor. NASA CR-159623, 1979.

Appendix A
Loss Accounting

Consider a simple steady state case of a control volume with no body forces or internal heat sources and with no shear work on the outer surface of the control volume and no heat transfer across the surface. The flow is incompressible. In this case, the stagnation enthalpy of the flow is constant.

$$\frac{D}{Dt}\left(h + \frac{U_i U_i}{2}\right) = 0 \tag{A.1}$$

The rate of change of mechanical energy is given by:

$$\frac{D}{Dt}\left(\frac{U_i U_i}{2}\right) = -\frac{1}{\rho} U_i \frac{\partial P}{\partial x_j} + \frac{1}{\rho} U_i \frac{\partial \tau_{ij}}{\partial x_j} \tag{A.2}$$

Where the shear stress tensor is defined by:

$$\tau_{ij} = \mu\left(\frac{\partial U_i}{\partial x_j} - \frac{\partial U_j}{\partial x_i}\right) \tag{A.3}$$

Equation A.2 can be re-written as:

$$\frac{D}{Dt}\left(\frac{U_i U_i}{2}\right) = -\frac{1}{\rho} U_i \frac{\partial P}{\partial x_j} + \frac{1}{\rho}\frac{\partial}{\partial x_j}\left(U_i \tau_{ij}\right) - \frac{1}{\rho}\tau_{ij}\frac{\partial U_i}{\partial x_j} \tag{A.4}$$

The last term on the right hand side is the dissipation function:

$$\Phi = \tau_{ij}\frac{\partial U_i}{\partial x_j} = \mu\left(\frac{\partial U_i}{\partial x_j} - \frac{\partial U_j}{\partial x_i}\right)\frac{\partial U_i}{\partial x_j} \tag{A.5}$$

The rate of change of thermal energy is given by:

$$\frac{Dh}{Dt} = \frac{1}{\rho}\frac{DP}{Dt} + \frac{1}{\rho}\tau_{ij}\frac{\partial U_i}{\partial x_j} = \frac{1}{\rho}\frac{DP}{Dt} + \frac{1}{\rho}\Phi \tag{A.6}$$

Using Gibbs relation, the rate of change of entropy is given by:

$$T\frac{Ds}{Dt} = \frac{1}{\rho}\tau_{ij}\frac{\partial U_i}{\partial x_j} = \frac{1}{\rho}\Phi \tag{A.7}$$

For a turbulent flow, we express each quantity as a sum of its mean and fluctuating part.

$$\begin{gathered} U_i = \overline{U}_i + u_i \\ P = \bar{P} + p \\ U_i U_i = \overline{U}_i\overline{U}_i + 2\overline{U}_i u_i + u_i u_i = \overline{U}_i\overline{U}_i + 2\overline{U}_i u_i + q^2 \end{gathered} \tag{A.8}$$

Substitution into the mechanical energy equation, Equation A.2, and averaging with respect to time gives Equation A.9 (Hinze, 1975, pg. 71).

$$\begin{gathered} \overline{\frac{D}{Dt}\left(\frac{(\overline{U}_i + u_i)(\overline{U}_i + u_i)}{2}\right)} = \\ \frac{D}{Dt}\left(\frac{\overline{U}_i\overline{U}_i}{2}\right) + \frac{D}{Dt}\left(\frac{\overline{q^2}}{2}\right) = \\ -\frac{1}{\rho}\overline{U_j}\frac{\partial \bar{P}}{\partial x_j} + \nu\frac{\partial}{\partial x_i}\overline{U_i}\left(\frac{\partial \overline{U_i}}{\partial x_j} + \frac{\partial \overline{U_j}}{\partial x_i}\right) - \frac{\partial}{\partial x_i}\overline{u_i\left(\frac{p}{\rho} + \frac{q^2}{2}\right)} \\ -\frac{\partial}{\partial x_i}\overline{U_i}\overline{u_i\,u_j} - \nu\frac{\partial}{\partial x_i}\overline{u_i\left(\frac{\partial u_i}{\partial x_j} + \frac{\partial u_j}{\partial x_i}\right)} \\ -\nu\left(\frac{\partial \overline{U_i}}{\partial x_j} - \frac{\partial \overline{U_j}}{\partial x_i}\right)\frac{\partial \overline{U_i}}{\partial x_j} - \nu\overline{\left(\frac{\partial u_i}{\partial x_j} - \frac{\partial u_j}{\partial x_i}\right)\frac{\partial u_i}{\partial x_j}} \end{gathered} \tag{A.9}$$

The second to last term on the right hand side is dissipation of kinetic energy from the mean field:

$$\bar{\Phi} = \mu\left(\frac{\partial\overline{U_i}}{\partial x_j} - \frac{\partial\overline{U_j}}{\partial x_i}\right)\frac{\partial\overline{U_i}}{\partial x_j} \tag{A.10}$$

The last term on the right hand side is the dissipation of kinetic energy from the turbulent field:

$$\varepsilon = \nu\overline{\left(\frac{\partial u_i}{\partial x_j} - \frac{\partial u_j}{\partial x_i}\right)\frac{\partial u_i}{\partial x_j}} \tag{A.11}$$

For a closed domain with stationary boundaries, Equation A.9 can be written to express the total rate of change of mechanical energy as:

$$\frac{D}{Dt}\left(\frac{(\bar{U}_i + u_i)(\bar{U}_i + u_i)}{2}\right) = -\frac{1}{\rho}\bar{\Phi} - \varepsilon \tag{A.12}$$

Substitution of A.8 into the thermal energy equation, Equation A.6, and averaging with respect to time gives Equation A.8. (Cebici and Bradshaw, 1984, p. 36).

$$\frac{D\bar{h}}{Dt} = \frac{1}{\rho}\frac{D\bar{P}}{Dt} + \frac{1}{\rho}\bar{\Phi} + \varepsilon \tag{A.13}$$

The rate of change of entropy in a turbulent flow is given by

$$T\frac{Ds}{Dt} = \frac{1}{\rho}\bar{\Phi} + \varepsilon \tag{A.14}$$

The rate of change in total mechanical energy is exactly equal to the rate of increase in entropy of a turbulent flow.